

© 2018 Minwoo Kim

ULTRASOUND TISSUE PERFUSION IMAGING

BY

MINWOO KIM

DISSERTATION

Submitted in partial fulfillment of the requirements  
for the degree of Doctor of Philosophy in Electrical and Computer Engineering  
in the Graduate College of the  
University of Illinois at Urbana-Champaign, 2018

Urbana, Illinois

Doctoral Committee:

Professor Michael F. Insana, Chair  
Professor Zhi-Pei Liang  
Professor Michael L. Oelze  
Assistant Professor Wawrzyniec L. Dobrucki

# ABSTRACT

Enhanced blood perfusion in a tissue mass is an indication of neo-vascularity and potential malignancy. Ultrasonic pulsed Doppler imaging is a safe and economical modality for noninvasive monitoring of blood flow. However, weak blood echoes make it difficult to detect perfusion using standard methods without the expense of contrast enhancement. Additionally, imaging requires high sensitivity to slow, disorganized blood-flow patterns while simultaneously rejecting clutter and noise. An approach to address these challenges involves arranging acquisition data in a multi-dimensional structure to facilitate the characterization and separation of independent scattering sources. The resulting data array involves a linear combination of spatial, slow-time (kHz-order sampling), and frame-time (Hz-order sampling) coordinates. Applying an eigenfilter that exploits higher-order singular value decomposition (HOSVD) can technically transform the array and reduce the dimensions to yield power estimates for blood flow and perfusion that are well isolated from tissue clutter. Studies using microcirculation-mimicking simulations and phantoms enable the optimization of the filtering algorithm to maximize estimation efficiency. These techniques are applied to murine models of ischemia and melanoma at 24 MHz to form perfusion images. The results show enhancements of tissue perfusion maps, which help researchers access lesions without contrast enhancement. In a study aimed at peripheral artery disease (PAD), the enhanced sensitivity and specificity of ultrasonic-pulsed-Doppler imaging enable differentiation of perfusion between healthy and ischemic states. In addition, the use of the new ultrasound imaging coupled with other imaging modalities helps to illuminate the complex mechanism that mediates neovascularization in response to vascular occlusion. Consequently, these techniques have the potential to increase the effectiveness of existing medical imaging technologies in safe, cost-effective ways that promote sustainable medicine.

# ACKNOWLEDGMENTS

First, I would like to thank my advisor, Dr. Michael Insana. He is a smart, kind, patient and energetic mentor. He always encouraged me to focus on research and make a step forward. This work would not be possible without his incredible support and trust in me. I also want to express my appreciation to my Ph.D. committee members, Dr. Zhi-pei Liang, Dr. Michael Oelze and Dr. Wawrzyniec Dobrucki, for their service and helpful guidance. I must thank Dr. Craig Abbey at the University of California Santa Barbara for his advice and interest in my study. Working with all the intelligent professors made me broaden my expertise and knowledge.

Also, I would like to thank my great lab mates, Yang Zhu, Cameron Hoerig, Yiliang Wang, Yue Wang and Sara Bahramian, for their help and support in completing this work. I must thank Jamila Hedhli and Than Huynh in the Molecular Imaging Lab. Talking with them about school life and experiments was definitely a valuable and memorable time. I am grateful to my friends at the University of Illinois for sharing enjoyable moments. I also thank all friends in Korea for their encouragement.

Finally, I would deeply like to thank my parents and sister for their love and support. Their smiles and heartwarming words always made me feel positive whenever I felt down. Thanks to my family, I was never afraid of challenges and I devoted myself to achieving goals. I always respect and love them.

# TABLE OF CONTENTS

LIST OF ABBREVIATIONS . . . . .	vi
CHAPTER 1 INTRODUCTION . . . . .	1
1.1 Significance of Perfusion Imaging . . . . .	1
1.2 Problem Statement and Objectives . . . . .	2
1.3 Review of US Doppler Imaging . . . . .	3
1.4 Clutter Filtering Technique . . . . .	4
1.5 Dissertation Summary . . . . .	5
CHAPTER 2 EFFICIENCY OF PERFUSION ESTIMATORS . . . . .	7
2.1 Introduction . . . . .	7
2.2 Methods . . . . .	8
2.3 Results . . . . .	20
2.4 Discussion . . . . .	27
CHAPTER 3 MULTIDIMENSIONAL CLUTTER FILTERING USING HOSVD . . . . .	28
3.1 Introduction . . . . .	28
3.2 Methods . . . . .	30
3.3 Results . . . . .	42
3.4 Discussion . . . . .	49
3.5 Conclusion . . . . .	52
CHAPTER 4 CLUTTER FILTER OPTIMIZATION . . . . .	53
4.1 Introduction . . . . .	53
4.2 Methods . . . . .	54
4.3 Results . . . . .	67
4.4 Discussion . . . . .	76
4.5 Summary and Conclusions . . . . .	78
CHAPTER 5 CLINICAL APPLICATION . . . . .	80
5.1 Introduction . . . . .	80
5.2 Method . . . . .	81
5.3 Results . . . . .	85
5.4 Discussion . . . . .	89

CHAPTER 6 CONCLUSION . . . . .	92
REFERENCES . . . . .	94

# LIST OF ABBREVIATIONS

AUC	Area Under the Curve
BSS	Blind Source Separation
CD	Color Doppler
CEUS	Contrast-enhanced Ultrasound
CT	Computational Tomography
CW	Continuous-wave
FIR	Finite Impulse Response
GM	Gaussian Mixture
HbO <sub>2</sub>	Oxy-hemoglobin
HbR	Deoxy-hemoglobin
HOSVD	Higher-order Singular Value Decomposition
ICA	Independent Component Analysis
ID	Ideal
LSCI	Laser Speckle Contrast Imaging
MR	Magnetic Resonance
PA	Photoacoustic Imaging
PAD	Peripheral Artery Disease
PCA	Principal Component Analysis
PD	Power Doppler
PW	Pulsed-wave

RBC	Red Blood Cell
ROC	Receiver Operating Characteristic
SEM	Standard Error of Mean
SNCR	Signal-to-noise+clutter Ratio
SNR	Signal-to-noise Ratio
SVD	Singular Value Decomposition
US	Ultrasound

# CHAPTER 1

## INTRODUCTION

### 1.1 Significance of Perfusion Imaging

The characteristic patterns of blood flow are critical biomarkers indicating cardio and vascular diseases. Currently, medical imaging modalities can examine multiscale blood circulation, ranging from fast, organized flows in the heart and arteries to slow, disorganized perfusion patterns in capillaries of organs and peripheral tissues. Periodic monitoring of the functional changes in circulation contributes to the diagnosis of a wide range of clinical conditions, including diabetic complications, neuropathies, peripheral vascular and cardiovascular diseases, intracranial injury, and tumor growth. Imaging is also necessary for investigating drug delivery and developing treatments.

The purpose of the circulation is to deliver oxygen and nutrients to tissue cells and eliminate their metabolic wastes [1]. Since capillary beds surrounding the cells mainly take part in the exchange, visualizing them can indicate abnormal transportation mechanisms such as ischemia, hypoxia, and angiogenesis, which are critical for monitoring health, disease, and injury. Observation of the flow in an individual capillary is, however, technically challenging because the diameter is rather small (under  $5\ \mu\text{m}$ ). Instead, the arterioles and venules ( $10\text{-}200\ \mu\text{m}$ ) connected by capillary beds are more accessible. Measuring blood perfusion is an attractive alternative that can be used to identify the local tissue need. The definition of perfusion is total flow in a volume (mass) of tissue, and the range is from 1 to 10 ml/min/100g of tissue [2, 3].

Contrast-enhanced magnetic resonance (MR), computational tomography (CT), and optical and ultrasound (US) methods provide a comprehensive and detailed picture of microvascular structure and perfusion [4, 5]. Injectable contrast agents enable perfusion mapping through minimally invasive proce-

dures [6]. The wide array of imaging modalities gives practicing physicians a selection of techniques to manage each patient's situation. Perfusion imaging without contrast agents is preferred if the method proves reliable, affordable, low-risk, and widely accessible. Current laser Doppler techniques offer safer and less expensive contrast-free options for imaging surface perfusion in real time, but can only measure up to 1 to 2 mm of depth [7]. Techniques in the US are capable of a great depth of penetration and real-time processing but are effective in imaging only with contrast enhancement [8, 9].

## 1.2 Problem Statement and Objectives

Contrast-enhanced ultrasound (CEUS) has already been applied to peripheral artery disease (PAD) studies to evaluate the perfusion of leg skeletal muscle [10, 11]. In addition, quantitative perfusion analysis currently allows an objective characterization of tumors [12, 13]. Although US imaging without the use of contrast agents can be applied to clinical situations more economically and safely, the approach is mostly restricted to measuring large arterial vessels because of technical problems. Technical challenges involve significantly low contrast, signal-to-noise ratio (SNR), and Doppler frequency resolution arising from small blood volumes and low velocities. Voluntary and involuntary movements of surrounding tissue worsen perfusion identification for imaging.

This dissertation focuses on the US to provide highly sensitive perfusion images without the need for injectable agents. The specific aims of this work are to (1) develop optimal US imaging techniques by exploiting novel signal processing techniques to overcome the limitations, (2) build adequate simulations, and *in vitro* and *in vivo* models, to verify the technique, and (3) demonstrate that PAD studies are reliable through the quantitative analysis of US perfusion imaging. The advancement of computational technologies allows us to design and implement complex algorithms to improve diagnostic sensitivity and specificity. The imaging techniques incorporate stochastic signal models of physical phenomena and measurements to extract information specific to the clinical task. The methods are applied to existing commercial US instruments, which makes these methods immediately valuable to medical practice provided they are effective and reliable.

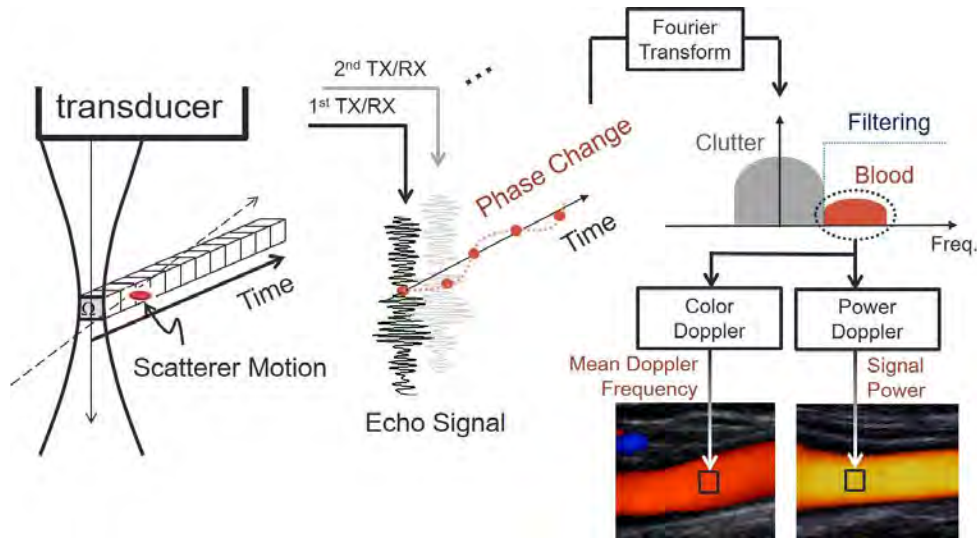


Figure 1.1: Standard US Doppler acquisition and processing are illustrated. A transducer emits repetitive narrow-band pulses to trace the displacement of scatterers over time. The motion results in the phase change between received echoes. A Fourier-based high-pass filter isolates blood signal from strong clutter using the discrepancy of Doppler shifts (motion speed). Color Doppler and power Doppler modes display the mean Doppler frequency and signal power, respectively.

### 1.3 Review of US Doppler Imaging

Doppler techniques in the US focus on the measurement of blood flow [14]. The framework involves evaluating the variation of received echoes to detect the movement of red blood cells (RBCs). As illustrated in Fig. 1.1, a transducer transmits a series of narrow-band pulses at the same time intervals and records consequent echoes. The technique in which pulsed-wave (PW) is emitted is exploited more than the technique that emits continuous-wave (CW) to distinguish echoes arising from two scatterers positioned at different depths along a scan-line. The scatterer motion causes the phase difference between received echoes at each fixed depth (slow-time ensemble) from consecutively transmitted pulses. Modulation frequency (Doppler shift) is proportional to axial motion speed.

Due to the benefit of spatial resolution, the PW technique facilitates imaging to monitor vascular structure and local blood distribution. Standard imaging modes include color Doppler (CD) and power Doppler (PD). Color Doppler estimates the mean velocity at every depth position along every ad-

jacent scan-line. Velocity information is presented in color and superimposed on the gray-scale anatomical image (B-mode image). Power Doppler imaging encodes the signal power computed by integrating echo amplitude to detect the moving scatterers or measure their concentration.

Power Doppler has several advantages over CD in accessing a weak perfusion signal [15, 16]. Firstly, PD is less sensitive to acquisition noise than CD. Color Doppler is likely to involve high estimation error since phase noise randomly occurs when calculating the mean frequency shift. However, representation of the noise is different in PD as the noise has uniformly low power in general. Integrating a power spectrum thus results in relatively high SNR. Secondly, PD is less dependent on the angle between flow direction and beam propagation direction. While a Doppler shift is angle-dependent, the power remains the same as long as it is detectable. Lastly, in PD, power compensation for attenuation can improve perfusion quantification.

## 1.4 Clutter Filtering Technique

In data acquisition, the blood signal is corrupted by clutter mainly arising from moving tissue or vessel walls. Respiration is one of the dominant sources, inducing gross displacement of tissue around the abdominal area. Additionally, pulsation contributes to the periodic displacement of tissue near arteries, and internal muscle continuously vibrates. The echo power of clutter is around 20 to 100 dB stronger than that of blood [17, 18]. As illustrated in Fig. 1.1, standard imaging uses a Fourier-based high-pass filter to separate the blood signal from clutter [14]. The fast motion of RBCs in arterial flow causes a high Doppler shift. However, when assessing slow flow in the microvasculature, the blood and clutter components of the Doppler frequency spectrum overlap significantly. To obtain a high ratio of blood-to-clutter components, filtering needs to exploit other characteristics beyond the motion speed.

Many studies proposed for clutter filtering are based on blind-source separation (BSS) [19, 20, 21]. These BSS methods take advantage of principal component analysis (PCA) or independent component analysis (ICA) [22, 23, 24]. The techniques begin with assumptions that acquisition data involve a set of independent sources and their exact properties are hardly

known. The common process follows three steps: (1) Input data is converted into specific coordinates associated with a statistical independent criterion to separate the sources, (2) filtering is conducted by suppressing unwanted source components in the new domains, and (3) filtered data is inversely transformed into the original domains.

Eigenfilters based on PCA currently appear to perform better than standard filters for *in vitro* and *in vivo* tests [18, 25]. The filters are adaptive in that temporal eigenbases are specific to the data and able to separate the sources of echo decorrelation. The eigenvalues associated with echo power of the sources facilitate the selection of blood-dominant bases. Dimension expansion using singular value decomposition (SVD) provides even better source separation as it preserves the characteristic differences between the spatial and temporal response of the sources [26, 27]. Plane-wave techniques can achieve higher acquisition rates to facilitate noise averaging when forming SVD filters [28].

## 1.5 Dissertation Summary

The fundamental contribution of this dissertation is to increase the sensitivity and specificity of US Doppler imaging to tissue perfusion. This research is motivated by the discovery that altering the spatiotemporal sampling in ways that build a multidimensional data array can enhance the sensitivity of the measurement to physiological perfusion. Since an increase in sensitivity naturally decreases specificity, novel statistical filtering techniques are needed to isolate signal components specific to the clinical task.

Chapter 2 addresses a preliminary study to investigate the possibility of statistical processing approaches. The efficiency of conventional PD methods in discriminating flow states is examined by comparing measurement performance to that of the Bayes methods using a multivariate Gaussian model [29]. *In vitro* experiments are conducted to observe that the statistical method is more efficient provided that random scattering from blood and soft tissues is well-represented by the temporal covariance matrix of echo data. All efficiencies are measured by areas under receiver operating characteristic (ROC) curves.

Chapter 3 focuses on multidimensional eigenfiltering for perfusion imag-

ing. The role of the eigenfilter is to adaptively suppress clutter and noise components from given stationary data samples prior to the estimation of local perfusion. To better characterize the sources, the strategy involves exploiting statistics of multiple modes by adopting the following sampling pattern. Doppler pulses sampled at kHz-order are acquired to form a Doppler frame. Frames are recorded at 10 to 30 Hz. This echo data is organized into a multidimensional array depicting slow-time, frame-time, and spatial bases. Higher-order singular value decomposition (HOSVD) is a feasible tool to incorporate statistics of the three modes to increase the separability of independent sources.

Chapter 4 describes filtering optimization. Following HOSVD, filtering is conducted by nullifying unwanted components. The accurate selection of clutter-dominated and noise-dominated subspace is thus required to enhance estimation efficiency. In this study, a comprehensive simulation is proposed to extract features and build a robust classification model. The simulation mimics US Doppler acquisition based on realistic models of tissue motions and microvascular flows. The synthetic data is used to train and test the classifier to minimize selection errors. All processes are validated using a couple of *in vitro* and *in vivo* models.

In Chapter 5, perfusion imaging is applied to studies for peripheral artery disease (PAD). The murine hindlimb ischemia is a typical experimental model used to understand PAD and develop new therapies. The loss of muscle blood flow occurs when the femoral artery of a healthy mouse is ligated. After several days, angiogenesis rebuilds the vasculature enough to restore most of the perfusion, and the use of the leg returns. The US imaging technique is used to track muscle perfusion changes for two weeks. This imaging coupled with other imaging modalities allows us to establish the complex angiogenic process.

# CHAPTER 2

## EFFICIENCY OF PERFUSION ESTIMATORS

### 2.1 Introduction

The study examines the ideal (ID) discriminator of ultrasonically detected blood-perfusion states. This statistical discriminant function leverages properties of the temporal covariance matrix of RF echo signals to describe echo decorrelation within a scattering region caused by scatterer motion and noise. The ideal discriminator fully incorporates temporal statistical information about the random object scatterers into a scalar test statistic that maximizes the area under the receiver operating characteristic (ROC) curve [30], or AUC, thus maximizing classification performance [31, 32]. Provided scattering is an incoherent Gaussian process, all anatomical and flow information is found within the covariance matrix of the object scatterers. The covariance matrix for the object function is simply related to that for the pulse-echo measurements using linear systems [33].

Heimdal and Torp [34] used a statistical discriminant function as a new color-Doppler estimator in a manner similar to the analysis described below. Later Hovda et al. [35] also applied statistical estimators in a technique they called knowledge-based imaging. Both studies found the statistical approach to flow estimation can be very sensitive to flow, but it requires knowledge of the covariance matrices for all possible flow conditions. The goal in this chapter is to use statistical estimators to assess the efficiency of standard power Doppler methods.

The temporal covariance matrix for an imaging experiment is a combination of pulse properties, scatterer echogenicity, and scatterer movement. When these properties are known, as they can be in phantom measurements, the covariance matrix for specific flow conditions can be estimated from echo samples. Then the ideal discriminator described in this chapter can be com-

puted and its performance compared with standard methods to estimate flow discrimination efficiency. Efficiency quantifies the fraction of available task information being used by the estimator. Traditional power-Doppler methods are suboptimal discriminators because they fail to incorporate all of the specific information about the interaction between pulse and scatterer motion interactions. This information is specific to each perfusion event but unknown during clinical studies.

The first step in our approach is to estimate the temporal covariance matrix of RF echo-data measurements obtained from a perfusion phantom. It explores how the amount of RF echo data used for ensemble averaging influences covariance estimates. For this aspect of the study, principal component analysis (PCA) [22] is applied to the echo covariance matrix to separate blood echoes from tissue clutter and acquisition noise [20] in an attempt to reduce the amount of echo data required to accurately estimate the covariance matrix.

The next step is to show that power Doppler estimates employing FIR clutter filters can be expressed in a manner analogous to the ID test statistic. ROC curves are generated for comparisons of both methods. From perfusion phantom data, ROC curves are estimated for discriminating between pairs of flow states using conventional power Doppler methods. These results are compared to the ID results to estimate the efficiency of conventional methods. The final step is to show how the binary discrimination task may be extended to more general flow conditions in a way that illustrates how inefficiency reduces the visibility of flow in power Doppler images of the phantom.

## 2.2 Methods

### 2.2.1 Flow Phantom

Ultrasonic measurements were made using the perfusion phantom illustrated in Fig. 2.1. The critical unit was a dialyzer cartridge consisting of a bundle of hundreds of 0.2 mm inner-diameter polysulfone fibers (B. Braun Medical Inc., Allentown, PA USA). Using a programmable syringe pump connected to the cartridge, we steadily infused in a closed loop through the fibers either pure water for the control state or blood-mimicking fluid (CIRS, Norfolk,

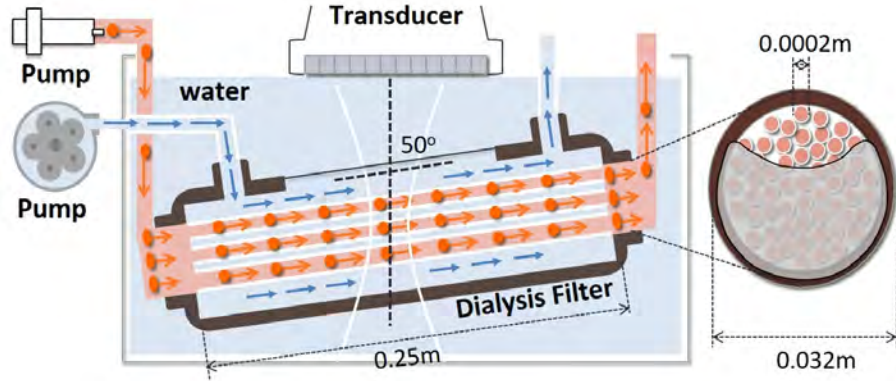


Figure 2.1: A dialyzer cartridge was used to mimic blood perfusion in a clutter and noise environment. An ultrasonic linear array scans the cartridge to acquire echo data in spectral Doppler mode. Perfusion rates are controlled by a syringe pump infusing either water or blood-mimicking fluid through the fibers while a peristaltic pump circulates the water surrounding the fibers to simulate clutter. As shown, blood-mimicking fluid flow was limited to a cross-sectional area of fibers about 25% ( $\sim 2 \text{ cm}^2$ ) of the total area.

USA) for the test state. In this way we simulated spatially directed blood perfusion in the range of 0.0 - 2.0 ml/min over a cross-sectional area  $2 \text{ cm}^2$  approximately<sup>1</sup>. In addition to intra-fiber infusion, a second set of cartridge connections allowed water to be pulsed into the cartridge outside the fibers. Connecting a 1 Hz peristaltic pump in this way, we simulated clutter from cardiac motion. A portion of the protective plastic case was removed to provide an acoustic window, and then the entire cartridge was submerged in degassed water at room temperature.

Flow is limited to just the most proximal  $2 \text{ cm}^2$  of the cross-sectional fiber area so that net flows  $\leq 2 \text{ ml/min}$  provided representative scatterer velocities within the fibers. We note that the density ( $1.24 \text{ g/cm}^3$ ) and longitudinal sound speed ( $2260 \text{ m/s}$ ) of the polysulfone fibers present a strong impedance mismatch with the surrounding fluids, which reduces sound penetration and echo SNR. However the ideal detector is limited by echo SNR in the same

<sup>1</sup>*In vivo* perfusion is the steady-state delivery of blood to a unit of tissue, often measured in units of flow per tissue mass. For example, reported perfusion measurements in VX2 rabbit tumors spans a large range, from 13.5 ml/min/100 g using PET techniques [36] to 0.2-1.1 ml/min/g using radioactive microspheres [37]. In this report, *perfusion* is the directed flow of blood-mimicking fluid through a fixed  $\sim 2 \text{ cm}^2$  cross sectional area of 25-cm-long packed microtubules; the total flow is varied between 0.1-2.0 ml/min.

way as other estimation methods, so that discrimination efficiencies will be relatively unaffected, even if this represents a somewhat more difficult environment for perfusion estimation.

### 2.2.2 Signal Model

All modeling and analysis were conducted in MATLAB . In a spectral-Doppler acquisition, a single line of sight (Fig. 2.1) is repeatedly probed with  $N'$  narrow-band pulses as  $M'$  range echoes are recorded after each pulse transmission. The result is an  $M' \times N'$  matrix  $\mathbf{X}'$  with elements  $X'[m, n]$ . Two examples are shown as gray-scale images at the top of Fig. 2.2.

Column vectors of  $\mathbf{X}'$  describe temporal sampling along a fixed transducer line of site; each vector is the RF echo signal from the  $n$ th pulse along the “fast-time” axis  $\mathbf{x}_n$  with elements  $x_n[m]$  and  $0 \leq m \leq M' - 1$ . Row vectors  $\mathbf{x}_m$  are echoes along the “slow-time” axis where echo signal samples are  $x_m[n]$  for  $0 \leq n \leq N' - 1$ . Integer index  $m$  also indicates the distance  $z$  from the transducer surface (depth) via  $z[m] = z_0 + cmT'/2$ , where  $z_0$  is the distance at which recording begins,  $c$  is the compressional wave speed, and  $T'$  is the fast-time sampling interval. The time interval between pulse transmissions (and slow-time samples) is  $T$ ,  $1/T$  is the pulse repetition frequency, and  $T \geq M'T'$ . Since the fast-time axis also corresponds to depth, we may consider  $\mathbf{X}'$  as composed of echoes recorded at  $M'$  depths each from  $N'$  pulses along the slow time axis.

The temporal covariance matrix for zero-mean echo signals recorded at depth  $z[m]$  is the expected value of the outer product of the  $m$ th row vector in  $\mathbf{X}'$ , i.e.,  $\Sigma_x = E(\mathbf{x}_m \mathbf{x}_m^T)$ , where superscript  $T$  indicates vector transpose. We assume the standard physical model of blood flow in Doppler ultrasound, where there are three stochastic sources contributing to  $\Sigma_x$  [18, 20, 27, 28, 31], and each source is assumed to be an independent zero-mean multivariate normal random process. The three covariance sources are tissue scattering represented by matrix  $\mathbf{C}$  (for clutter), blood scattering by matrix  $\mathbf{B}$ , and acquisition noise by matrix  $\mathbf{E} = \sigma_e^2 \mathbf{I}$ . The quantity  $\sigma_e^2$  is the noise variance and  $\mathbf{I}$  is an identity matrix. Unlike  $\mathbf{E}$ , matrices  $\mathbf{C}$  and  $\mathbf{B}$  are not diagonal, representing the fact that clutter and blood signals persist to some extent

through time. They contribute to  $\Sigma_x$  through the filter of instrumentation,

$$\Sigma_x = \Sigma_c + \Sigma_b + \mathbf{E} = \mathbf{HCH}^T + \mathbf{HBH}^T + \sigma_e^2 \mathbf{I}, \quad (2.1)$$

where  $\mathbf{H}$  is the measurement-system matrix. In this model, all tissue and blood information is contained in  $\Sigma_x$ .

In practice, an  $M \times N$  subset of  $\mathbf{X}'$  is selected to form the smaller echo matrix  $\mathbf{X}$ , where  $M \leq M'$  and  $N \leq N'$ . We then assume there may be a non-zero mean and that the signal are ergodic, where spatial averaging is used in place of ensemble averaging to estimate  $\Sigma_x$ . For  $M \times N$  echo matrix  $\mathbf{X}$ , the approximation is the  $N \times N$  covariance

$$\Sigma_x \simeq \frac{1}{M-1} (\mathbf{X} - \bar{\bar{x}})^T (\mathbf{X} - \bar{\bar{x}}), \quad (2.2)$$

with mean  $\bar{\bar{x}} = \frac{1}{MN} \sum_{m=0}^{M-1} \sum_{n=0}^{N-1} X[m, n].$

Ergodicity is possible when the impulse-response function is shift invariant and the contributing sources are stationary for all  $M$  rows of  $\mathbf{X}$ .

If more data are desired for averaging to improve the estimate of Eq. (2.2), the  $N'$  samples in  $\mathbf{X}'$  may be partitioned to augment the number of rows. For example, if we recorded  $N' = 1000$  pulses at  $M' = 100$  depths (total of 1.54 s at 650 Hz PRF), each row could be partitioned and rearranged into five 200-pulse packets to form a  $500 \times 200$  matrix  $\mathbf{X}$ , yielding covariance matrices of size  $200 \times 200$ .

### 2.2.3 Ideal Discriminator Approach to Perfusion Estimation

Assuming the covariance matrices can be accurately measured, consider a measurement vector  $\mathbf{x}$  (subscript  $m$  is understood). Its specific properties are unknown except that it was recorded from one of two possible perfusion states that we label 0 or 1. Echo signals from the two states are both multivariate-normal zero-mean processes,

$$\mathbf{x} \sim \begin{cases} MVN(\mathbf{0}, \Sigma_{x|0}) & \text{for perfusion state 0} \\ MVN(\mathbf{0}, \Sigma_{x|1}) & \text{for perfusion state 1} \end{cases}, \quad (2.3)$$

where  $\Sigma_{x|0} = \Sigma_c + \Sigma_{b_0} + \mathbf{E}$  and  $\Sigma_{x|1} = \Sigma_c + \Sigma_{b_1} + \mathbf{E}$ . That is,  $\Sigma_{x|i}$  are  $\Sigma_x$  measured for the  $i$ th state, where  $i = 0$  or  $1$ . The only difference between these two echo-signal distributions is the perfusion rate via  $\Sigma_{b_i}$ .

The classification task is to decide to which state  $\mathbf{x}$  belongs. That task is optimally achieved by the likelihood ratio test [38] given by the ratio of echo probability density functions conditioned on the two states,

$$\ell(\mathbf{x}) = \ln \frac{p(\mathbf{x}|1)}{p(\mathbf{x}|0)} \sim \frac{1}{2} \mathbf{x}^T (\Sigma_{x|0}^{-1} - \Sigma_{x|1}^{-1}) \mathbf{x} = \mathbf{x}^T \mathbf{Q} \mathbf{x}. \quad (2.4)$$

The symbol  $\sim$  is used to indicate that terms independent of  $\mathbf{x}$  are discarded since they do not influence classification performance [33]. Scalar  $\ell(\mathbf{x})$  is the test statistic for the ideal discriminator, a quadratic function of testing-data vector  $\mathbf{x}$ . For convenience, we define the difference between inverse covariances for the two states by the matrix

$$\mathbf{Q} = \Sigma_{x|0}^{-1} - \Sigma_{x|1}^{-1}. \quad (2.5)$$

In the following, we refer to echo data recorded for estimating  $\Sigma_x$  as *training data*. Alternatively the echo data indicated by  $\mathbf{x}$  in Eq. (2.4) are referred to as *testing data*. Training and testing are conducted on different sets.  $\Sigma_x$  are estimated using Eq. (2.2) and training data. These matrices are nonsingular because of the presence of acquisition noise; their inverses exist as long as there are more samples than degrees of freedom.  $\Sigma_x$  and  $\mathbf{Q}$  estimations are described in Section 2.2.4 and illustrated in Fig. 2.2.

Decisions based on test vector  $\mathbf{x}$  for which  $\ell(\mathbf{x})$  has been estimated are expressed as

$$D(\mathbf{x}) = \text{step}(\ell(\mathbf{x}) - \tau), \quad (2.6)$$

indicating the decision is state 0 when  $\ell < \tau$  and state 1 when  $\ell \geq \tau$  for threshold  $\tau$ . For example,  $\ell(\mathbf{x}|1)$  is correctly classified when  $D(\mathbf{x}) = 1$  and incorrectly classified when  $D(\mathbf{x}) = 0$ . To measure discrimination performance, consideration of all possible threshold values is required as shown in Section 2.2.7.

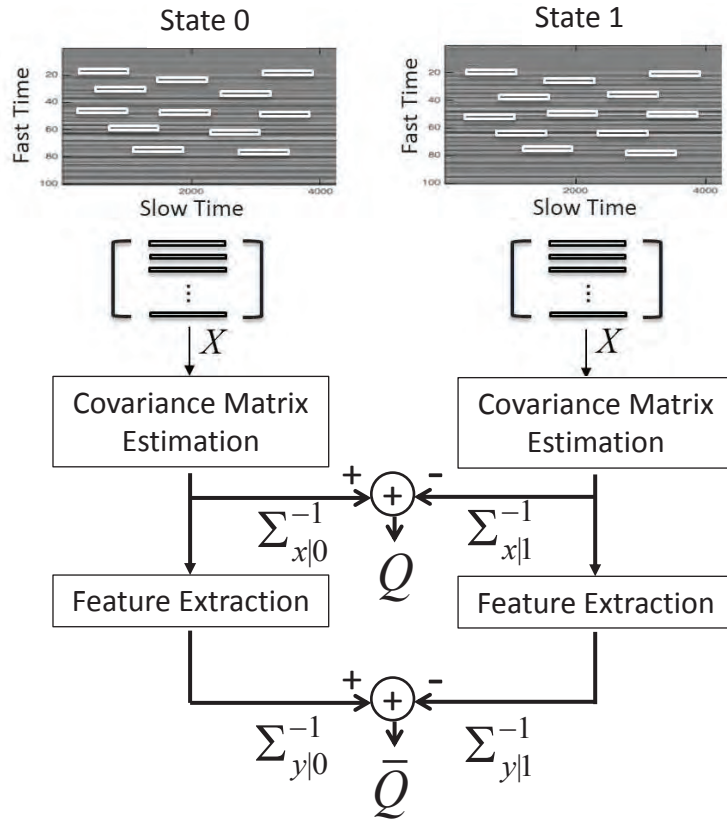


Figure 2.2: Illustration of the procedure for generating data matrices  $\mathbf{X}$  and covariance matrices  $\Sigma_{x|i}$ . From covariance matrix inverses,  $\mathbf{Q}$  are formed (Eq. (2.5)) and  $\bar{\mathbf{Q}}$  (Eq. (2.14) in Section 2.2.8). Echo vectors randomly selected from within  $\mathbf{X}'$  (i.e., the small white rectangles in grayscale images at top) are used to form  $\mathbf{X}$ .

### 2.2.4 Estimating $\Sigma_{x|i}$ and $\mathbf{Q}$

The top of Fig. 2.2 illustrates the process of randomly selecting data vectors for  $\mathbf{X}$  to estimate  $\Sigma_x$ . In this example, we recorded 3250 (650/s  $\times$  5 s) RF echo signal segments for a fixed-position 2 mm range gate (2 mm  $\times$  20 samples/ $\mu$ s)/(0.77 mm/ $\mu$ s)=52 samples) near the transmit focus of the transducer. Throughout each 52 $\times$ 3250 matrix  $\mathbf{X}'$  (grayscale images at top of Fig. 2.2), we assume the system response is linear time-invariant and the random processes associated with the three sources are wide-sense stationary. We then randomly select packets to form data sub-matrix  $\mathbf{X}$ . The length and number of packets selected depend on the experiment.

### 2.2.5 Standard Approaches to Perfusion Estimation

We can express standard power Doppler estimation using an expression similar to Eq. (2.4) as follows for a single test vector  $\mathbf{x}$ . Techniques that apply a Fourier-domain wall filter to minimize clutter can be written as

$$\bar{\ell} = (\mathbf{F}\mathbf{x})^T(\mathbf{F}\mathbf{x}) = \mathbf{x}^T\mathbf{Q}_{PD}\mathbf{x} . \quad (2.7)$$

$\mathbf{F}$  is a circulant  $N \times N$  matrix that defines a high-pass filter. We define  $\mathbf{Q}_{PD} \triangleq \mathbf{F}^T\mathbf{F}$ , which is different from  $\mathbf{Q}$  that involves covariance matrices in Eq. (2.4). For example, a DC-cancellation filter is

$$\mathbf{Q}_{PD} = \mathbf{I} - \frac{1}{N}\mathbf{1} , \quad (2.8)$$

for  $N \times N$  matrix  $\mathbf{1}$  in which every element is set to one.

### 2.2.6 $\mathbf{Q}_{PD}$ and $\mathbf{Q}$ Matrices

Figure 2.3 displays  $\mathbf{Q}_{PD}$  (top row) and  $\mathbf{Q}$  (bottom row) matrices as images.  $\mathbf{Q}_{PD}$  matrices are for the DC cancellation filter (A), a 12.25 Hz high-pass FIR filter (B), and 60 Hz high-pass FIR filter (C).  $\mathbf{Q}_{PD}$  are formed independently of echo data because they are simply implementations of high-pass filters.

In contrast,  $\mathbf{Q}$  are formed from echo signals recorded at specific perfusion states. Parts (D), (E) and (F) show  $\mathbf{Q}$  matrices for steady blood-mimicking

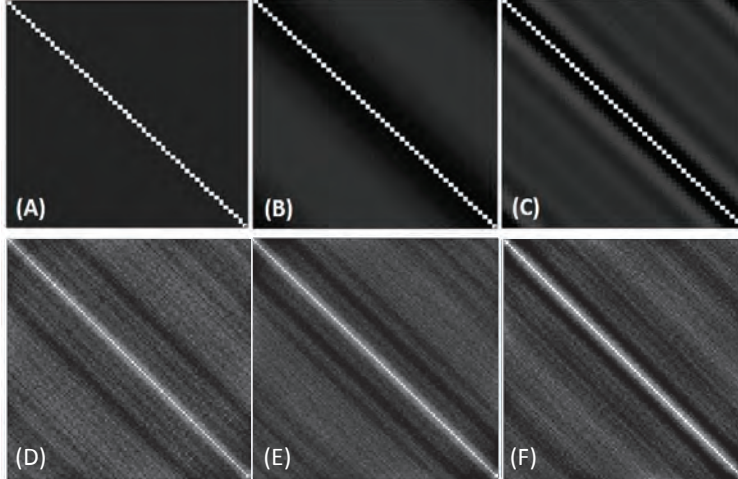


Figure 2.3: The top row shows  $100 \times 100$   $\mathbf{Q}_{PD}$  matrices for, respectively, a DC cancellation filter, 12.25 Hz FIR high-pass filter, and 60 Hz FIR high-pass filter. Each matrix in the top row implements the operation of high-pass filtering and summing in the time domain via Eq (2.7) to yield signal power measurements for conventional PD estimates. The  $100 \times 100$  matrices (D), (E) and (F) are  $\mathbf{Q}$  matrices for the ID estimator (unfiltered echo data) at three perfusion rates, 0.4, 1.0 and 2.0 ml/min, respectively. Each experimentally measured matrix is the difference between two inverse covariance matrices via Eq (2.5), and has patterns characteristic of the pair of flow states being compared. The covariance matrices forming  $\mathbf{Q}$  in the bottom row are stationary and thus Toeplitz; each was formed using an ensemble of 50,000 packets to obtain low-noise estimates.

perfusion at three rates compared with their controls. Because each is the difference between two inverse covariance matrices, it is hard to intuit the patterns in each case. The bottom row shows that  $\mathbf{Q}$  matrices describe experimental information specific to the combination of pulse properties, echogenicity and perfusion properties that do not appear in the generic  $\mathbf{Q}_{PD}$  of the top row.

### 2.2.7 Discrimination Performance

Performance quantifies the ability to achieve a task. Flow-discrimination performance is measured by comparing AUC values resulting when perfusion estimates are used to differentiate distinct perfusion states.

Figure 2.4 illustrates the formation of ROC curves from histograms of  $\ell(\mathbf{x}|1)$  for test state 1 (0.4 ml/min blood-mimicking fluid flow) and  $\ell(\mathbf{x}|0)$  for control state 0 (0.4 ml/min water flow). The histograms provide estimates of the probability of detection,  $P_D = P(\ell(\mathbf{x}|1) > \tau)$ , versus the probability of false alarm,  $P_F = P(\ell(\mathbf{x}|0) > \tau)$  [39]. That is,  $P_D(\tau)$  and  $P_F(\tau)$  are found by summing the histograms from  $\tau \leq \ell(\mathbf{x}) < \infty$  over all possible  $\tau$  to generate the ROC curve shown on the right. Perfect detection yields  $AUC = 1$ , which occurs when the two distributions do not overlap. A worthless detector generates an  $AUC = 0.5$  that results from the two probability distributions being identical.

The efficiency  $\eta$  by which standard power-Doppler techniques distinguish two perfusion states compared to that of the ideal discriminator for the same task is computed using [33]

$$\eta = \frac{\Phi^{-1}(AUC_{PD})}{\Phi^{-1}(AUC_{ID})}. \quad (2.9)$$

Function  $\Phi^{-1}(\cdot)$  is the inverse of the cumulative normal function, and  $AUC_{PD}$  and  $AUC_{ID}$  are areas under the ROC curves for the standard power-Doppler and ideal-discriminator approaches, respectively.

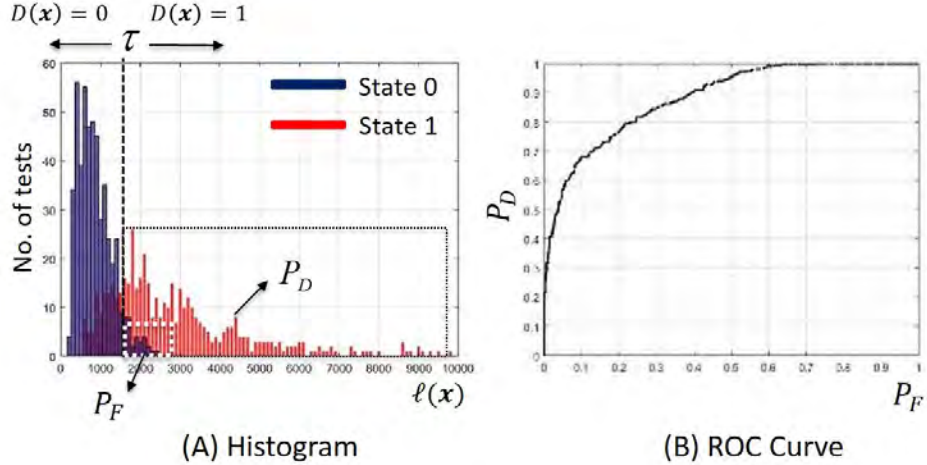


Figure 2.4: (A) Histogram of likelihood ratios  $\ell$  found from phantom measurements for two perfusion states. The distributions of clutter and noise are the same for the two states, but the blood flow states are different. Red and blue histograms represent  $\ell(\mathbf{x}|1)$  and  $\ell(\mathbf{x}|0)$ , respectively. The probability of correctly detecting blood-mimicking fluid perfusion is  $P_D$  and the false alarm probability is  $P_F$ . These are found by integrating histograms for  $\ell(\mathbf{x}|1)$  and  $\ell(\mathbf{x}|0)$  above threshold  $\tau$ . (B) The ROC curve is a plot of  $P_D$  versus  $P_F$  as discrimination threshold  $\tau$  is varied. AUC in this case is 0.83.

### 2.2.8 PCA Filtering

When we know the echo covariance matrix, e.g., if we can precisely measure it for known perfusion conditions, there is no need to separate the different contributions since each known source of covariance becomes part of the ID calculation. Clutter and noise filtering are required clinically because these covariances are unknown. We were concerned that errors made while estimating the covariance matrix might degrade classification performance below the ideal (maximum) value. To address this concern, we studied how the size of the echo-data training set influenced performance and report the results below. During that study, we also asked if filtering the training data used to estimate  $\Sigma_x$  to suppress clutter and noise might allow ideal performance to be achieved with less training data.

This section describes our implementation of principal component analysis specifically for reducing errors in covariance matrix estimates. Filtering out sources that contribute to  $\Sigma_x$  is a reduction in dimensionality [18, 20, 22, 27, 28] that we seek to achieve by identifying matrix  $\mathbf{W}$  that returns clutter-

and noise-suppressed vector  $\mathbf{y}$  from training echoes  $\mathbf{x}$ . That is,

$$\mathbf{y} = \mathbf{W}\mathbf{x}, \quad (2.10)$$

where  $\mathbf{x} \in \mathfrak{R}^{N \times 1}$ ,  $\mathbf{y} \in \mathfrak{R}^{J \times 1}$ , and  $\mathbf{W} \in \mathfrak{R}^{J \times N}$  for  $J \leq N$ .  $\mathbf{W}$  is chosen to maximize the separability of likelihood functions  $p(\mathbf{y}|0) = p(\mathbf{W}\mathbf{x}|0)$  and  $p(\mathbf{y}|1) = p(\mathbf{W}\mathbf{x}|1)$  for the two perfusion states; i.e., there is a function  $f$  such that

$$\mathbf{W} = \arg \max_{\mathbf{W}'} f(p(\mathbf{W}'\mathbf{x}|0), p(\mathbf{W}'\mathbf{x}|1)). \quad (2.11)$$

$\mathbf{W}$  is found from an eigen-decomposition of the covariance matrix

$$\begin{aligned} \Sigma_{x|i} &= \sum_{k=1}^N \lambda_k \mathbf{u}_k \mathbf{u}_k^T \\ &= \sum_{k \in C} \lambda_k \mathbf{u}_k \mathbf{u}_k^T + \sum_{k \in B} \lambda_k \mathbf{u}_k \mathbf{u}_k^T + \sum_{k \in E} \lambda_k \mathbf{u}_k \mathbf{u}_k^T, \end{aligned} \quad (2.12)$$

where eigenvalues  $\lambda_k$  and eigenvectors  $\mathbf{u}_k$  are listed in descending order left to right and grouped into three subspaces  $C$ ,  $B$  and  $E$  as shown in Fig. 2.5.

Moving-tissue echoes (clutter) typically contribute the largest eigenvalues to  $\Sigma_{x|i}$ , as tissue scattering is more echogenic than blood scattering. Also, the spatially coherent and temporally periodic patterns of clutter motion concentrates their eigenmodes into a low-dimensional subspace with eigenvectors  $\{\mathbf{u}_k | k \in C\}$ . In contrast, the weaker scattering of red blood cells generates blood-echo components in lower-amplitude eigenvalues. As perfusion often generates a more diverse pattern of scatterer motion than clutter, it forms a somewhat larger-dimensional subspace with eigenvectors  $\{\mathbf{u}_k | k \in B\}$ . Acquisition noise is typically the smallest-energy component of the echo-signal covariance and it usually spans the entire basis.

Given that blood components in  $B$  correspond to eigenvalues at  $\{k, \dots, k+J-1\}$  ( $k = 3, 4, 5$  in the simplified example of Fig. 2.5), then  $\mathbf{y}$  is found from the projection of signal vector  $\mathbf{x}$  onto that feature space. In terms of Eq. (2.10) we have

$$\mathbf{W} = [\mathbf{u}_k, \mathbf{u}_{k+1}, \dots, \mathbf{u}_{k+J-1}]^T. \quad (2.13)$$

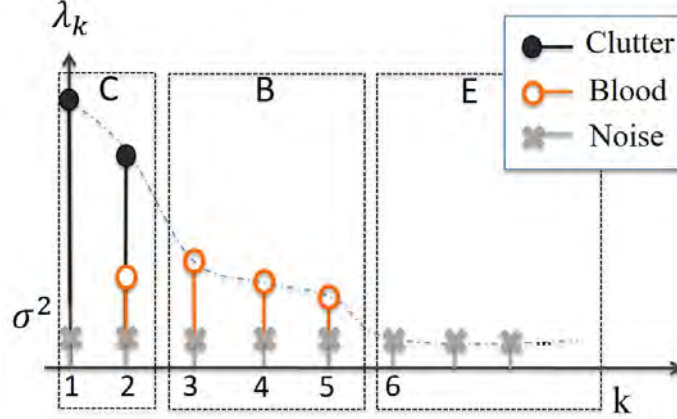


Figure 2.5: A simplified eigenspectrum of Doppler echo-signal vector  $\mathbf{x}_m$  where eigenvalues  $\lambda_k$  are sorted in decreasing order. Values are grouped into sets,  $C$ ,  $B$  and  $E$ , that approximate the three sources contributing to  $\Sigma_x$ .

Consequently,  $J$  is the cardinality of set  $B$  since we assume the other subspaces have no information useful for discriminating perfusion states. In this study, we selected  $k$  and  $J$  for PCA filtering by discovering which subgroup of eigenvalues maximized flow discrimination performance via AUC measurements.

The eigenbasis cannot completely separate blood and clutter components but, among all orthonormal bases of that dimension, it spans the maximum clutter-signal energy such that the mean-square error between it and the true clutter signal is minimized [17].

Applying PCA filtering to covariance matrix estimates, we have

$$\begin{aligned}
 \Sigma_{y|i} &= \mathbf{W}_i \Sigma_{x|i} \mathbf{W}_i^T, \quad i = 0, 1, \\
 \tilde{\ell}(\mathbf{x}) &= \mathbf{x}^T (\mathbf{W}_0^T \Sigma_{y|0}^{-1} \mathbf{W}_0 - \mathbf{W}_1^T \Sigma_{y|1}^{-1} \mathbf{W}_1) \mathbf{x} \\
 &= \mathbf{x}^T \tilde{\mathbf{Q}} \mathbf{x}.
 \end{aligned} \tag{2.14}$$

$\tilde{\mathbf{Q}} \in \mathbb{R}^{N \times N}$  has rank  $J < N$ , and so  $\tilde{\mathbf{Q}}$  is a reduced-rank version of  $\mathbf{Q}$ .  $\tilde{\mathbf{Q}}$  estimation is illustrated in Fig. 2.2.

## 2.3 Results

### 2.3.1 Data Acquisition

Echo data were recorded using a Sonix RP ultrasonic imaging system (Ultrasonix Medical Corp., Richmond, BC, Canada) and a linear-array transducer. The transducer, located above the dialyzer cartridge, probes the fibers with narrow-band pulses at a Doppler angle of 50 degrees. Tests with blood-mimicking fluid provide perfused-state data including clutter, blood, and noise signals. Control data were recorded by replacing the blood-mimicking fluid with degassed water, thus maintaining the same clutter and noise signal. Table 2.1 summarizes the experimental parameters.

Table 2.1: Acquisition Parameters

Parameter	Value
Probe type	Ultrasonix L14-5
Pulse center frequency	5.0 MHz
Doppler pulse length	4 cycles
In-plane transmit focal length	15.75 mm
In-plane transmit f-number	2.02
Testing ensemble size	40-100 pulses
Fractional bandwidth	20%
Axial range of sample volume	2 mm
Pulse repetition frequency	220-650 Hz
Fast-time sampling rate	20 MHz
PD line density (Fig. 2.10)	2.5/mm

### 2.3.2 Experimental Overview

Blood-mimicking fluid perfusion state 1 was compared to its water-only control state 0 to study perfusion *detection* in Experiment I. Comparison of two different blood-mimicking perfusion states between 0 and 2 ml/min was conducted to study perfusion *discrimination* in Experiment II. From histograms of test statistic responses, e.g., Fig. 2.4, AUC values were computed for conventional power Doppler and ID estimators and applied to Eq. (2.9) to determine estimator efficiency.

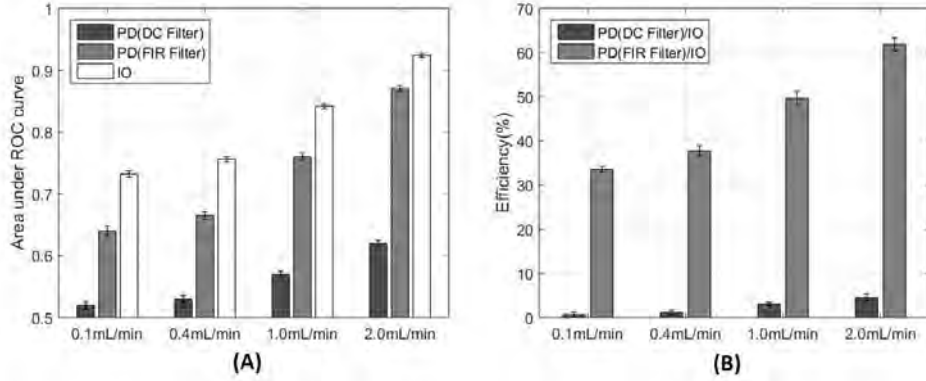


Figure 2.6: (A) Areas under ROC curves (AUCs) for perfusion detection using different perfusion rates and estimators. The state 0 condition uses water in place of the blood-mimicking fluid. The white bar indicates ideal-discriminator (ID) performance, and the gray bars are the performances of the conventional power-Doppler (PD) estimator for the DC cancellation and FIR clutter filters. (B) Detection efficiency of Doppler methods relative to the ID method. Error bars denote  $\pm 2$  standard errors for 300 trials.

Test statistics reported as conventional power-Doppler estimates were computed using Eq. (2.7). Estimates involved echo data for which either a DC cancellation filter, Eq. (2.8), or a high-pass FIR filter was applied. Ideal discriminator (ID) test statistics were computed using echo data that was unfiltered via Eq. (2.4) or PCA-filtered via Eq. (2.14). We will show in Experiment IV that the only effect PCA filtering has on ID estimator performance is to improve estimation accuracy with a smaller training set. Experiment V illustrates how the ID formalism can be adapted for imaging under the special situation where the covariances are known.

### 2.3.3 Experiment I: Detection

Experiment I provided data to compare perfusion-detection performances of standard power-Doppler and ideal-discriminator approaches. In each case blood-mimicking fluid perfusion measurements were compared to water-perfused control measurements.  $\Sigma_x$  was estimated using a training set of 3000 vectors each of packet size 100 recorded at PRF = 650 Hz.

*Detection* performance is summarized in Fig. 2.6, where testing sets are

composed of 300 echo-signal vectors. Doppler estimator results involved an FIR filter having a high-pass corner frequency that was selected to maximize AUC. Figure 2.6 (A) shows AUC values for the range of perfusion rates tested relative to the corresponding control state. As expected, performance for each estimator improves as flow rates increase because of better separation between the clutter and blood components. Detection performance estimated from power-Doppler versus ideal-discriminator test statistics is summarized by the efficiency measurements shown in Fig. 2.6 (B). At flows below 1 ml/min, PD estimators are less than 50% efficient.

### 2.3.4 Experiment II: Discrimination

Experiment II estimated the efficiency for perfusion discrimination of PD estimators. Here we measured the ability of the power-Doppler method to *discriminate* various perfusion rates when compared to perfusion at 0.1 ml/min in Fig. 2.7 (A) and (B). Comparisons are also made relative to 0.4 ml/min in Fig. 2.7 (C) and (D). Discriminating two perfusion states is more challenging than detection, as quantified by the lower AUC values in Fig. 2.7 (A) and (C) relative those in Fig. 2.6 (A). Along with lower overall AUC values, we find that PD estimators are also less efficient at discrimination than detection.

### 2.3.5 Experiment III: PRF and Frequency Resolution

We expect the pulse-repetition frequency (PRF) to have a different influence on perfusion-detection performance than it does on arterial-flow estimation since aliasing is not a limiting factor in perfusion estimation. For perfusion estimation, the total time spanned by packet samples is very influential because it determines the frequency resolution of a Fourier basis. Conditions that improve frequency resolution also increased the number of samples in the  $B$  eigen-subspace, which improves perfusion discrimination.

Figure 2.8 shows the results of two experiments that demonstrate the value of high-frequency resolution. In Fig. 2.8 (A), we increase the packet size by increasing PRF without changing the total duration of slow-time measurements to find no measurable change in ID detection performance. Conversely, in Fig. 2.8 (B) we fix the packet size at 100 and allow the increase in PRF

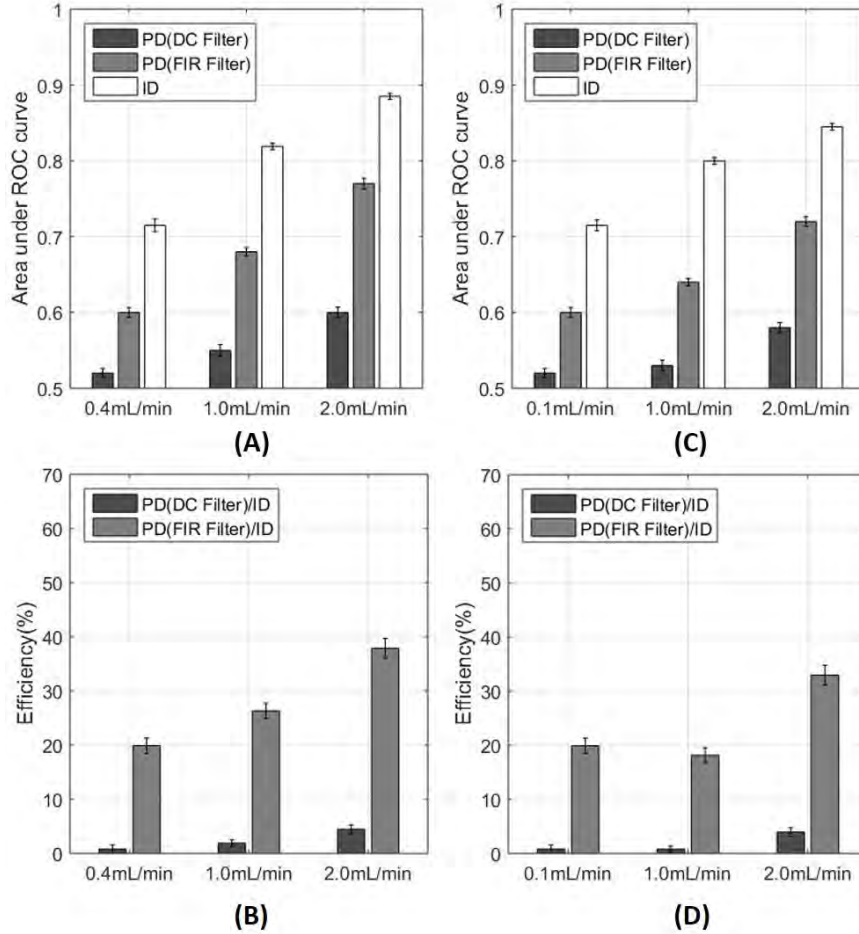


Figure 2.7: (A) Areas under ROC curves (AUCs) for perfusion discrimination using different perfusion rates and estimators. In (A) and (B), state 0 applies blood-mimicking fluid perfusion at a rate of 0.1 ml/min while (C) and (D) use state 0 blood-mimicking fluid perfusion at a rate of 0.4 ml/min. The white bar indicates performance of the ideal-discriminator (ID), and the gray bars are that for the conventional power-Doppler (PD) estimator for the DC cancellation and FIR clutter filters. Results at 0.4 ml/min in (A) and (B) are by definition the same as those at 0.1 ml/min in (C) and (D). Error bars denote  $\pm 2$  standard errors for 300 trials.

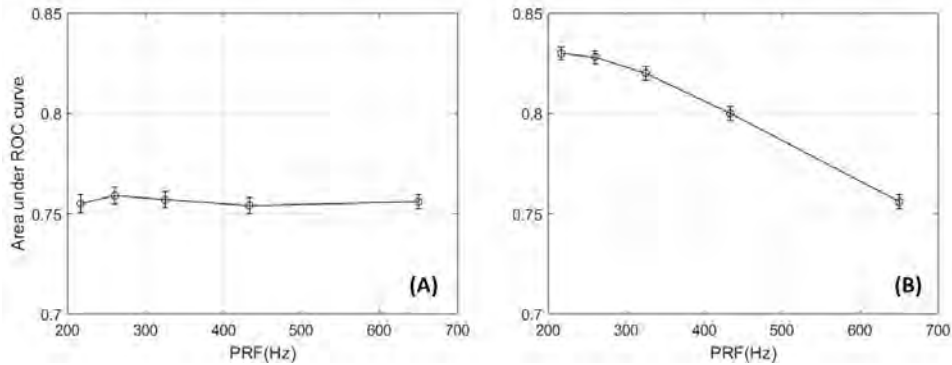


Figure 2.8: Plots of detection AUC at 0.4 ml/min perfusion measured from the ID test statistic as a function of pulse-repetition frequency (PRF). In (A), the total time duration of the echo vector is fixed at 0.1864 s and the vector size varies as  $0.1538 \times \text{PRF}$  pulses. In (B), the vector size is fixed at 100 pulses while time duration varies as  $100/\text{PRF}$  s. Error bars denote  $\pm 2$  standard errors for 300 trials.

to decrease the total duration spanned by the packet. We find performance decreases with the reduction in frequency resolution. The change in AUC between  $\text{PRF} = 217$  Hz (0.83) and 650 Hz (0.76) is modest, but the corresponding change in efficiency via Eq. (2.9) is a factor of 2, which is highly significant. The best performance for perfusion detection and discrimination is found at a PRF less than 1 kHz and the largest packet size that preserves signal ergodicity.

### 2.3.6 Experiment IV: Effects of PCA Filtering

Figure 2.9 illustrates how the number of echo vectors used to estimate the covariance matrix influences ID performance with and without PCA filtering of the training set. In Fig. 2.9 (A), where we used a packet size of 50 pulses, a plateau is reached near  $\text{AUC} \simeq 0.65$ . We only need 400 training vectors to achieve ideal-discriminator performance because the AUC does not increase using a larger number of training vectors. In the plateau region, PCA filtering has no influence on AUC. However, as the number of training vectors falls below 400, we find AUC also falls as errors in covariance estimates increase; below 400 training vectors, we are not estimating the ideal-discriminator response. We see that the reduction in AUC values below 400 vectors is less using PCA-filtered echo signals to estimate  $\Sigma_x$  because we generate fewer

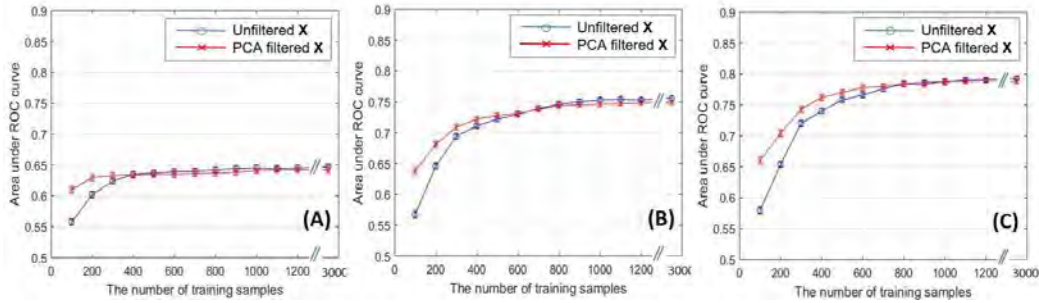


Figure 2.9: Changes in detection AUC at 0.4 ml/min as a function of the number of vectors used to estimate the covariance matrices (training samples) and test-vector length (packet size). Test-vector sizes are (A) 50, (B) 100, and (C) 150 pulses. Points marked (o) are for the ID estimator in which the echoes used to estimate covariance were unfiltered. Points marked (x) use PCA-filtered echo signals. Note that the point at the far right in each plot is for 3000 training vectors. Error bars denote  $\pm 2$  standard errors for 300 trials.

covariance errors by suppressing the clutter and noise components.

Increasing the test vector packet size to 100 in Fig. 2.9 (B) and to 150 in Fig. 2.9 (C) at fixed PRF raises the detection-performance plateau because of increased in frequency resolution. However, we must increase the training set to 800 vectors or more before a plateau is reached.

The data of Fig. 2.9 show that ID performance is not affected by echo-data filtering, although PCA-filtering generates fewer covariance estimation errors leading to performance estimates closer to the ideal discriminator. It also provides evidence that clutter filtering is not fundamental to achieving optimal discriminability when statistical properties of the echo signal are known or can be measured; the need for clutter filtering depends on the requirements of the perfusion estimator adopted.

The following computational times were measured using an Intel processor i5-4300U CPU, 2.50GHz running MATLAB 2013b. The average time to compute  $\mathbf{Q}$  matrices (training) was 0.028 s without PCA filtering and 0.106 s with PCA filtering. The computational time for testing was 0.068 s per data set.

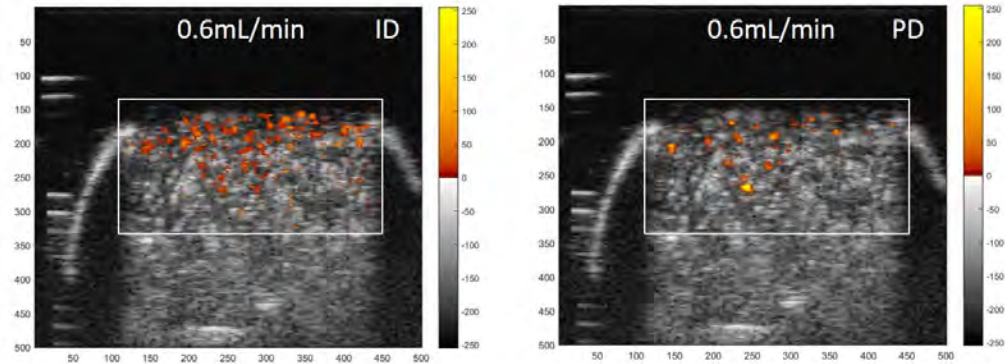


Figure 2.10: Conventional power-Doppler image of phantom perfusion at 0.6 ml/min (right) and that obtained using the ID estimator (left) for the same recorded echo data. Results are coded in color and overlaid on the B-mode image. The image is a cross-sectional view of the dialyzer cartridge diagrammed in Fig. 2.1.

### 2.3.7 Experiment V: Imaging

Figure 2.10 illustrates the effects of lower detection efficiency by comparing standard Doppler estimation with a statistical estimator inspired by the ID approach. Note that this method is only possible because we have training sets of known perfusion rates.

Perfusion was estimated for the phantom of Fig. 2.1 by extending Eq. (2.4) to M-ary hypothesis testing using

$$\ell_k(\mathbf{x}) = \ln \frac{p(\mathbf{x}|k)}{p(\mathbf{x}|0)} \simeq d_k + \mathbf{x}^T \mathbf{Q}_k \mathbf{x}, \quad (2.15)$$

where  $d_k = \log(|\Sigma_{x|0}|/|\Sigma_{x|k}|)$  is the logarithm of the ratio of determinants,  $\mathbf{Q}_k = \Sigma_{x|0}^{-1} - \Sigma_{x|k}^{-1}$  and  $k \in \{1, 2, \dots, 19, 20\}$  denotes the 20 nonzero perfusion states between 0.1 and 2.0 ml/min for which covariances were estimated. The perfusion estimate at each location is found from  $\mathbf{Q}_k$  that maximizes the test statistic,

$$D(\mathbf{x}) = \arg \min_k (\ell_k(\mathbf{x})) . \quad (2.16)$$

The procedure for estimating the covariance matrices is the same as that in Section 2.2.4. Then we estimated  $\ell_k(\mathbf{x})$  for all the test data in the 2-D spatial window shown in Fig. 2.10. Test vectors consist of 40 (200 Hz  $\times$  0.2 s) slow-time echo signals at each window position over a 400-sample axial

range  $((15.4 \text{ mm} \times 20 \text{ samples}/\mu\text{s})/(0.77 \text{ mm}/\mu\text{s})=400 \text{ samples})$  and a 65 scan line lateral range  $((25.8 \text{ mm})/(0.4 \text{ mm}/\text{scanline}) = 65 \text{ scan lines})$ . The total number of test vectors is  $400 \times 65$ , one for each point in the white box of Fig. 2.1, and each test vector has 40 samples. The image on the left side of Fig. 2.10 was obtained by color coding the results of the test vector by Eq. (2.16) at each pixel according to the 20 flow states possible and superimposing those values on the B-mode image. A conventional Doppler image with the same color mapping is shown on the right.

## 2.4 Discussion

The efficiency of conventional power-Doppler methods using FIR clutter filtering for detecting and discriminating perfusion-like blood velocities without contrast enhancement is in the range of 20-50%. This finding suggests there may be more efficient label-free perfusion estimators. If we change acquisition processes to further enhance sensitivity and exploit not only temporal but also spatial statistics, we would find a lower efficiency.

Equation Eq. (2.4) reveals that the strategy of the ideal discriminator is to use the entire covariance matrix in decision making, which is only possible if the states being compared are known statistically. Each echo covariance matrix is a specific combination of properties of the interrogating pulse and scatterer reflectivity and motion. Conventional power Doppler methods do not apply the covariance matrix during the power calculation, meaning they sub-optimally weight echo signals during the squaring and summing process.

Perfusion images are enhanced to reveal flows that are closer to the true value by properly weighting each test vector with covariance information. We demonstrated enhanced flow in the phantom via the image of Fig. 2.10; however, this approach is only possible when the true covariance estimate can be accurately estimated for a known flow condition. Future work includes development of statistical flow estimators that introduce covariance matrix information into the process. Even if the method is sub-optimal, independently validated *in vivo* testing will be able to quantify benefits. Importantly, the methods described in this chapter can be applied to any new estimator to measure its discrimination efficiency and compare those results with standard approaches to evaluate efficacy.

# CHAPTER 3

## MULTIDIMENSIONAL CLUTTER FILTERING USING HOSVD

### 3.1 Introduction

The goal of ultrasonic power Doppler (PD) imaging is to display the magnitude of blood perfusion in tissue at each point in a scan plane. PD methods are sensitive to red-blood-cell (RBC) movements, making them useful for assessing ischemia and flow in tortuous vessels. Nonetheless, quantifying slow and weakly scattering intrinsic perfusion signals remains a formidable challenge. The principal challenge is to increase the signal-to-noise+clutter ratio (SNCR), which is addressed by either suppressing noise and clutter components [40, 25, 28] or augmenting the blood-flow component with contrast agents [8, 41, 9]. Our work focuses on non-contrast-enhanced approaches to improving PD imaging.

We provide an initial demonstration of a simple echo-acquisition and data filtering strategy that appears to substantially improve SNCR and Doppler-frequency resolution. With some tuning of the filters, we clearly see regions of slower perfusion that are not visible using established PD techniques. The acquired data at each spatial location are arranged to have two temporal dimensions: slow-time sampled on the order of kHz and frame-time sampled on the order of Hz. Temporal sampling is adjusted to increase the density of independent samples in the low-frequency Doppler spectrum where the weak perfusion signal is strongest. We then increase the dimension of the clutter filter to fully exploit the expanded dimensionality of the data, and employ high-frequency pulses to further increase SNCR.

The recorded data array initially has two spatial dimensions (axial and lateral) and two temporal dimensions (slow-time and frame-time). These data are reordered to combine the two spatial axes into one, resulting in a 3-D data array with one spatial and two temporal axes. We describe the

information contained within this 3-D data array and a 3-D clutter filter that separates blood components from clutter and noise.

Traditional filters have been employed in the slow-time domain to reduce power at low temporal frequencies where clutter dominates [19]. The resulting perfusion estimates are often averaged over a few spatial locations and/or multiple frames to reduce variance in the estimates. However, under conditions of slow flow, a significant portion of the perfusion signal may fall into the attenuated frequency channels of the clutter filter. This issue is also present for more general eigenfilters that operate on slow-time echo signals [21, 18].

An alternative to 1-D slow-time filters has been to expand the filter dimension to use information from both space and time to isolate the blood signal [40]. Two-dimensional filters are derived from the echo data using singular-value decomposition (SVD). They exploit the spatial coherence of clutter echoes as distinct from the more incoherent flow patterns of perfusion when separating clutter and blood signals. Today, estimation of SVD-filtered data often takes place along the spatial and slow-time axes. If frame-time data are recorded, they are averaged to stabilize the SVD filter. Higher sampling rates along the slow-time axis can be achieved with plane-wave imaging techniques [28] that facilitate noise averaging when forming SVD filters from the data.

We propose here to extend SVD filters to 3-D data arrays described above using a higher-order SVD (HOSVD) technique [42, 43]. We will show data that suggests this filter facilitates isolation of echo power from slowly moving and spatially disorganized RBC movement. HOSVD filter construction yields one set of basis vectors for each of the three data dimensions within a region of interest. Retaining all three data dimensions enables the adaptive HOSVD filter to effectively separate signal components. We hypothesize that by analyzing data along the frame-time axis, we can enhance the sensitivity of PD imaging to blood perfusion echo signals. The challenge for users is to find a subspace in the HOSVD core array that isolates perfusing blood signals. Projecting the recorded echo data onto that subspace before computing the signal power at each pixel dramatically increases PD sensitivity to perfusion. The process of filter formation includes signal averaging that improves filter stability. However, we must take care to select spatial regions that include only wide-sense stationary echo data.

To test the feasibility of the approach, these measurement methods are applied to muscle-perfusion imaging of healthy and ischemic mouse hindlimbs. Perfusion in this model of surgically induced ischemia generates spatial patterns of perfusion/ischemia [44] that we track to observe and compare with alternative approaches.

## 3.2 Methods

### 3.2.1 Notation

The structure of the data array is central to understanding the method. Arrays are described using the following notation. Scalars are written as lower-case letters ( $a, b, \dots$ ), column vectors as bold lower-case letters ( $\mathbf{a}, \mathbf{b}, \dots$ ), matrices as bold capital letters ( $\mathbf{A}, \mathbf{B}, \dots$ ), and multidimensional arrays or *tensors*<sup>1</sup> as bold calligraphic capital letters ( $\mathcal{A}, \mathcal{B}, \dots$ ). Integers  $i, i_1, i_2, i_3$  are indices; e.g., the  $i$ th element of vector  $\mathbf{a}$  is denoted as  $a_i = \mathbf{a}[i]$ , the  $(i_1, i_2)$ th element of matrix  $\mathbf{A}$  as  $a_{i_1, i_2} = \mathbf{A}[i_1, i_2]$ , and the  $(i_1, i_2, i_3)$ th element of third-order tensor  $\mathcal{A}$  as  $a_{i_1, i_2, i_3} = \mathcal{A}[i_1, i_2, i_3]$ .

### 3.2.2 Echo Data Arrays

Doppler-mode acquisition involves the recording of echoes following a series of narrow-band pulse transmissions along one or more scan lines. After each pulse transmission,  $M$  echoes are recorded at fast-time sampling interval  $T$  (Fig. 3.1). Let  $\mathbf{x}$  represent the complex envelope of the recorded echo signal, i.e., the demodulated analytic signal [45]. Each element of  $M \times 1$  vector  $\mathbf{x}$  is a complex number with real and imaginary components given by in-phase and quadrature values. The  $m$ th fast-time sample, for  $1 \leq m \leq M$ , corresponds to axial depth  $z = z_0 + (m - 1)cT/2$  where  $z_0$  is the distance between the transducer surface and the beginning of the recorded signal, and  $c$  is the compressional wave speed.

---

<sup>1</sup>We use the term *tensor* to be consistent with the HOSVD literature. However, in our usage, the term does not imply anything about the transformation properties of the multidimensional data arrays.

For each line of site, echo vectors are recorded  $N$  times following each of  $N$  pulse transmissions to form a packet of echo data. Pulses are transmitted on the slow-time interval  $T' > MT$ , where  $1/T'$  is the pulse repetition frequency (PRF). Conventional power and color Doppler acquisitions record a packet of echo data for each of  $L$  adjacent lines of sight separated laterally by the spatial interval  $D$ . All packets for one spatial frame form an  $(N \times M \times L)$  array of echo data that we call a *Doppler frame*. This conventional 3-D array represents two spatial dimensions and a slow-time dimension.

$K$  Doppler frames are recorded on the time interval  $T'' \gg T'$  to generate the frame-time dimension of a 4-D data array. To measure perfusion, we set  $T = 0.042 \mu\text{s}$  (24 Msamples/s fast-time sampling rate),  $T' = 1 \text{ ms}$  (PRF = 1 kHz), and  $T'' = 0.11 \text{ s}$  (frame-repetition frequency = 9 Hz). This 4-D data array is represented by  $\tilde{\mathcal{X}} \in \mathbb{C}^{N \times M \times L \times K}$ .

The second and third dimensions of  $\tilde{\mathcal{X}}$  are associated with axial and lateral spatial domain, respectively, that are not separately analyzed. Therefore the array is reordered as follows:

$$\mathcal{X} \in \mathbb{C}^{N \times S \times K}, \text{ such that } x_{n,s,k} = \tilde{x}_{n,m,l,k}, \quad (3.1)$$

where  $s = m + (l - 1)M$  and  $S = ML$ .

The common assumption is that echo data arise from three independent physical sources: tissue clutter  $\mathcal{C}$ , blood scattering  $\mathcal{B}$ , and acquisition noise  $\mathcal{N}$ . Thus,  $\mathcal{X}$  has three components,

$$\mathcal{X} = \mathcal{C} + \mathcal{B} + \mathcal{N}, \quad (3.2)$$

where each has size  $N \times S \times K$ . White acquisition noise ensures that  $\mathcal{X}$  is full-rank. Finally,  $\mathcal{B}$  includes signals from fast arterial flow and slow capillary perfusion.

### 3.2.3 Eigen-based Filters

For echo data well represented by a zero-mean Gaussian process, the correlation (and covariance) matrix contains all of the statistical information for that vector space. Eigenfilters decompose the multidimensional data array using eigenvectors of the correlation matrix. These eigenvectors are orthogonal

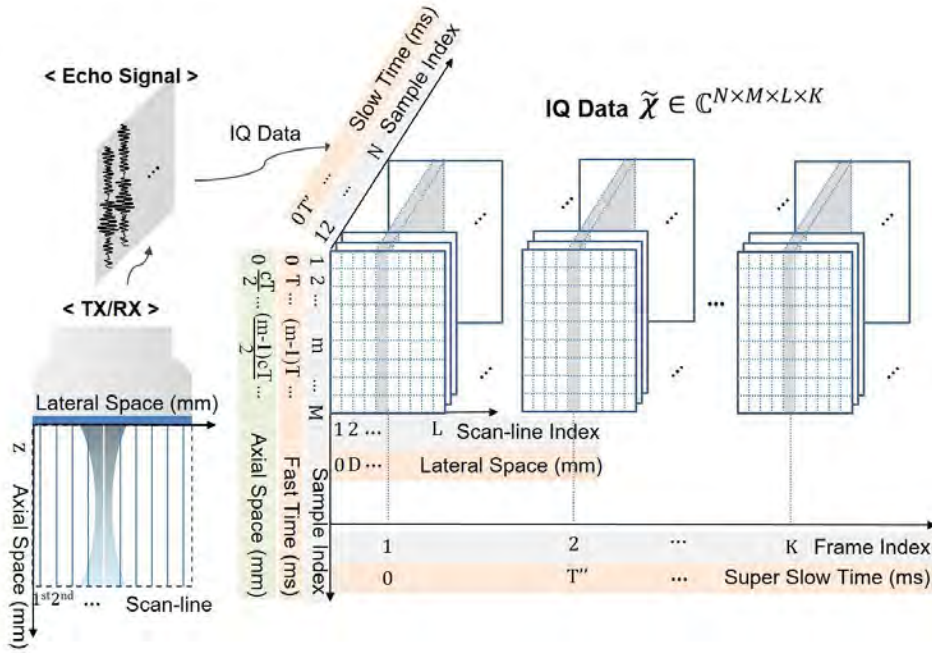


Figure 3.1: Data acquisition is illustrated. One IQ echo vector is recorded for each pulse transmission. The fast-time sampling interval is  $T$  generating an  $M \times 1$  vector.  $N$  echo vectors are recorded with interval  $T'$  at each line of site. Repeating the acquisition process over  $L$  lateral lines of site with spatial interval  $D$  makes one Doppler frame array. Recording  $K$  frames at time interval  $T''$  results in the 4-D array of IQ echo data  $\tilde{\mathcal{X}} \in \mathbb{C}^{N \times M \times L \times K}$ . The array is reformed as a 3rd-order tensor  $\mathcal{X} \in \mathbb{C}^{N \times S \times K}$  where  $S = ML$ .

and uncorrelated, and, under the Gaussian assumption, their eigencomponents are as statistically independent as possible. An eigenvalue divided by the sum of all eigenvalues describes the fraction of variance contributed by that eigenmode. Because tissue scattering is often more echogenic than blood scattering, and both contribute more to the variance than noise, the common assumption is that clutter dominates the first few eigenvalues, blood the next few, and the rest are noise. Eigen-based filters isolate the blood subspace by identifying the clutter-blood and blood-noise interfaces and suppressing eigenvalues outside the blood subspace [17, 18, 28]. The method used to construct the filter depends on how many of the data dimensions we choose to apply, as we now explain.

### 1st-order Eigen-based Filter

Let  $\mathbf{X} \in \mathbb{C}^{N \times S}$  be a matrix indicating the  $\alpha$ th Doppler frame of echo data such that  $\mathbf{X} = \mathcal{X}_{i_3=\alpha}$ ,  $\alpha \in \{1, \dots, K\}$ . An empirical correlation matrix of the *temporal signal* can be computed and then decomposed as follows.

$$\mathbf{R}_N = \mathbf{X}\mathbf{X}^\dagger = \mathbf{U}\mathbf{\Lambda}\mathbf{U}^\dagger \in \mathbb{C}^{N \times N}, \quad (3.3)$$

where  $\dagger$  denotes conjugate transpose.  $\mathbf{\Lambda}$  is a diagonal matrix of eigenvalues sorted in descending order. The columns of unitary matrix  $\mathbf{U} = [\mathbf{u}_1, \dots, \mathbf{u}_N]$  are the corresponding eigenvectors for  $\mathbf{R}_N$ . From Eq. (3.3),  $\mathbf{X}$  is easily decomposed in terms of temporal eigenvectors using

$$\mathbf{X} = \mathbf{U}\mathbf{U}^\dagger\mathbf{X} = \sum_{i=1}^N \mathbf{u}_i\mathbf{u}_i^\dagger\mathbf{X}. \quad (3.4)$$

Identifying the rank of the clutter and blood subspaces by  $c$  and  $b$ , respectively, data are processed using the 1-D eigen-based clutter filter,

$$\hat{\mathbf{B}} = \sum_{i=c+1}^{c+b} \mathbf{u}_i\mathbf{u}_i^\dagger\mathbf{X}. \quad (3.5)$$

That is, only those eigenvectors associated with the blood subspace are used to resynthesize the decomposed echo data, which is now represented by matrix  $\hat{\mathbf{B}}$ . Subsequently, the power  $\hat{\mathbf{B}}$  is mapped into the PD image.

Note that when the echo signals are wide-sense stationary and the impulse response for the pulse-echo system is linear time-invariant such that the system matrix is well approximated by a circulant matrix, then the eigenfilter components are equal to Fourier components. The difference is that finite-impulse response (FIR) clutter filters are generally fixed over the imaged region while the eigenfilter described by Eq. (3.5) adapts to the echo data.

Similarly, an empirical correlation matrix of the *spatial signal* can be computed and then decomposed using

$$\mathbf{R}_S = \mathbf{X}^\dagger\mathbf{X} = \mathbf{V}\mathbf{\Lambda}'\mathbf{V}^\dagger \in \mathbb{C}^{S \times S}, \quad (3.6)$$

where eigenvalue matrix  $\mathbf{\Lambda}'$  has a different size but contains the same non-trivial eigenvalues as  $\mathbf{\Lambda}$  in Eq. (3.3). The columns of unitary matrix  $\mathbf{V} =$

$[\mathbf{v}_1, \dots, \mathbf{v}_S]$  are eigenvectors in the spatial domain. Equation (3.6) is not typically used for power estimation although it is an important component of the second-order filters described below.

### 2nd-order Eigen-based Filter

SVD is an analogous tool for decomposing data spanning two vector spaces, in this case time and space. Matrix  $\mathbf{X} \in \mathbb{C}^{N \times S}$  is decomposed using

$$\mathbf{X} = \mathbf{U}\mathbf{\Sigma}\mathbf{V}^\dagger = \sum_{i=1}^r \sigma_i \mathbf{u}_i \mathbf{v}_i^\dagger. \quad (3.7)$$

This form of  $\mathbf{X}$  is known as the Casorati matrix [28], whose rows comprise vectorized frames of the image series.<sup>2</sup> Assuming white acquisition noise, the rank of  $\mathbf{X}$  is  $r = \min(N, S)$ , which is also the rank of  $\mathbf{\Sigma} \in \mathbb{R}^{N \times S}$ , a diagonal matrix of singular values  $\sigma_i$  sorted in descending order. Analogous to Eq. (3.5), the best estimation of the blood-signal matrix, in a least-squared sense [28], is found by processing

$$\hat{\mathbf{B}} = \sum_{i=c+1}^{c+b} \sigma_i \mathbf{u}_i \mathbf{v}_i^\dagger = \sum_{i=c+1}^{c+b} \mathbf{u}_i \mathbf{u}_i^\dagger \mathbf{X} \mathbf{v}_i \mathbf{v}_i^\dagger. \quad (3.8)$$

Equations (3.5) and (3.8) both seek to identify the blood component of echo-signal variance along the slow-time dimension.  $N$  is typically small, which may not provide enough eigenmodes to uniquely identify the blood-scattering subspace given the similarity of perfusion and clutter velocities. Adding frame-time samples increases the number of eigenmodes in a way that also increases the SNCR.

Power contained in filtered data  $\hat{\mathbf{B}} \in \mathbb{C}^{N \times S}$  is computed using

$$\mathbf{p}[i_2] = \frac{1}{N} \sum_{i_1=1}^N |\hat{\mathbf{B}}[i_1, i_2]|^2, \quad (3.9)$$

---

<sup>2</sup>Liang [46] showed that the spatiotemporal components of a Casorati matrix are at least partially separable if  $\mathbf{X}$  is low rank. With white acquisition noise,  $\mathbf{X}$  is always full rank, and yet for echo SNR  $\gtrsim 20$  dB the rank of the clutter and blood subspaces is much less than the rank of  $\mathbf{X}$ .

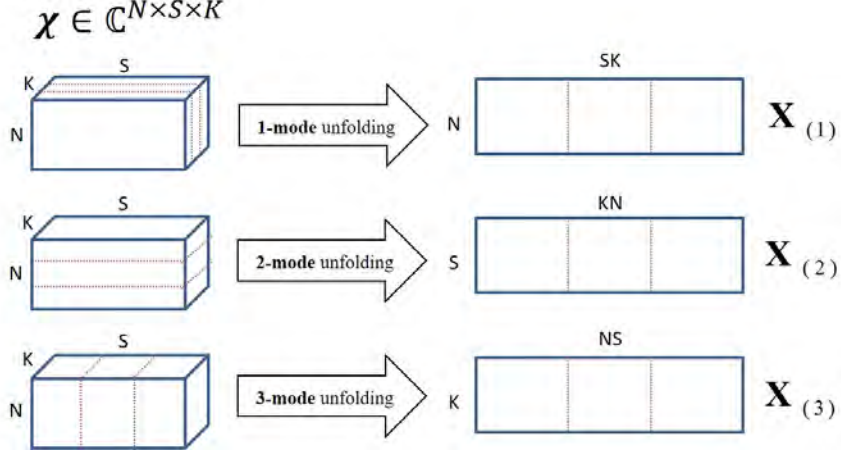


Figure 3.2: The figure illustrates 1, 2 and 3-mode unfolding operation of the 3rd-order tensor data  $\mathcal{X}$ .

where  $\mathbf{p} \in \mathbb{R}^S$  can be converted into an image  $\mathbf{P} \in \mathbb{R}^{M \times L}$ . Power estimates are log compressed and scan converted when displaying the image for the  $\alpha$ th frame acquired.

### 3rd-order Eigen-based Filter

SVD methods can be extended to 3-D data by decomposing  $\mathcal{X} \in \mathbb{C}^{N \times S \times K}$  into three empirical correlation matrices. First, consider the following related to tensor processing:

- *Unfolding.* A 1-mode unfolding operator  $\mathbf{X}_{(1)} = [\mathcal{X}]_1$  arranges elements of tensor  $\mathcal{X} \in \mathbb{C}^{N \times S \times K}$  into a matrix  $\mathbf{X}_{(1)} \in \mathbb{C}^{N \times SK}$  where columns of the matrix are slow-time signals. Likewise, 2-mode and 3-mode unfoldings generate the matrix  $\mathbf{X}_{(2)} \in \mathbb{C}^{S \times KN}$  and  $\mathbf{X}_{(3)} \in \mathbb{C}^{K \times NS}$  where columns of the matrices are space and frame-time signals, respectively. These are illustrated in Fig. 3.2.
- *Empirical correlation matrices* are found using the unfoldings as follows:

$$\begin{aligned}
 \mathbf{R}_N &= [\mathcal{X}]_1 [\mathcal{X}]_1^\dagger = \mathbf{U} \mathbf{\Lambda}_N \mathbf{U}^\dagger \in \mathbb{C}^{N \times N} \\
 \mathbf{R}_S &= [\mathcal{X}]_2 [\mathcal{X}]_2^\dagger = \mathbf{V} \mathbf{\Lambda}_S \mathbf{V}^\dagger \in \mathbb{C}^{S \times S} \\
 \mathbf{R}_K &= [\mathcal{X}]_3 [\mathcal{X}]_3^\dagger = \mathbf{W} \mathbf{\Lambda}_K \mathbf{W}^\dagger \in \mathbb{C}^{K \times K} .
 \end{aligned} \tag{3.10}$$

Subscripts on the correlation matrices indicate the  $\mathcal{X}$  dimension preserved.  $\mathbf{\Lambda}_N$ ,  $\mathbf{\Lambda}_S$  and  $\mathbf{\Lambda}_K$  are diagonal eigenvalue matrices for the three modes, and  $\mathbf{U}$ ,  $\mathbf{V}$  and  $\mathbf{W}$  are the corresponding eigenvector matrices.

- *n-mode rank* of tensor  $\mathcal{X}$  equals the rank of the matrix generated by n-mode unfolding,

$$r_n(\mathcal{X}) = r([\mathcal{X}]_n), \quad n \in \{1, 2, 3\}. \quad (3.11)$$

Thus, 1-mode, 2-mode and 3-mode rank of  $\mathcal{X}$  is the same as the rank of  $\mathbf{R}_N$ ,  $\mathbf{R}_S$  and  $\mathbf{R}_K$ .

Analogous to Eq. (3.7), the HOSVD of  $\mathcal{X}$  is

$$\begin{aligned} \mathcal{X} &= \mathcal{G} \times_1 \mathbf{U} \times_2 \mathbf{V} \times_3 \mathbf{W} \\ &= \sum_{i_1=1}^{r_1} \sum_{i_2=1}^{r_2} \sum_{i_3=1}^{r_3} g_{i_1, i_2, i_3} \mathbf{u}_{i_1} \times \mathbf{v}_{i_2} \times \mathbf{w}_{i_3}, \end{aligned} \quad (3.12)$$

where  $\times$  denotes an outer-product operation. See Section 3.2.4 for an element-based description of the outer products.

$\mathcal{G} \in \mathbb{C}^{N \times S \times K}$  is a ‘‘core tensor’’ analogous to matrix  $\mathbf{\Sigma}$  in Eq. (3.7). The columns of  $\mathbf{U}$ ,  $\mathbf{V}$  and  $\mathbf{W}$  are the eigenvectors for the slow-time, spatial and frame-time dimensions, respectively. Also  $r_1$ ,  $r_2$ , and  $r_3$  are the n-mode ranks of  $\mathcal{G}$ .  $\mathcal{G}$  is computed using the unitary property of eigenvector matrices,

$$\mathcal{G} = \mathcal{X} \times_1 \mathbf{U}^\dagger \times_2 \mathbf{V}^\dagger \times_3 \mathbf{W}^\dagger. \quad (3.13)$$

Components of  $\mathcal{G}$  are orthogonal in that the dot product between planes in the array,

$$\langle \mathcal{G}_{i_n=\alpha}, \mathcal{G}_{i_n=\beta} \rangle = 0, \quad \alpha \neq \beta, \forall n, \forall \alpha, \forall \beta, \quad (3.14)$$

and the squared norm of matrix  $\|\mathcal{G}_{i_n=j}\|^2$  equals a  $j$ th largest eigenvalue of  $\mathbf{R}_n$  for  $n = 1, 2, 3$ .

HOSVD filtering is analogous to that described for SVD filtering in Eq. (3.8). However, note that the 1,2,3-mode rank of  $\mathcal{X}$  are not necessarily the same, and its core tensor  $\mathcal{G}$  is not diagonal [42, 43]. Thus, an advantage of HOSVD filtering is the added flexibility in defining the rank of the clutter and blood subspaces.

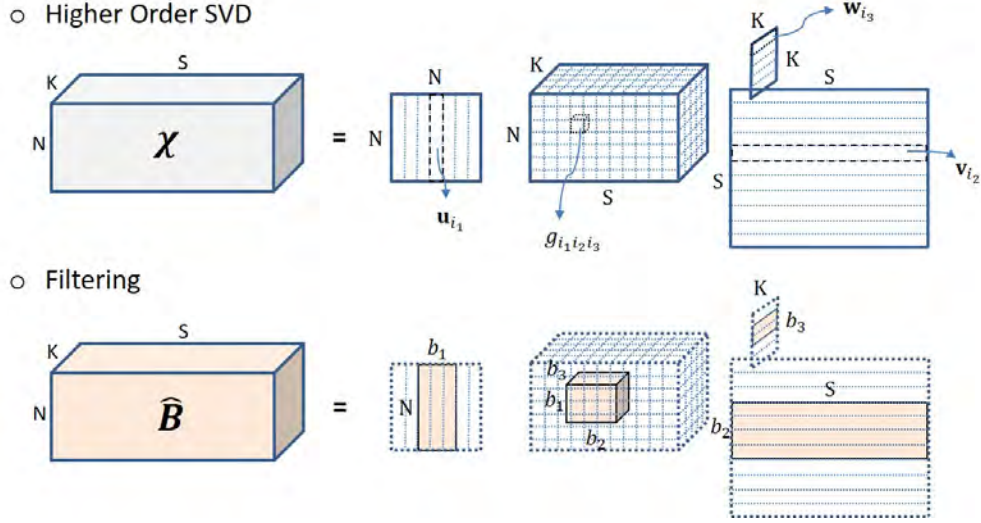


Figure 3.3: The top diagram describes HOSVD applied to 3rd-order tensor data  $\mathcal{X}$ . The bottom diagram illustrates a region in the core tensor being selected to isolate the blood-perfusion signal.

The HOSVD filter applied to  $\mathcal{X}$  (Fig. 3.3) yields the filtered echo-signal tensor,

$$\begin{aligned}
 \hat{\mathcal{B}} &= \sum_{i_1=c_1+1}^{c_1+b_1} \sum_{i_2=c_2+1}^{c_2+b_2} \sum_{i_3=c_3+1}^{c_3+b_3} g_{i_1,i_2,i_3} \mathbf{u}_{i_1} \times \mathbf{v}_{i_2} \times \mathbf{w}_{i_3} \\
 &= \sum_{i_1=c_1+1}^{c_1+b_1} \sum_{i_2=c_2+1}^{c_2+b_2} \sum_{i_3=c_3+1}^{c_3+b_3} \mathcal{X} \times_1 \mathbf{u}_{i_1} \mathbf{u}_{i_1}^\dagger \\
 &\quad \times_2 \mathbf{v}_{i_2} \mathbf{v}_{i_2}^\dagger \times_3 \mathbf{w}_{i_3} \mathbf{w}_{i_3}^\dagger. \tag{3.15}
 \end{aligned}$$

Constants  $c_n$  and  $b_n$  are, respectively, the ranks of the clutter and blood subspaces on  $i$ -th mode eigenspace. Section 3.4 describes an approach to finding 3-D regions within the  $\mathcal{G}$  array that best represents the blood components of echo power.

In contrast to Eqs. (3.5) and (3.8), which were analyzed by others [17], the rank reduction provided by HOSVD filtering in Eq. (3.15) is not optimal in the least-squares sense [47]. That is, the mean-square error between  $\mathcal{X}$  and one or more signal components may not be minimized by this filter. Nevertheless, it is a good approximation and can be implemented more simply and quickly than that of iterative methods that can obtain the least-squares solution [48].

### 3.2.4 Explanation of Outer-Product Notation

This subsection briefly explains the outer-product notation used in Eq. (3.12).

The  $n$ -mode outer product of  $I_N$ -dimensional tensor  $\mathcal{A}$  and matrix  $\mathbf{Z}$  is

$$\begin{aligned}\mathcal{D} = \mathcal{A} \times_n \mathbf{Z} &\in \mathbb{C}^{I_1 \times \dots \times I_{n-1} \times J_n \times I_{n+1} \times \dots \times I_N} \\ \mathcal{A} &\in \mathbb{C}^{I_1 \times I_2 \times \dots \times I_{n-1} \times I_n \times I_{n+1} \times \dots \times I_N} \\ \mathbf{Z} &\in \mathbb{C}^{J_n \times I_n},\end{aligned}$$

where an element of tensor  $\mathcal{D}$  is

$$d_{i_1 \dots i_{n-1} j_n i_{n+1} \dots i_N} = \sum_{i_n=1}^{I_n} a_{i_1 \dots i_N} z_{j_n i_n}.$$

The  $(\ell_1, \ell_2, \ell_3)$ -th element of  $\mathcal{X} \in \mathbb{C}^{N \times S \times K}$  is

$$x_{\ell_1, \ell_2, \ell_3} = \sum_{i_1=1}^N \sum_{i_2=1}^S \sum_{i_3=1}^K g_{i_1, i_2, i_3} u_{\ell_1, i_1} v_{\ell_2, i_2} w_{\ell_3, i_3},$$

which corresponds to a second line of Eq. (3.12).

### 3.2.5 Implementation

We assume perfusion is constant over the 17 slow-time samples (17 ms) recorded in this study. However the echo-signal mean and covariance matrix in the unfolded  $\mathcal{X}$ , e.g., Eq. (3.10), do vary over the  $6.4 \text{ mm} \times 14.4 \text{ mm} \rightarrow 200 \times 240 = 48,000$  spatial samples and over the 17 frame-time samples (1.9 s) typically applied to each PD image. Although we record 100 frames (11.1 s), blocks of 17 frames are applied to any one estimate. See Table 3.1 for data acquisition details. Since the number of spatial samples is much larger than either of the time samples, the data are spatially windowed to compute local filters. In this way, HOSVD filters adapt to properties of recorded data along any of the array axes.

Beginning with the 4-D array  $\tilde{\mathcal{X}} \in \mathbb{C}^{N \times M \times L \times K}$ , spatial window  $\Omega_j$  of size  $N \times \dot{M} \times \dot{L} \times \dot{K}$  is applied  $J$  times to  $\tilde{\mathcal{X}}$  to make one PD image. Data within the  $j$ th window are rearranged into  $\mathcal{X}_j \in \mathbb{C}^{N \times \dot{S} \times \dot{K}} = \mathbb{C}^{17 \times 224 \times 17}$ , where  $\dot{S} = \dot{M}\dot{L}$  for  $\dot{M} = 14$  and  $\dot{L} = 16$  samples. Each overlaps adjacent

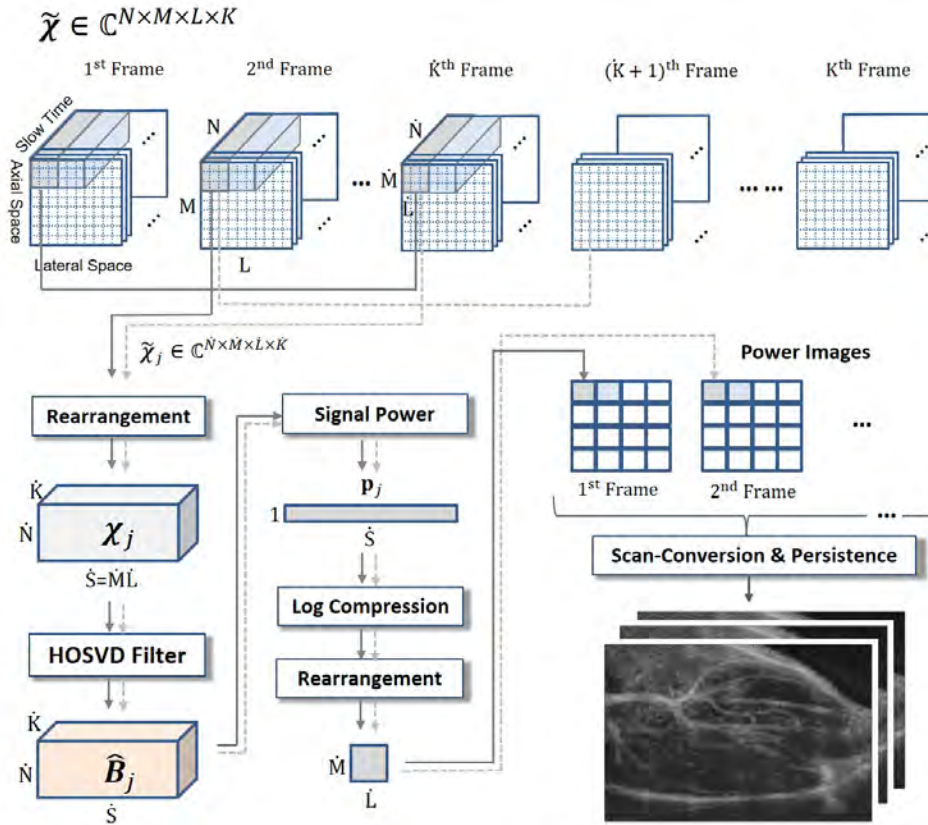


Figure 3.4: The sequence of operations leading to the formation of a perfusion image is illustrated. The acquisition data within each window is individually processed. HOSVD filtering isolates the blood-scattering components of the echo signal. Echo power is computed by averaging over slow-time and frame-time axes. The log-compressed power value is assigned a spatial position in the PD image.

windows by 0.13 mm axially and 0.24 mm laterally. A total of  $J = 1600$  spatial windows and filters were applied per 6.4 mm×14.4 mm PD image. We also window data along the frame-time axis if we wish to implement a dynamic sequence of images. Figure 3.4 offers a graphical summary.

Similar to Eq. (3.9), the post-filtration signal power within windowed data  $\tilde{\mathcal{B}}_j \in \mathbb{C}^{N \times \dot{S} \times \dot{K}}$  is computed using

$$\mathbf{p}_j[i_2] = \frac{1}{N\dot{K}} \sum_{i_1=1}^N \sum_{i_3=1}^{\dot{K}} |\tilde{\mathcal{B}}_j[i_1, i_2, i_3]|^2, \quad (3.16)$$

where  $\mathbf{p}_j \in \mathbb{R}^{\dot{S}}$ . The elements of vector  $\mathbf{p}_j$  are log-compressed and scan converted into a spatial segment of size  $\dot{M} \times \dot{L}$ . These segments are then assembled into a PD image. Final images may sum sequential PD frames formed along the frame-time axis or display them as a dynamic sequence with adjustable persistence. The latter is preferred if perfusion varies over the acquisition time.

In summary, three eigenanalyses are performed on  $\mathcal{X}$  via Eq. (3.10). From the three sets of eigenvectors generated, the core tensor is formed via Eq. (3.13). We then select a region within the core tensor that contains information about perfusion and zero the other elements via Eq. (3.15). This process yields the perfusion subspace whose elements are squared and summed in Eq. (3.16) to estimate the signal power mapped into PD images. *In vivo* experiments discussed below show that the perfusion subspace is confined to a small region within  $\mathcal{G}$ . Therefore we find it is fast and easy to exhaustively search for values of  $c_n$  and  $b_n$  in Eq. (3.15) that yield the “best” perfusion maps shown in the results below.

Echo data were recorded using a Vevo<sup>®</sup> 2100 system and a MS400 linear array (FUJIFILM VisualSonics Inc. Toronto, Ontario, Canada). The transducer transmits 2-cycle pulses with a 24 MHz center frequency. All processing was implemented in MATLAB 2013b on an Intel processor i5-4300U CPU, 2.50 GHz. The highest computational burden is filter construction, which was performed using a truncation technique [49] to minimize running time. The average time to compute the 1600 windows for one PD image frame is 19.1 s.

Table 3.1: Acquisition parameters

Parameter	Value
System	Visualsonics Vevo 2100
Probe type	MS 400
Pulse center frequency	24.0 MHz
Doppler pulse length	2 cycles
Fast-time samples size (Axial length)	200-272 (6.4-8.7 mm)
Fast-time sampling rate	24.0 MHz
Slow-time samples size (Scan time)	17 (0.017 ms)
Slow-time sampling rate	1.0 kHz
Frame-time samples size (Scan time)	100 (11 s)
Frame-time sampling rate	9 Hz
Scan-line numbers (lateral length)	240-250 (14.40-15.00 mm)
Scan-line density	16.67 lines/mm

### 3.2.6 *In vivo* Perfusion Imaging

A murine model of partial hindlimb ischemia was used [50] to study the feasibility of our methods for *in vivo* perfusion imaging (Fig. 3.5). Each mouse was anesthetized with 1.5% isoflurane vaporized in O<sub>2</sub> at a rate of 1 L/min via nose cone. Each animal underwent hindlimb occlusion of the right femoral artery, following the procedure described previously in [50, 44] without disturbing non-femoral peripheral flow to the right leg or any blood flow to the left leg. Briefly, the anesthetized mouse was placed on a 37 °C heating pad, a small incision was made on the right leg to expose the femoral vasculature, and dual ligation of the femoral artery was performed distal to the profundus branch to induce unilateral hindlimb ischemia. To confirm the occlusion and the reduction of blood flow in ischemic hindlimb, animals were imaged with a Laser Doppler Imager (moorLDI, Moor Instruments, UK) before, and immediately after ligation. For US scanning at 24 hrs post-surgery, the anesthetized animal was placed in a supine position with hindlimbs extended, and the transducer scanned the shaved inner hindlimb along a longitudinal cross section that included muscle, bone and vasculature.

Figure 3.5 (B) displays a B-mode view of the anatomy. Although measurements were made on three mice, we will show results of scanning contralateral limbs of two mice specifically to compare methods. All experiments were performed with the approval of the Institutional Animal Care and Use Committee of the University of Illinois at Urbana-Champaign following the

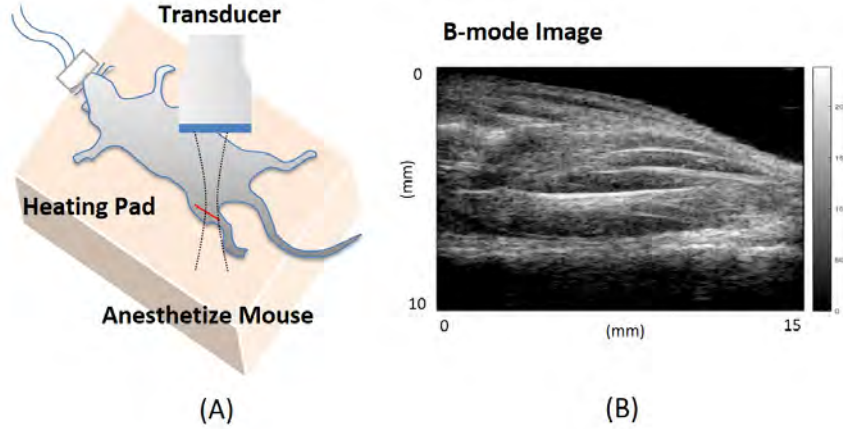


Figure 3.5: (A) An anesthetized mouse placed on a heated surface in a supine position is scanned with a linear array. (B) A longitudinal cross section of the hindlimb is displayed as a B-mode image.

principles outlined by the American Physiological Society on research animal use.

### 3.3 Results

We recorded 100 sequential Doppler frames (11.1 s) from the right (ischemic) and left (healthy control) hindlimbs one day after right femoral-artery ligation. Only the first 17 frames are included in each of the PD images shown below. Images in Figs. 3.6 - 3.10 are from one animal, while the left image in Fig. 3.11 is from a second animal undergoing identical procedures.

#### 3.3.1 First-order Filter

We begin by processing only the first Doppler frame in the array; specifically,  $\mathbf{X} = \mathbf{x}_{i_3=1} \in \mathbb{C}^{17 \times 200 \cdot 240 \times 1}$ . Applying the spatial window described in Section 3.2.5, the data matrix used to form the  $j$ th spatial window for first-order eigenfilters was  $\mathbf{X}_j \in \mathbb{C}^{17 \times 14 \cdot 16}$ . Computing the temporal correlation matrix in Eq. (3.3) and filtering the data using Eq. (3.5), we constructed the perfusion images found in Fig. 3.6.

The first row of Fig. 3.6, (A) and (B), displays images obtained without filtering to show the full clutter component in the PD signal. Arrows indi-

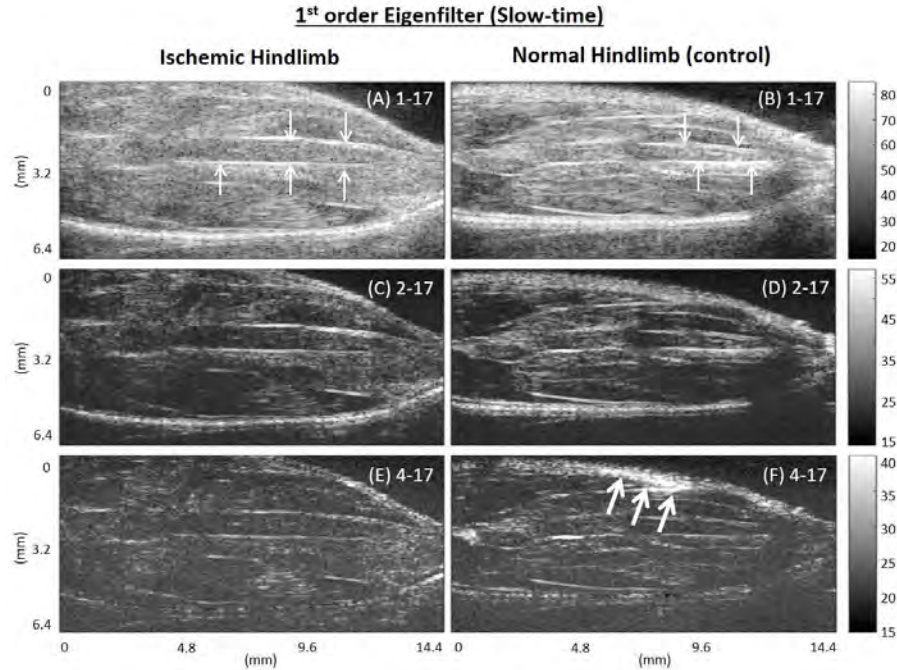


Figure 3.6: Power Doppler (PD) images are shown without a B-mode component. These images are formed using a first-order eigenfilter and slow-time eigenbases. Left and right columns are images of ischemic and normal hindlimbs, respectively. Thin arrows indicate bone echoes and thick arrows indicate fast arterial flow. The numbers at the top of each image indicate the range of indices passed through the filter in the summation of Eq. (3.5). Since the possible range is 1-17, lower rows are more heavily filtered images.

cate echoes from bone surfaces. The second row, (C) and (D), shows filtered images formed by discarding the first (most energetic) slow-time eigencomponent and preserving eigencomponents 2-17. Third row images, (E) and (F), discard the first three slow-time eigencomponents, leaving 4-17. Discarding the three most energetic eigenvalues removes many of the clutter echoes from both images, although the bone reflections remain. More importantly, there is no apparent discriminability between the ischemic and control states except for the appearance of a segment of arterial flow as indicated by the larger arrows in (F) near the proximal skin surface of the control hindlimb.

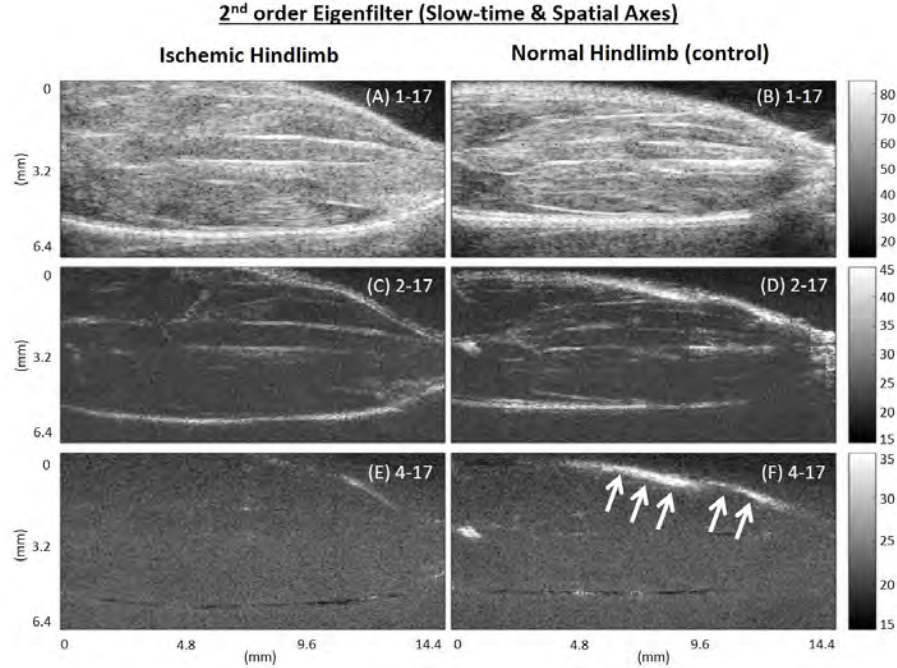


Figure 3.7: PD images using a 2nd-order SVD filter based on slow-time and spatial eigenbases to show primarily arterial flow. Left and right columns are images of ischemic and normal hindlimbs, respectively. Thick arrows indicate a region with fast arterial flow. The numbers at the top of each image indicate the range of indices passed through the filter in the summation of Eq. (3.8). Possible range: 1-17.

### 3.3.2 Second-order Filter

The same data were processed by the second-order SVD filter via Eq. (3.8). Figure 3.7 shows the resulting PD images using slow-time and spatial eigenbases. As in Fig. 3.6, the three rows describe three levels of filtering given by numbers in the upper right corner. Virtually all echoes are eliminated in images (E) and (F) except for the arterial flow near the skin surface in the control hindlimb. Comparing Figs. 3.6 and 3.7, we see the effectiveness of including the spatial axis of the data array for clutter suppression. However, the slow-time axis offers very little sensitivity to perfusion signals; the remaining signal power indicates a segment of arterial flow (arrows).

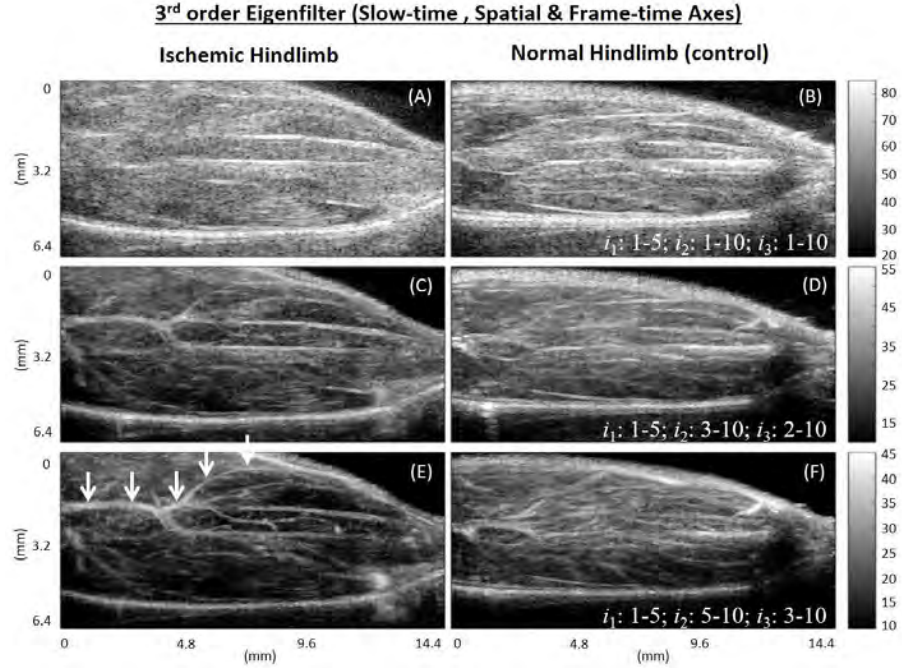


Figure 3.8: PD images using the full 3-D data array and HOSVD filter to show perfusion. Left and right columns are images of ischemic and normal hindlimbs, respectively. Filter parameters shown at the bottom of an image apply to the normal and ischemic images in that row. As filter parameters change, vascular structures emerge (arrows in (E) point to one branch) while clutter and noise components fade. The normal flow image (F) is uniformly perfused, although the signal strength near the bottom surface of the leg is low because of acoustic attenuation. In contrast, the ischemic hindlimb in (E) with lost femoral-arterial flow shows perfusion-deficit patches and prominent vessels that now contain low-speed blood flow from the remaining peripheral vessels. Note that the same echo data are used to form images in Figs. 3.6 – 3.8.

### 3.3.3 Third-order Filter

We again analyzed the same echo data array but now employing all three dimension using the HOSVD filters of Eq. (3.15). In the bottom row of Fig. 3.8, we see the emergence of vascular structures that are not at all apparent with 1-D and 2-D filters in Figs. 3.6 and 3.7. There are three sets of filter indices,  $i_1, i_2, i_3$ , that specify the ranges in  $\mathcal{G}$  passed by the 3-D filter. These are given at the bottom of the images, where values shown apply to both images in that row. Here we see perfusion and slow vascular flow but very little fast flow or clutter. The advantages brought to bear in these result

are threefold. First, the use of frame-time data enhances SNCR for perfusion. Second, employing all three data-array axes increases the effectiveness of clutter filtering. Third, we use more data than that applied to the results of Figs. 3.6 and 3.7, which greatly suppresses acquisition noise.

In Fig. 3.9, we compare results of first-, second-, and third-order clutter filters for displaying the slow-time arterial flow (first three rows of images) and frame-time perfusion (last three rows of images). All results are obtained from the same echo-data array, viz.,  $\mathbf{x} \in \mathbb{C}^{17 \times 200 \cdot 240 \times 17}$ . For the first- and second-order filters, 17 post-filtered images are averaged over either the slow-time or the frame-time axes to take full advantage of all echo data. The third-order filter first decomposes the entire data array before projecting onto the appropriate subspace. The entire echo-data array influences each image displayed in Fig. 3.9. In each case, we selected filter parameters that provided the clearest visualization of RBC movement. From one set of recorded echo data, we can see the effects of filter order and data-array axis (eigenbasis) on the ability to visualize fast or slow-flow patterns in normal and ischemic hindlimbs. In particular, compare the noise levels in the third-order filter results with first and second-order results. A noticeable contrast improvement is observed.

The full impact of using 3-D data may be appreciated when we threshold and color code the power signals before overlaying them on the B-mode image (Fig. 3.10) as is traditionally displayed for clinical applications. We use a blue color map to display the slow-time-axis power (arterial flows) seen in Figs. 3.9 (E) and (F) and a red color map to display the frame-time-axis power (blood perfusion) from Figs. 3.9 (K) and (L). Colored PD images are displayed in the third row of Fig. 3.10. The inset shows 160  $\mu\text{m}$ -dia vessels are clearly resolved.

The first and second rows of Fig. 3.10 display FIR-filtered PD images, and the third row shows HOSVD-filtered images. All are computed from the same echo-data array. We applied a fixed 25 Hz high-pass FIR filter in (A) and (B) and a 150 Hz high-pass FIR filter in (C) and (D). While surface vessels and bone artifacts can be seen in the 25 Hz FIR-filtered and the HOSVD images of Fig. 3.10, only HOSVD images show slow flow within interior vessels of the ischemic hindlimb and uniformly perfused muscle in proximal regions of healthy controls. Sensitivity is reduced in distal muscle regions of all images as sound attenuation reduces SNCR.

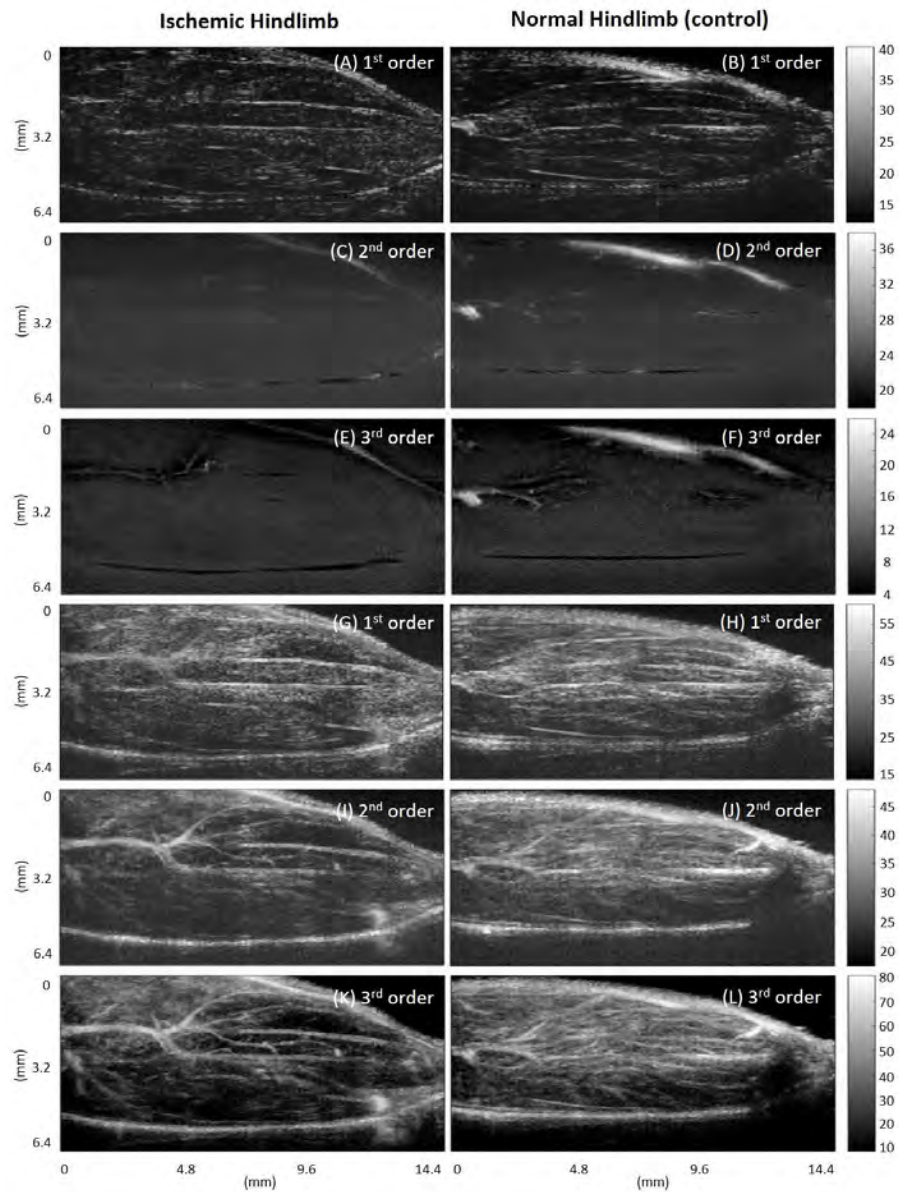


Figure 3.9: Comparisons of the visually clearest examples of first-, second-, and third-order filters applied to the slow-time data axis (A-F) to display arterial flow and to the frame-time data axis (G-L) to display perfusion. Each image is based on same 17 frames of echo data.

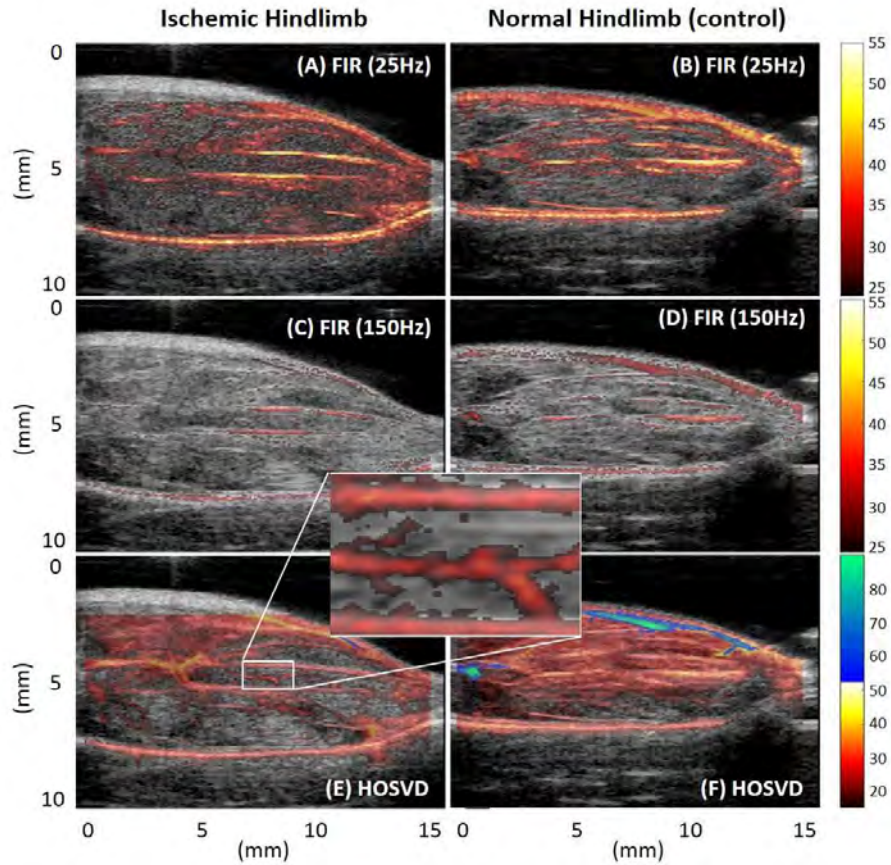


Figure 3.10: PD images are compared using standard FIR clutter filtering (first row: 25 Hz high-pass, second row: 150 Hz high-pass) and adaptive HOSVD filtering (third row) applied to the same data array. Notice that perfusion in the control limb is fairly uniform, except in distal regions where the SNCR is low. Conversely, the ischemic limb shows patchy perfusion throughout. The inset shows an enlargement of microvessels. Given that the PD pixel dimensions are  $32 \mu\text{m}$  axially and  $60 \mu\text{m}$  laterally, we are resolving  $160 \mu\text{m}$ -dia vessels axially and  $300 \mu\text{m}$ -dia vessels laterally. Axial resolution for 24 MHz pulses with 12 MHz bandwidth is  $\sim 128 \mu\text{m}$ . The blue and red colorbars indicate, respectively, color maps related to slow-time power (dB) and frame-time power (dB).

### 3.4 Discussion

These preliminary data suggest the proposed changes in acquisition and filtering can greatly increase the sensitivity of ultrasonic power-Doppler perfusion imaging without contrast enhancement. The HOSVD filter allows us to separate fast and slow flows that we indicate with blue and red color maps in Fig. 3.10 (arrows in top row of Fig. 3.11 also indicate arterial flows). We were fortunate to capture a portion of the femoral artery in the ischemic image. This ligated vessel appears prominently in the perfusion image because it is weakly fed from collateral vessels. Also, at 24 MHz, the ischemic hindlimb perfusion image inset in Fig. 3.10 (E) clearly displays vessels with diameter smaller than  $200 \mu\text{m}$ . These small vessels are less visible in the control hindlimb (F) where surrounding capillary perfusion reduces small-vessel contrast (not shown).

Baseline perfusion, which is 17 ml/min/100g in the normal hindlimb [51], falls to 60-70% of that value following femoral ligation [50]. Consequently, a 5-10 g hindlimb muscle has normal capillary flow in the range of 1-3 ml/min. A key element of successful HOSVD filtering is selection of the clutter and blood subspaces within core tensor,  $\mathcal{G}$ . The standard selection method is based on eigenvalue information and echogenic properties of the sources as mentioned in Section 3.2.3. Since there are only a few prominent elements in  $\mathcal{G}$ , we now just try various filter ranges and inspect the resulting PD images to determine the “best” filter parameters. The following techniques using eigenvector information could guide a more objective and automated partitioning of  $\mathcal{G}$ .

The top left PD image in Fig. 3.11 represents a different normal mouse hindlimb. Here we see two segments of arterial flow as indicated by arrows and the blue-green color. On the right, we reproduce the ischemic hindlimb image from Fig. 3.10 that displays no fast blood flow patterns. In both images, we box a region of interest that includes directed vascular flows away from the transducer; on the left, flow velocity is in the range 2-15 mm/s and on the right the flow velocity is in the range  $\pm 0.2$  mm/s.

In the second row of Fig. 3.11, we display the first nine odd spatial eigenvectors as gray scale images. These are taken from data in the boxed regions in the figures above. The absolute values of elements in each spatial eigenvector are reshaped back into the shapes of the 2-D image patches. Looking closely,

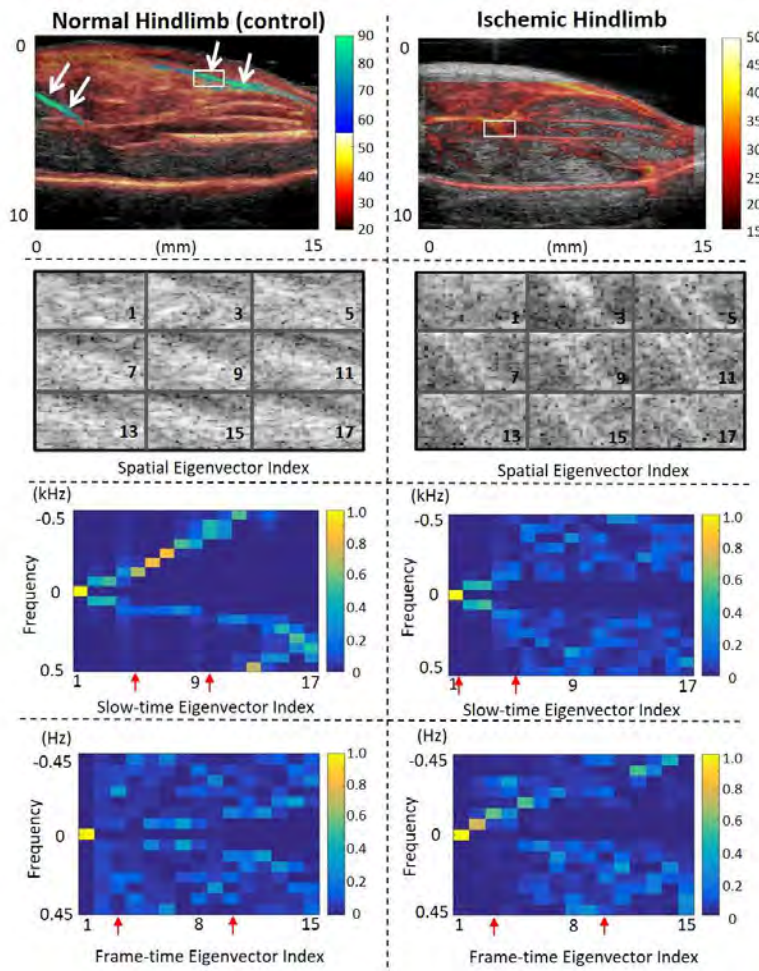


Figure 3.11: The two columns illustrate analyses of data within local regions of three images. Top row shows adaptive HOSVD images of normal and ischemic hindlimbs. White arrows indicate arterial flows, and boxes indicate analysis regions that include a vessel. The second row shows 9 of the first 18 spatial eigenvectors, some showing linear shapes similar to vessels seen in top row images. Third and fourth rows depict the power spectrum of slow-time and frame-time eigenvectors, respectively. The vertical axis is temporal frequency with the origin at the center, and the horizontal axis indicates eigenvectors along the corresponding axes, of which there are 17. Each column of the four spectral images is the absolute-square Fourier transform of the corresponding eigenvector. Eigenvectors between the red arrows were passed by the HOSVD filter for the images displayed in this report. Eigenvectors outside these ranges were removed by the filter.

we see the linear shape of the vessel within each eigenvector that is similar to that in the boxed image region above, except for the first eigenvector. The uniformity of spatial eigenvector 1 suggests it is dominated by clutter, while the appearance of a vessel-like structure in the other eigenvectors suggests they are influenced by directional blood flow in the vessel. For this reason, we eliminate at least the first spatial eigenmode through HOSVD filtering.

Images of the slow-time eigenvector spectra (third row in Fig. 3.11) and frame-time eigenvector spectra (fourth row) further reveal information about blood flow. In the first eigenvector spectrum (left-most column of the spectral images) the only nonzero value is at zero-frequency; consequently the first eigenvector offers no information about movement and should be discarded. The linear spectral pattern in the normal hindlimb slow-time spectral image between eigenvectors 5-10 (third row, left in Fig. 3.11) suggests a strong signal is present for fast directed blood flow. Because this flow is away from the transducer, the linear pattern appears along the negative-frequency axis, which shows there is directional flow information available. Notice the spectrum shows evidence of aliasing as the linear structure wraps from negative to positive frequencies at eigenvector 13. There is no linear spectral pattern for the normal hindlimb image in the corresponding frame-time spectrum (fourth row, left in Fig. 3.11) as expected for the slow, disorganized RBC movement associated with capillary perfusion. The red arrows along the abscissa indicate the upper and lower bounds on the eigenvector pass band set for HOSVD filtering.

There is also an asymmetric linear spectral pattern in the ischemic hindlimb image between eigenvectors 3-9 in the frame-time spectrum (fourth row, right in Fig. 3.11). This corresponds to the relatively slow but downward-directed flow within the large vessel in the ischemic tissue. We know it is slow flow because it is found in the frame-time spectrum and the linear pattern indicates the flow is directed. Conversely, the slow-time eigenvector spectrum for the ischemic leg (third row, right in Fig. 3.11) is symmetric and diffuse, indicating no directed fast flow in this region.

Future work includes imaging at lower transmission frequencies and higher frame-time rates to assess clinical utility in human subjects. The low frame rate used for the murine model is unlikely to span the wider range of perfusion velocities found in human tissue.

## 3.5 Conclusion

In this preliminary study, we found that expanding the dimension of the acquired echo-data array and then strategically reducing the data dimension using adaptive HOSVD filters leads to images that suggest improved perfusion sensitivity. At this point in development, the method offers images of signal power that describe relative flow and perfusion patterns.

HOSVD filtering appears to enhance the distinct information provided by each axis of the 3-D data array, enabling visualization of blood components of the echo signal while effectively suppressing clutter and noise components. The addition of frame-time data as a separate array dimension appears to allow increased sensitivity to slower flows through a longer acquisition period without discarding fast blood flow echoes offered by the slow-time array axis. One 3-D acquisition processed via HOSVD effectively displays both blood components.

Although we apply power-Doppler processing here, we note that the eigenvector spectra seen in Fig. 3.11 contain information about the direction and spatial coherence of RBC movement. In principle, color-flow imaging is possible. We applied 24 MHz ultrasonic pulses to couple the method to the small mouse model which enabled sub-millimeter vessel diameter flows to be imaged with 5-mm tissue penetration.

The price paid for adding the frame-time axis in the echo-power estimator is that each PD frame requires more than 1 s worth of data acquisition. Since perfusion is normally steady or slowly varying, the long acquisition could be inconsequential depending on the application. The added sensitivity and lower noise justify the extra time and effort, especially when imaging stationary echo data that describe steady RBC movements, as for the application described in this chapter. Little effort has been made thus far to minimize the time required to compute one PD image frame, which now stands at 19.1 s.

# CHAPTER 4

## CLUTTER FILTER OPTIMIZATION

### 4.1 Introduction

Pulse-echo power Doppler (PD) imaging is highly sensitive to slow disorganized movements of red blood cells (RBCs), and therefore it is a natural choice for microvascular and perfusion imaging. PD signals are insensitive to blood speed and direction but highly vulnerable to tissue clutter and acquisition noise sources. The most effective PD methods for perfusion imaging without contrast enhancement are those that maximize the sensitivity of echo signals to RBC movements in ways that can be uncoupled from clutter and noise signal sources. This chapter explores a new approach to perfusion imaging with a focus on clutter filter design.

Detailed overviews of clutter filtering research are found from the literature, including [17, 18, 52]. Originally, Fourier-basis clutter filters were applied (e.g., FIR, IIR). The Doppler equation provided a direct interpretation between temporal Fourier coefficients and blood velocity. However, it is now well accepted that Fourier-basis filters do not provide the best separation between tissue and slow-moving blood echoes [20, 17, 53]. Eigenbases are a generalization of Fourier bases that can adapt to specific data sets and thus have the potential to provide more separability between the blood and tissue subspaces. Eigenfilters result from a decomposition of the echo-data temporal correlation matrix. In contrast, SVD-basis filters are able to fully exploit the spatiotemporal nature of each echo acquisition [54, 25, 28]. 2D SVD generates both temporal and spatial bases, so that the characteristically strong echoes of spatially coherent tissue movements can be more readily separated from the weaker echoes of spatially incoherent blood perfusion echoes. Recently, high frame-rate acquisition techniques have been coupled to 2-D SVD clutter filters to provide exciting new opportunities for microvascular

imaging in brain, kidney and thyroid tissues [28, 52].

In Chapter 3, we found that probing tissues with multicycle bursts of Doppler pulses over long durations can significantly increase the sensitivity of echo signals to peripheral perfusion RBC movement. RBC sensitivity increases if we reorder the time axis into two array dimensions, labeled slow-time and frame-time axes, to produce a 3-D echo-data array. 3-D data arrays are decomposed using higher-order SVD (HOSVD) techniques [42, 55, 43] to produce three orthogonal basis sets corresponding to slow-time, spatial, and frame-time vector spaces. We also found that enhanced perfusion signals could be uncoupled from clutter by decomposing the data array and locating the blood subspace within the 3-D core tensor elements. However, subsequent phantom studies reported below suggest the eigen-bandwidth for clutter plays a key role in clutter-blood subspace separability.

To identify the clutter eigen-bandwidth, we are proposing a statistical classifier applied to each core-tensor element. The classifier decides if a core element is predominantly from a clutter source based on a vector of five signal energy and similarity features estimated from the decomposition eigenvalues and eigenvectors. Encouraged by a similar approach described by Baranger et al. [52] for 2-D SVD filters, we arrive at different but consistent findings. Signal subspaces and clutter filter designs are explored through echo simulations, where all data properties are known exactly; phantom experiments, where data properties are known statistically; and *in vivo* experiments, where the data properties are most realistic.

## 4.2 Methods

### 4.2.1 Notation

To distinguish various types of data arrays, we adopt the following notation:

- Scalars are lower-case or capital letters  $a, b, N, M \dots$
- Column vectors are bold lower-case letters  $\mathbf{a}, \mathbf{b} \dots$
- Matrices are bold capital letters  $\mathbf{A}, \mathbf{B} \dots$

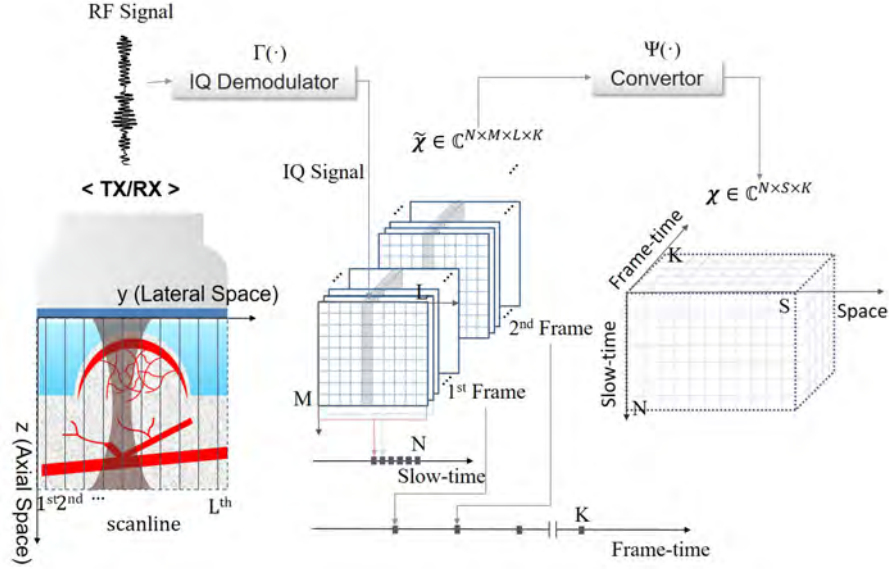


Figure 4.1: Color-flow acquisition is illustrated resulting in multidimensional data array  $\tilde{\mathcal{X}}$ . A linear array transmits sound pulses into tissue and receives echoes along a line of site. Signals from the receive aperture are beamformed, fast-time sampled, decomposed into baseband quadrature signals and stored as an  $M$ -point complex IQ vector.  $N$  transmissions in slow time at a  $\sim 1$  kHz pulse repetition frequency (PRF) are made for each of  $L$  lateral lines to compose one 3-D Doppler frame. Recording  $K$  frames at a  $\sim 10$  Hz frame repetition frequency (FRF) yields the 4-D data array  $\tilde{\mathcal{X}} \in \mathbb{C}^{N \times M \times L \times K}$ . The 4-D array is reordered to form 3-D array  $\mathcal{X} \in \mathbb{C}^{N \times S \times K}$ , where  $S = ML$ .

- Multidimensional arrays (tensors) are bold calligraphic capital letters  $\mathcal{A}, \mathcal{B}, \dots$
- Array elements: The  $i$ th element of vector  $\mathbf{a}$  is denoted  $a_i = \mathbf{a}[i]$ , the  $(i_1, i_2)$ th element of matrix  $\mathbf{A}$  is  $a_{i_1, i_2} = \mathbf{A}[i_1, i_2]$ , and the  $(i_1, i_2, i_3)$ th element of 3-D array (tensor [55])  $\mathcal{A}$  is  $a_{i_1, i_2, i_3} = \mathcal{A}[i_1, i_2, i_3] = \mathcal{A}_{i_1, i_2, i_3}$ .

Sets for integers, real numbers and complex numbers are represented as  $\mathbb{Z}$ ,  $\mathbb{R}$  and  $\mathbb{C}$ , respectively. For example,  $a \in \mathbb{Z}_{[0, N]}$  indicates  $a$  is an integer scalar and  $0 \leq a \leq N$ .

## 4.2.2 Echo-Signal Model

First, let us review the acquisition model. We define the spatiotemporal structure of the data array resulting from the narrow-band pulsed-Doppler

acquisition illustrated in Fig. 4.1. Each beamformed quadrature (IQ) echo waveform  $x(t)$  is sampled on the fast-time interval  $T$  as  $x(t_m)$  where  $t_m = mT$  and  $m \in \mathbb{Z}_{[1,M]}$ .  $M$  is the number of temporal samples recorded following each pulse transmission. Scaling the time axis, we form the axial waveform  $x(z_m) = x(z_0 + ct_m/2)$  where  $c$  is the sound speed and  $z_0$  is the distance between the transducer surface and the onset of the range gate. Repeatedly transmitting  $N$  pulses at each line of site on the slow-time interval  $T' > MT$  results in 2-D spatiotemporal echo signal  $x(t_n, z_m)$ , where  $t_n = nT'$  and  $n \in \mathbb{Z}_{[1,N]}$ . Indexing the transmit and receive apertures laterally on the interval  $D$  yields  $L$  echo lines within one Doppler frame. Each 3-D Doppler frame  $x(t_n, z_m, y_l)$  has a slow-time dimension and two spatial dimensions including  $y_l$  as the lateral position of the  $l$ th echo line;  $l \in \mathbb{Z}_{[1,L]}$ . Finally,  $K$  Doppler frames are recorded at frame-time interval  $T'' > T'$  to form the 4-D echo-data array

$$\tilde{\mathcal{X}} = x(t_n, z_m, y_l, t_k) \in \mathbb{C}^{N \times M \times L \times K}, \quad (4.1)$$

where  $t_k = kT''$  and  $k \in \mathbb{Z}_{[1,K]}$ .

Second, we describe a linear model for simulating Eq. (4.1). Echoes from perfused tissues are assumed to arise from discrete red blood cell (RBC) and surrounding tissue reflectors, the latter is referred to as tissue clutter. Discrete acquisition time  $t = t_{n,m,l,k}$  is the clock time passing during a complete 4-D acquisition. Scattering functions  $c_i(z, y, t)$  and  $b_j(z, y, t)$  define the  $i$ th discrete tissue reflector and the  $j$ th RBC, respectively, at spatiotemporal location  $(z, y, t)$ . Further, let  $h(z, y)$  be the spatially invariant pulse-echo impulse response of the ultrasonic instrument. Consequently, the echo-data array  $\tilde{\mathcal{X}}$  can be modeled as a 2-D spatial convolution,

$$\begin{aligned} \tilde{\mathcal{X}}_{n,m,l,k} = & \Gamma \left( \iint_{\Omega} dz dy h(z - (z_0 + cmT/2), y - y_l) \right. \\ & \left. \times \left[ \sum_{i=1}^{J_c} c_i(z, y, t_{n,m,l,k}) + \sum_{j=1}^{J_b} b_j(z, y, t_{n,m,l,k}) \right] \right) + e_{n,m,l,k}, \end{aligned} \quad (4.2)$$

where  $\Gamma(\cdot)$  is the operator that converts RF signals to in-phase and quadrature (IQ) components [45],  $\Omega$  is a 2-D region indicating the spatial extent of the acquisition, and  $J_c$  and  $J_b$  are the numbers of discrete tissue and blood

scatterers, respectively, in  $\Omega$ . Also  $e$  is additive white-Gaussian acquisition noise. Equation (4.2) is more simply expressed as the sum of three 4-D arrays describing clutter  $\tilde{\mathcal{C}}$ , blood  $\tilde{\mathcal{B}}$ , and noise  $\tilde{\mathcal{N}}$  sources via

$$\tilde{\mathcal{X}} = \tilde{\mathcal{C}} + \tilde{\mathcal{B}} + \tilde{\mathcal{N}}. \quad (4.3)$$

Ratios of signal power between contributing sources are

$$\begin{cases} r_{\text{CB}} = 10 \log_{10} (\|\tilde{\mathcal{C}}\|^2 / \|\tilde{\mathcal{B}}\|^2) \\ r_{\text{BN}} = 10 \log_{10} (\|\tilde{\mathcal{B}}\|^2 / \|\tilde{\mathcal{N}}\|^2), \end{cases} \quad (4.4)$$

where  $\|\cdot\|$  indicates the  $\ell_2$ -norm and  $r_{\text{CB}}$  and  $r_{\text{BN}}$  are clutter-to-blood and blood-to-noise ratios, respectively, each expressed in decibels.

### 4.2.3 Tissue and Blood Motion

The  $i$ th tissue scatterer randomly positioned in  $\Omega_c \in \Omega$  (see Fig. 4.2) is represented by the Dirac delta

$$c_i(z, y, t) = \alpha_c^{(i)} \delta \left( z - (z_{c0} + z_c(t))^{(i)}, y - (y_{c0} + y_c(t))^{(i)} \right), \quad (4.5)$$

where  $\alpha_c^{(i)} \sim N(m_{\alpha_c}, \sigma_{\alpha_c}^2)$  is a normally distributed echo amplitude assigned to the  $i$ th tissue scatterer, and  $(z_{c0}^{(i)}, y_{c0}^{(i)})$  is its position in  $\Omega_c$  at  $t = 0$ . Tissue displacement vector  $\mathbf{f}_c(t)$ , which applies at  $t > 0$ , describes the temporal movements of all tissue scatterers in  $\Omega$  relative to the initial positions. It includes the sum of 2-D breathing  $\boldsymbol{\eta}(t)$  and muscle vibration  $\boldsymbol{\xi}(t)$  vectors:

$$\begin{aligned} \mathbf{f}_c^{(i)}(t) &= (z_c(t), y_c(t))^{(i)} = \boldsymbol{\eta}(t) + \boldsymbol{\xi}(t) \quad \text{for } t > 0 \\ \text{and where } \begin{cases} \boldsymbol{\eta}(t) = \beta \left[ \sum_{n'} e^{\frac{-(t-n'\Delta t)^2}{2\sigma_r^2}}, 0 \right] \\ \boldsymbol{\xi}(t) = \gamma \sin(w_0 t) [\cos(\theta), \sin(\theta)]. \end{cases} \end{aligned} \quad (4.6)$$

Symbol  $n'$  is an integer,  $\Delta t$  indicates the interval between breaths, and  $\beta$  and  $\sigma_r$  specify the range and rate of breathing movement oriented along the  $z$  axis. Parameters  $\gamma$ ,  $w_0$  and  $\theta$  determine the oscillation strength, frequency and direction, of muscle vibration. The directions of the two sources of clutter movement are not aligned to each other nor are they synchronous, although each function is applied simultaneously to all scatterers in  $\Omega_c$ .

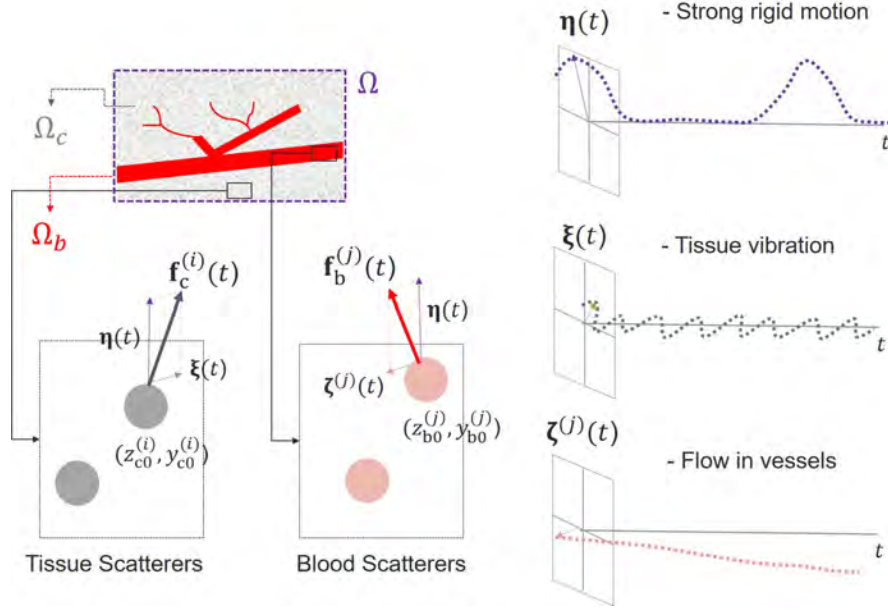


Figure 4.2: Simulation of tissue perfusion is illustrated. Scattering field  $\Omega$  consists of nonoverlapping regions of tissue scatterers in  $\Omega_c$  and moving RBCs in  $\Omega_b$ . On the top right, we show a time series for the entire field  $\Omega$  in which all scatterers (illustrated below left) undergo large-scale low-frequency periodic rigid motion mimicking respiration. In addition, scatterers in regions  $\Omega_c$  undergo rigid-body vibration at higher frequency and smaller amplitude, while vascular RBCs in regions  $\Omega_b$  undergo blunt-flow translation with known velocity.

Similarly, the position of the  $j$ th RBC is

$$b_j(z, y, t) = \alpha_b^{(j)} \delta \left( z - (z_{b0} + z_b(t))^{(j)}, y - (y_{b0} + y_b(t))^{(j)} \right), \quad (4.7)$$

where the RBC echo amplitude is  $\alpha_b^{(j)} \sim N(m_{\alpha_b}, \sigma_{\alpha_b}^2)$  and  $(z_{b0}^{(j)}, y_{b0}^{(j)})$  is the initial position within  $\Omega_b \in \Omega$ .

Blood displacement vector  $\mathbf{f}_b^{(j)}(t) = (z_b^{(j)}(t), y_b^{(j)}(t))$  describes temporal movement of the  $j$ th RBC at times  $t > 0$  relative to its initial position. RBC movement is also modeled as the sum of two 2-D vector sources,

$$\begin{aligned} \mathbf{f}_b^{(j)}(t) &= \boldsymbol{\eta}(t) + \boldsymbol{\zeta}^{(j)}(t) \quad \text{for } t > 0 & (4.8) \\ \text{where } \boldsymbol{\zeta}^{(j)}(t) &= t[v_z^{(j)} \sin \varphi^{(j)}, v_y^{(j)} \cos \varphi^{(j)}]. \end{aligned}$$

The components of velocity  $v_z^{(j)}, v_y^{(j)}$  and the Doppler angle  $\varphi^{(j)}$  are constant in time but vary spatially within  $\Omega$  as illustrated, for example, by the vascular patterns in Fig. 4.2. Since respiration is a rigid-body translation of vessels



transformation operator  $\Psi$ , resulting in

$$\mathbf{x} = \Psi(\tilde{\mathbf{x}}), \text{ such that } x_{n,s,k} = \tilde{x}_{n,m,l,k}, \quad (4.9)$$

where  $\mathbf{x} \in \mathbb{C}^{N \times S \times K}$ ,  $s = m + (l - 1)M$  and  $S = ML$ . In Chapter 3, we showed how to decompose  $\mathbf{x}$  using higher-order singular-value decomposition (HOSVD). Reducing the data array from 4D to 3D speeds the HOSVD compute time.

HOSVD is a multilinear generalization of 2-D SVD analysis [42, 43]. As illustrated in Fig. 4.3, decomposing  $\mathbf{x}$  generates core tensor<sup>1</sup>  $\mathcal{G} \in \mathbb{C}^{N \times S \times K}$  with core elements  $g_{i_1 i_2 i_3}$  and three orthogonal matrices:  $\mathbf{U} \in \mathbb{C}^{N \times N}$  whose columns  $\mathbf{u}$  are slow-time-mode eigenvectors,  $\mathbf{V} \in \mathbb{C}^{S \times S}$  whose columns  $\mathbf{v}$  are spatial-mode eigenvectors, and  $\mathbf{W} \in \mathbb{C}^{K \times K}$  whose columns  $\mathbf{w}$  are frame-time-mode eigenvectors. The expression is

$$\begin{aligned} \mathbf{x} &= \mathcal{G} \times_1 \mathbf{U} \times_2 \mathbf{V} \times_3 \mathbf{W} \\ &= \sum_{i_1=1}^N \sum_{i_2=1}^S \sum_{i_3=1}^K g_{i_1, i_2, i_3} \mathbf{u}_{i_1} \times \mathbf{v}_{i_2} \times \mathbf{w}_{i_3}, \end{aligned} \quad (4.10)$$

where  $\times_n$  denotes  $n$ -mode outer product as defined in [42, 43]. The eigenvalues for each of the three modes are given by

$$\begin{cases} \text{Slow-time mode:} & \lambda_{j_1}^{(1)} = \sum_{i_2=1}^S \sum_{i_3=1}^K |g_{j_1, i_2, i_3}|^2 \\ \text{Spatial mode:} & \lambda_{j_2}^{(2)} = \sum_{i_1=1}^N \sum_{i_3=1}^K |g_{i_1, j_2, i_3}|^2 \\ \text{Frame-time mode:} & \lambda_{j_3}^{(3)} = \sum_{i_1=1}^N \sum_{i_2=1}^S |g_{i_1, i_2, j_3}|^2 \end{cases} \quad (4.11)$$

Eigenvalues for each mode are arranged in decreasing order.

Our main interest is to preserve echo signals originating from blood perfusion while suppressing other echo-signal contributions. We can filter the echo data by identifying the 3-D subspace in  $\mathcal{G}$  dominated by perfusion echoes and suppressing values outside the perfusion subspace. Since signal power from clutter, blood, and acquisition-noise sources can occupy the same subspace, the filtering process is not straightforward.

---

<sup>1</sup>Modal planes in  $\mathcal{G}$  are orthogonal; i.e.,  $\sum_{i_1} \sum_{i_2} g_{i_1, i_2, a} g_{i_1, i_2, b} = \sum_{i_1} \sum_{i_3} g_{i_1, a, i_3} g_{i_1, b, i_3} = \sum_{i_2} \sum_{i_3} g_{a, i_2, i_3} g_{b, i_2, i_3} = 0$  unless  $a = b$ .

## 4.2.5 Clutter Filtering

The strategy is to classify each core element  $(i_1, i_2, i_3)$  as clutter or non-clutter based on five features described below. Elements identified as “clutter dominant” are discarded.

### Feature Selection

- Normalized Eigenvalues: Three of the five features are from the normalized eigenvalue spectra. The slow-time eigenvalue spectrum is normalized using

$$\bar{\lambda}_{i_1}^{(1)} = \frac{\log_{10} \lambda_{i_1}^{(1)} - \log_{10} \lambda_{min}^{(1)}}{\log_{10} \lambda_{max}^{(1)} - \log_{10} \lambda_{min}^{(1)}} \in \mathbb{R}_{[0,1]}, \quad (4.12)$$

where  $\lambda_{max}^{(1)} = \lambda_1^{(1)}$  and  $\lambda_{min}^{(1)} = \lambda_N^{(1)}$ . Similarly, the normalized spatial and frame-time eigenvalue spectra are  $\bar{\lambda}_{i_2}^{(2)}$  and  $\bar{\lambda}_{i_3}^{(3)}$ , respectively. In each normalized spectrum, the first value is largest and equal to 1. When clutter is significant, subsequent spectral values at  $i_1, i_2, i_3 > 1$  associated with clutter remain close to 1 (Fig. 4.4, top right). Large eigenvalues arise from the most echogenic components of  $\tilde{\mathcal{X}}$  that are typically associated with stationary or rigid-body tissues dynamics.

- Tissue Structure Similarity: The magnitude of each spatial eigenvector,  $\mathbf{s}_{i_2} = |\mathbf{v}_{i_2}| \in R^{S \times 1}$ , which are columns of  $\mathbf{V}$ , can be reformatted into a 2-D image  $\mathbf{S}_{i_2} \in R^{M \times L}$ . Eigenimage  $\mathbf{S}_1$  is associated with the largest (first) eigenvalue. It resembles the B-mode image for the region of interest. Other eigenimages from  $\mathbf{V}$  that are influenced by tissue clutter will have similar structural patterns. In contrast, eigenimages most influenced by blood signals or noise will appear dissimilar to  $\mathbf{S}_1$ . The fourth feature,  $d$ , compares the first eigenimage with each of the others using Pearson’s correlation coefficient via operator  $\Upsilon(\cdot)$  to quantify similarity.

$$\begin{aligned} d_{i_2} &= \Upsilon(\mathbf{s}_1, \mathbf{s}_{i_2}) \\ &= \frac{\sum_{n=1}^S (\mathbf{s}_1[n] - \bar{s}_1)(\mathbf{s}_{i_2}[n] - \bar{s}_{i_2})}{\sqrt{\sum_{n=1}^S (\mathbf{s}_1[n] - \bar{s}_1)^2} \sqrt{\sum_{n=1}^S (\mathbf{s}_{i_2}[n] - \bar{s}_{i_2})^2}}, \end{aligned} \quad (4.13)$$

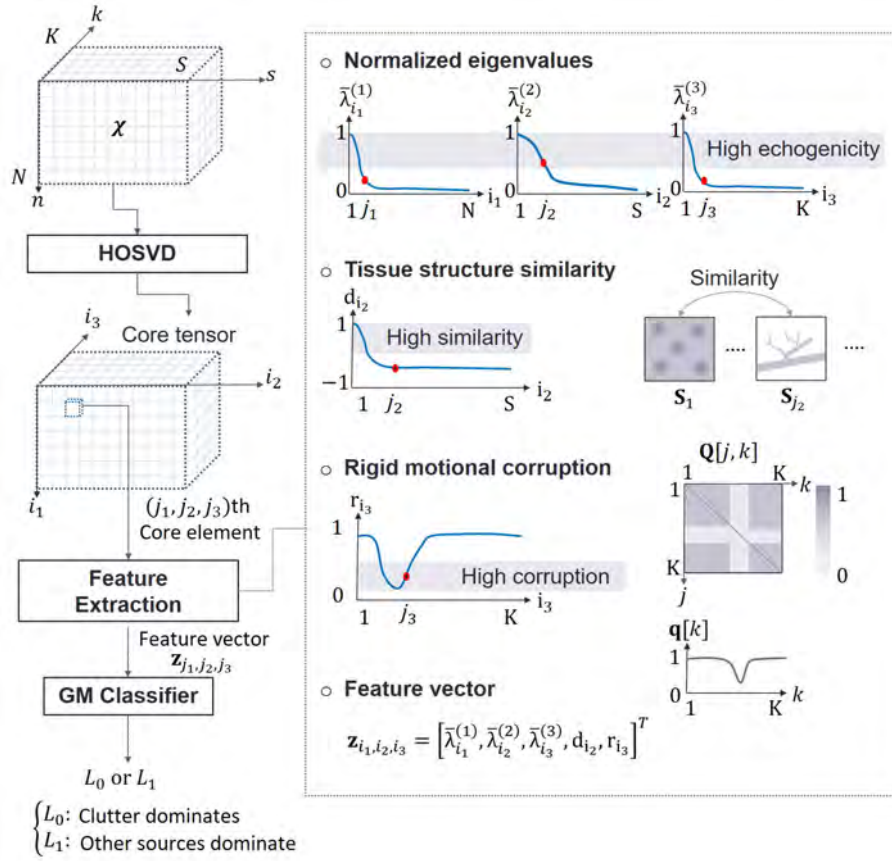


Figure 4.4: The diagram describes a classification of each eigenelement for clutter filtering. To determine the state of  $(j_1, j_2, j_3)$ th core element, features are extracted from eigenvectors and eigenvalues. Normalized eigenvalues are associated with source echogenicity. The eigenimage using spatial eigenvector provides structural information as we will show in Fig. 4.6. Provided that 1st eigenimage  $\mathbf{S}_1$  most likely involves tissue structure, the correlation between the 1st image and  $j_2$ th image informs contribution of the  $j_2$ th eigenspace for tissue clutter. The last feature is associated with strong rigid motion. Data acquired for the moment tend to be corrupted by strong clutter. The time points can be recognized by similarity matrix  $\mathbf{Q}$  obtained by computing correlation between frame-images. The feature measures the contribution of the  $j_3$ th eigenspace for the time-points (corruption). The Gaussian mixture (GM) classifier makes a decision using the features.

where  $d_{i_2} \in \mathbb{R}_{[-1,1]}$ , and  $\bar{s}_1, \bar{s}_{i_2}$  are the means of all samples in vectors  $\mathbf{s}_1, \mathbf{s}_{i_2}$ . Large positive  $d$  values indicate core elements with significant clutter contributions to  $\mathcal{X}$ . (see Fig. 4.4, right.)

- Rigid-body Motion Corruption: Adding a frame axis to extend the echo-data array enhances sensitivity to both blood perfusion and moving tissue clutter. The magnitude of motion over the frame-time axis is identified by comparing echo power images obtained by the  $k$ th Doppler frame using

$$\mathbf{P}_k[m, \ell] = 10 \log_{10} \left( \frac{1}{N} \sum_{n=1}^N |\tilde{\mathcal{X}}[n, m, \ell, k]|^2 \right). \quad (4.14)$$

The similarity between echo power in two frames is

$$\mathbf{Q}[j, k] = \Upsilon(\mathbf{P}_j, \mathbf{P}_k), \quad (4.15)$$

where matrix  $\mathbf{Q} \in \mathbb{R}^{K \times K}$ . The sudden, large-amplitude, coherent motion characteristic of clutter creates distinct patterns in  $\mathbf{Q}$  (see Fig. 4.4, right) where echo power is far less correlated. Negative correlations are possible, but, in practice, correlations from rigid-body motion remain positive. The mean correlation between the  $k$ th and  $j$ th frames is

$$\mathbf{q}[k] = \frac{1}{K} \sum_{j=1}^K \mathbf{Q}[j, k] \in \mathbb{R}_{[0,1]}. \quad (4.16)$$

Large coherent displacements, like those from breathing, result in small correlation values. Vector  $\mathbf{q}$  can thus be used as a basis to test if a frame is corrupted by clutter motion. The inner product

$$r_{i_3} = \sum_{k=1}^K \mathbf{q}[k] |\mathbf{w}_{i_3}[k]|^2 \in \mathbb{R}_{[0,1]} \quad (4.17)$$

provides  $r$ , a scalar feature quantifying motion corruption in a data frame. Note that  $|\mathbf{w}_{i_3}[k]|^2$  results from a Hadamard (element-wise) product of  $\mathbf{w}_{i_3}$  with itself. Small values of  $r$  indicate a frame is corrupted by coherent motion.

Each core tensor element is classified based on feature vector  $\mathbf{z}$  computed

for that element; from Eqs. (4.12),(4.13),(4.17),

$$\mathbf{z}_{i_1,i_2,i_3} = [\bar{\lambda}_{i_1}^{(1)}, \bar{\lambda}_{i_2}^{(2)}, \bar{\lambda}_{i_3}^{(3)}, d_{i_2}, r_{i_3}]^T. \quad (4.18)$$

### GM Classifier

Each core element was classified as clutter dominated  $L_0$  or non-clutter dominated  $L_1$  using the following likelihood ratio test classifier:

$$D(\mathbf{z}) = \begin{cases} L_0, & \text{if } p(\mathbf{z}|L_0)/p(\mathbf{z}|L_1) > \tau \\ L_1, & \text{if } p(\mathbf{z}|L_0)/p(\mathbf{z}|L_1) \leq \tau. \end{cases} \quad (4.19)$$

Threshold  $\tau$  depends on error risks [38].  $p(\mathbf{z}|L_0)$  and  $p(\mathbf{z}|L_1)$  are probability density functions (pdfs) conditioned on states  $L_0$  and  $L_1$ , viz.,  $p(\mathbf{z}|L_i) \sim \text{Normal}(\bar{\mathbf{z}}_i, \mathbf{\Sigma}_i)$ ,  $i \in \{0, 1\}$ . We will show that both pdfs are found by applying training data.

From simulated echo data with known states, likelihood functions are modeled as linear mixtures of three multivariate Gaussian functions (GM models):

$$p(\mathbf{z}|L_i) = \sum_{j=1}^3 A_{ij} \frac{1}{\sqrt{(2\pi)^3 |\mathbf{\Sigma}_{ij}|}} e^{(-\frac{1}{2}(\mathbf{z}-\bar{\mathbf{z}}_{ij})^\dagger \mathbf{\Sigma}_{ij}^{-1}(\mathbf{z}-\bar{\mathbf{z}}_{ij}))}, \quad (4.20)$$

where  $\mathbf{z}^\dagger$  is the conjugate transpose of  $\mathbf{z}$ . Amplitudes  $A_{ij}$ , mean vectors  $\bar{\mathbf{z}}_{ij}$ , and covariance matrices  $\mathbf{\Sigma}_{ij}$  are for the  $i$ th state and the  $j$ th (of three) mixture model functions. A three-component mixture model was found to provide acceptable model accuracy and reasonable computational time.

### Training

Simulated echo signals are computed from training media similar to the perfused tissue regions illustrated in Figs. 4.1 and 4.2. First, we set the blood and noise terms to zero in Eq. (4.2) to compute the clutter-only component,  $\tilde{\mathcal{C}} \in \mathbb{C}^{N \times M \times L \times K}$ , and reformat the result via Eq. (4.9) to find  $\mathcal{C} \in \mathbb{C}^{N \times S \times K}$ . Next, Eq. (4.2) is applied to the same model, now including all scattering components, to simulate perfusion data  $\tilde{\mathcal{X}}$  with clutter and noise. The 4-D array is reformatted to find  $\mathcal{X} \in \mathbb{C}^{N \times S \times K}$  and decomposed with HOSVD to compute core tensor  $\mathcal{G} \in \mathbb{C}^{N \times S \times K}$ . Rectangular subspaces within  $\mathcal{G}$  of

increasing size, beginning with element  $i_1 = i_2 = i_3 = 1$  and growing to  $i_1 = N, i_2 = S, i_3 = K$ , are progressively selected to form all possible estimates of clutter subspace  $\hat{\mathcal{G}}_C$ . Core elements outside the selected regions are set to zero. Reconstructing the echo data matrix from Eq. (4.10), but using  $\hat{\mathcal{G}}_C$  in place of  $\mathcal{G}$ , we estimate the clutter-only signal,  $\hat{\mathcal{C}}$ . Subspace  $\hat{\mathcal{G}}_C$  giving clutter echo-signal estimate  $\hat{\mathcal{C}}$  that most closely matches the known clutter-only signal  $\mathcal{C}$  becomes the final subspace estimate,  $\mathcal{G}_C$ . The objective function is

$$\mathcal{G}_C = \arg \min_{\hat{\mathcal{G}}_C} \|\mathcal{C} - \hat{\mathcal{C}}\|^2$$

$$w.r.t \left\{ \begin{array}{l} \hat{\mathcal{C}} = \sum_{(i_1, i_2, i_3) \in \hat{\mathcal{G}}_C} g_{i_1, i_2, i_3} \mathbf{u}_{i_1} \times \mathbf{v}_{i_2} \times \mathbf{w}_{i_3} \\ \hat{\mathcal{G}}_C = \{ \forall (i_1, i_2, i_3) | 0 < i_1 < c_{i_1}, \\ \quad \quad \quad 0 < i_2 < c_{i_2}, 0 < i_3 < c_{i_3} \} . \end{array} \right. \quad (4.21)$$

The feature vectors for core elements within  $\mathcal{G}_C$  are labeled  $L_0$ ; others are labeled  $L_1$ . Training results in a hard threshold being set for subspace parsing.

## Testing

With knowledge of the clutter subspace from Eq. (4.21), we can estimate the parameters in Eq. (4.20). Specifically, equivalent Matlab R2016a functions `gmdistribution.fit` or `fitgmdist` apply the expectation-maximization (EM) algorithm to find maximum-likelihood estimates of the three-component Gaussian mixture model parameters,  $A_{ij}$ ,  $\bar{\mathbf{z}}_{ij}$ , and  $\Sigma_{ij}$ . Finally, combining Eqs. (4.20) and (4.19), we are now prepared to simulate test data (independent of the training data) to test this clutter filter. First, we discuss a method for filtering acquisition noise.

### 4.2.6 Noise Filtering

Several techniques for suppressing additive white-Gaussian noise in a data array have been thoroughly studied [56, 57, 58]. Following clutter filtering, the noise-filtering approach we adopt is to find the blood-signal rank for the correlation matrix of each data-array mode,  $r_i$ , and to zero eigenvalues beyond  $r_i$ . In a tensor model, the blood-signal rank can be different for

the slow-time, spatial, and frame-time correlation matrices. We adopt a minimum description length (MDL) method for estimating the blood-signal rank of each matrix [58]. For example, the rank of the slow-time correlation matrix is estimated as

$$r_1 = \arg \min_r -2 \log \left\{ \frac{\prod_{i=r+1}^N [\lambda_i^{(1)}]^{1/(M-r)}}{\frac{1}{M-r} \sum_{i=r+1}^M \lambda_i^{(1)}} \right\}^{SK(M-r)} + r(2M - r) \log(SK). \quad (4.22)$$

Similarly, we estimate  $r_2$  and  $r_3$ . Data are noise filtered by discarding the noise-dominated subspace using the hard threshold  $\mathcal{G}_N = \{i_1, i_2, i_3 | (i_1 > r_1) \vee (i_2 > r_2) \vee (i_3 > r_3)\}$  where  $\vee$  indicates logical ‘or’. What remains is the blood subspace  $\mathcal{G}_B$ .

#### 4.2.7 Velocity Discrimination

We found that the slow-time eigenvector can be used to parse speed ranges for blood components of the post-filtered echo signal. The frequency spectrum of each slow-time eigenvector is found using the DFT expression

$$U[k] = \left| \frac{1}{N} \sum_{n=1}^N u_{i_1}[n] \exp(-i2\pi nk/N) \right|, \quad (4.23)$$

where  $u_{i_1}[n]$  is an  $n$ th element of eigenvector  $\mathbf{u}_{i_1}$ . Slow-time frequency  $f = k/NT'$  is converted into the axial component of blood speed  $v$  using the Doppler equation  $v = cf/2f_c$ , where  $c$  and  $f_c$  are the wave speed and pulse center frequency. The weight indicating contributions to the eigenvector from speed range  $[v_{min}, v_{max}]$  is found from

$$\omega_{i_1} = \sum_k U[k] w[k], \quad w[k] = \begin{cases} 1 & \text{if } v_{min} < \left| \frac{cf}{2f_c} \right| < v_{max} \\ 0 & \text{otherwise.} \end{cases} \quad (4.24)$$

The weight is used to apply a soft-threshold in the slow-time mode.

Velocity discrimination combined with clutter and noise suppression yields an estimate of the target blood-echo signal

$$\hat{\mathcal{B}} = \sum_{(i_1, i_2, i_3) \in \mathcal{G}_B} g_{i_1, i_2, i_3} (\omega_{i_1} \mathbf{u}_{i_1}) \times \mathbf{v}_{i_2} \times \mathbf{w}_{i_3}. \quad (4.25)$$

### 4.2.8 Filter Scale

Echo frames up to several  $\text{cm}^2$  in area are recorded for as long as 10 s to capture blood perfusion patterns. However, the heterogeneous space-time properties of tissue suggest that one filter cannot be expected to apply to all data in an acquisition. Instead we divide data arrays into statistically homogeneous blocks that may overlap, and we develop filters for each.

The  $j$ th of  $J$  data blocks is expressed as  $\tilde{\mathbf{x}}_j \in \mathbb{C}^{\dot{N} \times \dot{M} \times \dot{L} \times \dot{K}}$ , where  $\dot{N} < N$ ,  $\dot{M} < M$ ,  $\dot{L} < L$  and  $\dot{K} < K$ . Each block is reshaped into  $\mathbf{x}_j \in \mathbb{C}^{\dot{N} \times \dot{S} \times \dot{K}}$ , where  $\dot{S} = \dot{M}\dot{L}$ , and individually processed via HOSVD. The subspace selection for the  $j$ th filter is determined only by the statistical characteristics of data in that block.

## 4.3 Results

### 4.3.1 Simulation

A primary purpose for including simulation data is to explore the clutter-filter GM classifier described in Section 4.2.5. The classifier was trained and tested using simulation data and then applied in the phantom and *in vivo* tumor studies shown below. Figure 4.5 (A) illustrates 6 of 12 heterogeneous regions  $\Omega$  from which echo data are simulated for classifier training. The size of each field is  $1 \text{ mm} \times 1 \text{ mm}$  and vessel diameters range between 10 and  $100 \mu\text{m}$ . The center frequency of pulse transmissions is either 10 or 15 MHz. Point scatterers are initially uniformly distributed in tissue regions  $\Omega_c$  and vascular regions  $\Omega_b$ . Tissue regions are further divided into  $\Omega_{c_1}$  and  $\Omega_{c_2}$  with different echogenicity. Displacements of all scatterers over time follow the tissue and blood motion functions described in Section 4.2.3. Included in the 12 training fields, clutter-to-blood ratios were varied over the range  $15 \text{ dB} < r_{\text{CB}} < 40 \text{ dB}$  and the blood-to-noise ratios over the range  $5 \text{ dB} < r_{\text{BN}} < 30 \text{ dB}$  via Eq. (4.4). For training, 1800 data arrays were produced from the 12 regions and multiple combinations of parameters. All modeling and analysis parameters are summarized in Tables 4.1 and 4.2.

Training and testing data are simulated using identical parameters, although the data sets are statistically independent from each other. Figure 4.5

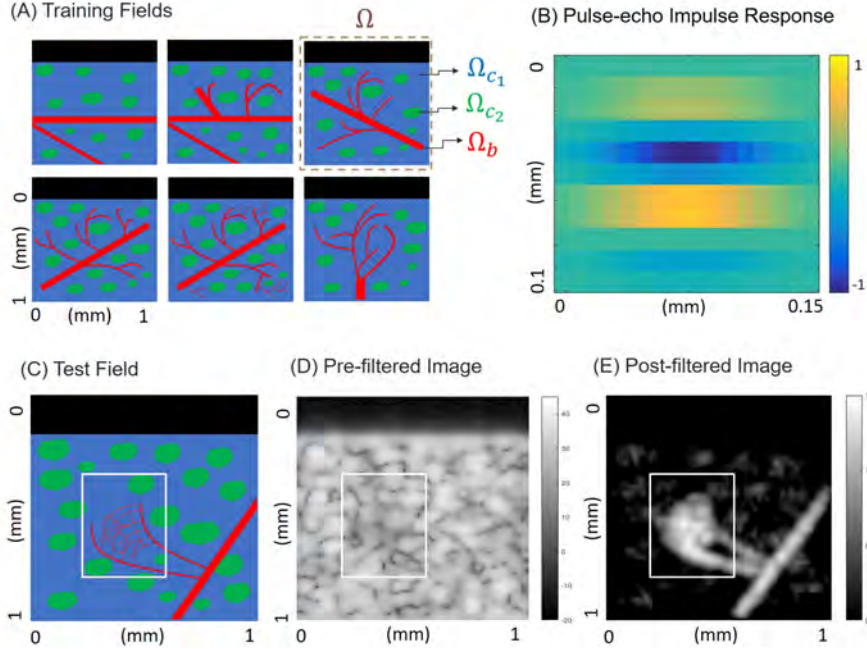


Figure 4.5: Examples of training and testing fields that were used to develop a clutter-filter classifier are shown with echo simulations. (A) Each of the 6 fields shown is composed of tissue  $\Omega_{c_1}$ ,  $\Omega_{c_2}$  and vascular  $\Omega_b$  regions. A 15 MHz pulse-echo impulse response is illustrated in (B). For the test field in (C), the pre- and post-filtered power Doppler (PD) images are shown in (D) and (E) for 15 MHz pulses. White boxes indicate regions containing fine vascular structures.

(C) displays one of the testing fields. Array data are processed for HOSVD clutter filtering then noise filtering. Figure 4.5 (D) and (E) show that vascular structures are clearly visualized in the post-filtered power-Doppler (PD) map but not in the pre-filtered PD map. The 50  $\mu\text{m}$  vessels are not resolved at 15 MHz.

Figure 4.6 provides examples from echo simulations of classification feature vector  $\mathbf{z}$  components. Figure 4.6 (A) shows significant overlap between blood and clutter components, except for the largest eigenvalues where clutter dominates. Figure 4.6 (B) displays the first three and middle three eigenimages,  $\{\mathbf{S}_{i_2} | i_2 = 1, 2, 3, 21, 22, 23\}$ . The first three eigenimages show tissue-related speckle because their eigenvectors are mostly influenced by tissue scattering (clutter). In contrast, vessel-like patterns found in the object of Fig. 4.5 (C) appear in eigenimages 21-23, showing how those eigenvalues are dominated by vascular flow. Finally, the dip in frame-time correlation in Fig. 4.6 (D)

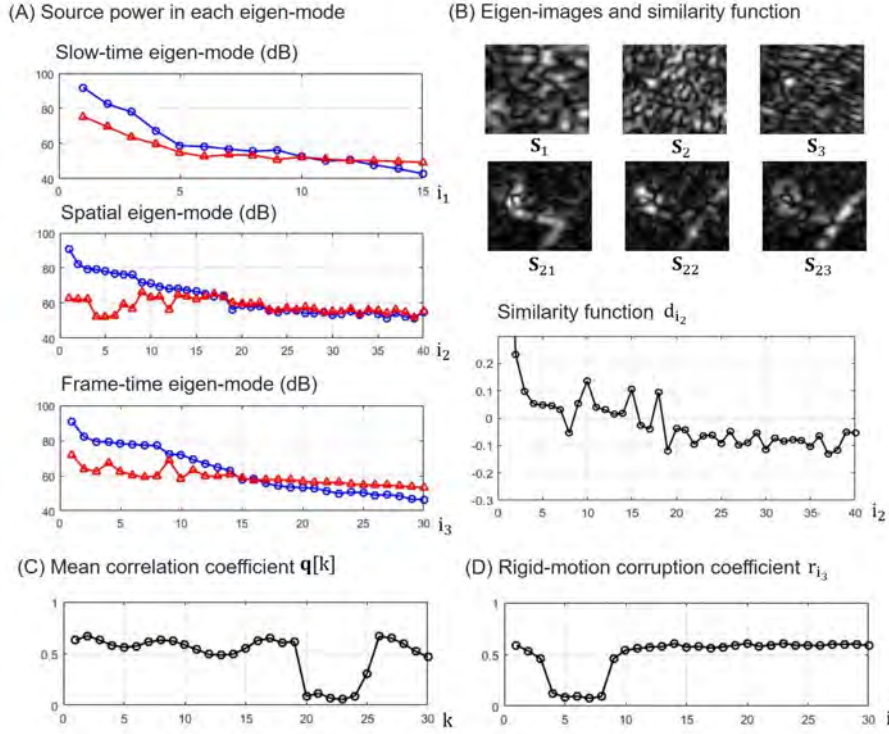


Figure 4.6: Measured components of feature vector  $\mathbf{z}$  analogous to those diagrammed in Fig. 4.4. These measurements are from echo simulations based on the test field of Fig. 4.5(C). (A) Contribution of the eigenvalues for clutter ( $\circ$ ) and blood ( $\triangle$ ) signals (Eq. (4.12)) are shown. Only the first 40 components of the spatial eigenmode are shown. (B) Six eigenimages  $\mathbf{S}_1, \mathbf{S}_2, \mathbf{S}_3, \mathbf{S}_{21}, \mathbf{S}_{22}$  and  $\mathbf{S}_{23}$ , and the similarity measures  $d_{i_2}$  (Eq. (4.13)). (C) Mean correlation coefficients  $\mathbf{q}[k]$  between the  $k$ th frame and others (Eq. (4.16)) are plotted. (D) Also shown is the contribution of the  $i_3$ th frame-time eigenvector ( $\mathbf{w}_{i_3}$ ) to the rigid-motion corruption coefficient  $r_{i_3}$  (Eq. (4.17)).

Table 4.1: Echo Data Simulation Parameters

Category/Function	Parameter	Value/Range
Tissue scatterers $c_i(\cdot)$ in field $\Omega_{c_1}$	Numbers $J_{c_1}$	4000
	Echo amplitude mean $\bar{\alpha}_{c_1}$	15
	Echo amplitude STD	1
Tissue scatterers $c_i(\cdot)$ in field $\Omega_{c_2}$	Numbers $J_{c_2}$	1200
	Echo amplitude mean $\bar{\alpha}_{c_2}$	25
	Echo amplitude STD	1
Blood scatterers $b_i(\cdot)$ in field $\Omega_b$	Numbers $J_b$	1000
	Echo amplitude mean $\bar{\alpha}_b$	1,2,3,4
	Echo amplitude STD	1
Source power ratio	Clutter-to-blood $r_{CB}$	15-40 dB
	Blood-to-noise $r_{BN}$	5-30 dB
Rigid-body motion ( $\boldsymbol{\eta}(t)$ )	Amplitude $\beta$	0-400 $\mu\text{m}$
	Breath interval $t_0$	10 s
	Interval $\sigma$	0.5 s
Vibration ( $\boldsymbol{\xi}(t)$ )	Amplitude $\gamma$	0-60 $\mu\text{m}$
	Frequency $w_0$	7.5 rad/s
	Direction $\theta$	0- $2\pi$ rad
Blood flow ( $\boldsymbol{\zeta}(t)$ )	Speed	1-3 mm/s

identifies those frames most corrupted by a rigid-body motion that simulates the effects of breathing.

#### Errors in Blood-Signal Estimation

Simulation enables direct error estimation as all states are known. Let fractional error be defined as  $\epsilon = \|\mathbf{B} - \hat{\mathbf{B}}\|^2 / \|\mathbf{B}\|^2$  where  $\|\mathbf{B}\|$  is the known blood-echo power (see Eqs. (4.2) and (4.3)) and  $\|\hat{\mathbf{B}}\|$  is the estimated power from Eq. (4.25). When the clutter and noise filters are highly effective,  $\epsilon \simeq 0$ . Conversely, if filters are poorly designed and they remove all of the blood signal, then  $\epsilon \simeq 1$ . Although it is possible to obtain error values greater than one, in practice, we find  $0 < \epsilon < 1$  as shown below.

We measure two fractional errors:  $\epsilon_{best}$  computes  $\hat{\mathbf{B}}$  from training data while  $\epsilon_{GM}$  computes  $\hat{\mathbf{B}}$  using testing data. Since  $\epsilon_{best}$  uses exactly known training data, these errors are unavoidably generated by applying a hard threshold to data where the clutter and blood subspaces overlap.  $\epsilon_{GM}$  are

Table 4.2: Experimental Parameters

Parameter	Simulation	Phantom	In-vivo Tumor
Axial samples ( $M$ )	52	100	168-272
Axial sampling rate	40.0 MHz	12.5 MHz	24.0 MHz
Axial size	1 mm	6.2 mm	5.4-8.7 mm
Slow-time samples ( $N$ )	15	17	17
Slow-time sampling rate	1.0 kHz	1.0 kHz	1.0 kHz
Frame-time samples ( $K$ )	30	30	30
Frame-time sampling rate	20 Hz	15 Hz	10-15 Hz
Scan-line numbers ( $L$ )	50	53	120-234
Scan-line density	50/mm	4/mm	16.67/mm
Lateral size	1 mm	13.2 mm	7-14 mm
Spatial samples ( $S=LM$ )	2.6k	5.3k	20k-64k
Sub-block size ( $\dot{N} \times \dot{S} \times \dot{K}$ )	$17 \times 2.6k \times 30$	$17 \times 576 \times 30$	$17 \times 2.5k \times 30$
Slow-time division ( $J_1$ )	1	1	1
Spatial division ( $J_2$ )	1	15	400
Frame-time division ( $J_3$ )	1	1	1
Block numbers ( $J=J_1J_2J_3$ )	1	15	400
Classification threshold ( $\tau$ )	1	1	1

obtained under testing conditions and are consequently a more practical measure of filter performance.

Figure 4.7 illustrates how classification errors are influenced by clutter motion and flow speed. For the full range of conditions  $\beta < 400 \mu\text{m}$ ,  $\gamma < 60 \mu\text{m}$ , and  $\nu < 3 \text{ mm/s}$ , classification errors  $\epsilon_{GM} - \epsilon_{best}$  remain relatively constant between 0.1 and 0.2. However, increasing the rigid-body clutter amplitude expands the extent of the clutter subspace in the core tensor. This larger clutter eigen-bandwidth increases the overlap between clutter and blood subspaces, thus increasing fractional error. Alternatively, higher blood-flow speeds reduce the clutter-blood subspace overlap by shifting and expanding the blood subspace to smaller eigenvalues (larger index elements,  $i_3$ ).

### 4.3.2 Flow Phantom

A phantom study was conducted to assess microvascular flow estimation under experimental conditions. Figure 4.8 is a diagram of a dialysis cartridge containing a bundle of 0.6 mm inner-diameter cellulose fibers (Spectrum Lab-

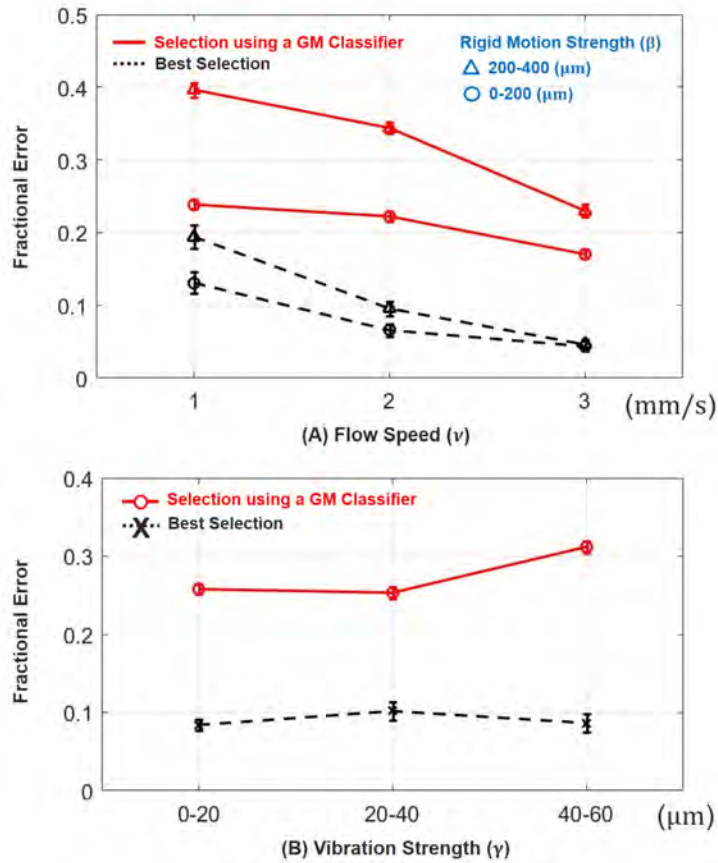


Figure 4.7: Fractional errors  $\epsilon_{GM}$  and  $\epsilon_{best}$  as functions of (A) flow speed for clutter amplitudes  $\beta$  and (B) vibration strengths  $\gamma$  at 2 mm/s flow speed. Points and error bars denote sample means and standard deviations of the mean, respectively. Large clutter motion and slow blood speeds generate the largest classification errors because of subspace overlap.

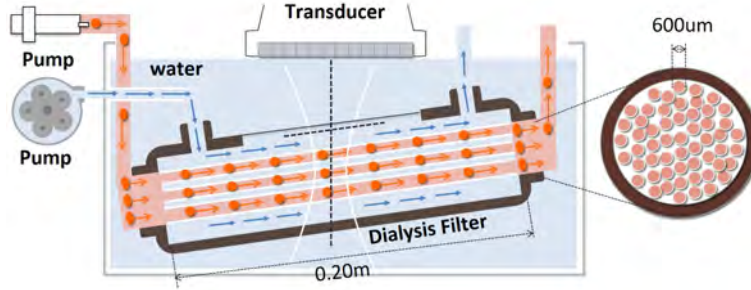


Figure 4.8: A flow phantom mimicking blood circulation consists of a dialysis cartridge and two pumping systems. A syringe pump infuses either water (control state) or blood-mimicking fluid (perfusion state) constantly into 0.6 mm fibers. A peristaltic pump circulates water pulses outside the fibers for clutter motion. A linear transducer scans the cartridge through an acoustic window for echo acquisition.

atories Inc., Rancho Dominguez, CA USA). Flow in the fibers was controlled by a programmable syringe pump injecting at a constant rate either pure water for the control state or blood-mimicking fluid (CIRS, Norfolk, VA USA) for test states. In addition, pulsatile water flow was generated outside the fibers using a peristaltic pump to induce sinusoidal clutter motion at frequencies between 0 and 0.5 Hz. We removed a portion of the thick plastic case protecting the cellulose fibers and wrapped that area with paraffin film (Parafilm, Bemis Co. Inc., Neenah WI, USA) to provide an acoustic window and housing structure for pulsatile clutter generation. The cartridge was immersed in degassed water for ultrasound scanning. A Vevo 2100 system with an MS200 linear array operated at 12.5 MHz (FUJIFILM VisualSonics Inc. Toronto, Ontario, Canada) was used to acquire IQ echo data in color-flow mode for off-line processing.

We compared five flow states: control state  $i = 1$  has stationary water in the fibers, 0 ml/min;  $i = 2$  has stationary TM blood, 0 ml/min;  $i = 3$  has TM blood at 1 ml/min;  $i = 4$  has TM blood at 2 ml/min; and  $i = 5$  has TM blood at 3 ml/min. At each flow state, we acquired data at four clutter motion levels:  $j = 1$  is no motion (peristaltic pump off),  $j = 2$  is pumping with rotation frequency 0.16 Hz,  $j = 3$  at 0.33 Hz, and  $j = 4$  is 0.5 Hz. These values span the 12-20 breath/min range. There were 12 acquisitions recorded per state and motion level, each 2 seconds in duration (30 Doppler frames). Power Doppler maps  $\mathbf{P}_k$  were formed for regions 6.2 mm axially by 13.2 mm laterally (see white boxes in Fig. 4.9). All experimental and filter

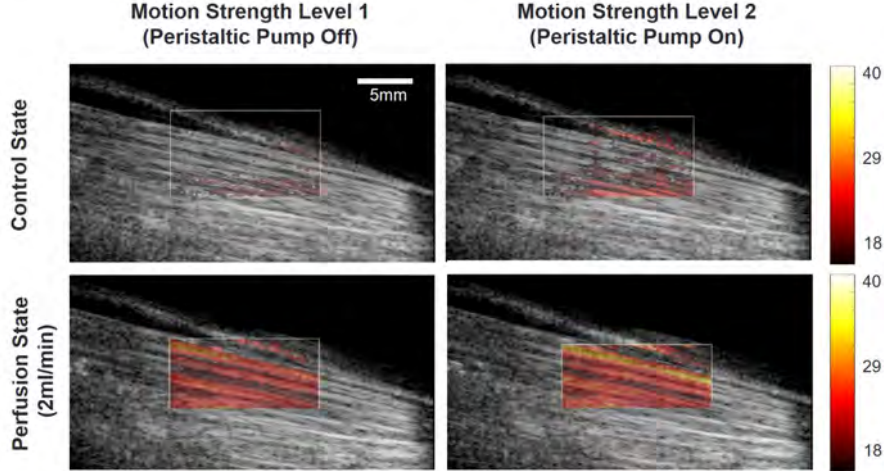


Figure 4.9: PD images of 0.6 mm-dia cellulose-fiber flow phantom at 12.5 MHz. Each is a filtered PD map superimposed on the corresponding B-mode image. Columns display two clutter levels. Rows display the control and 2 ml/min flow states. Color bar indicates signal power.

parameters are summarized in the column of Table 4.2 labeled “phantom.”

Figure 4.9 displays examples of PD maps superimposed on their B-mode images for two clutter levels. Post-filter signal power was found to increase with clutter level. The changes were quantified by computing pixel average  $s_{ijk} = \frac{1}{ML} \sum_{(m,l)} \mathbf{P}_k[m, l]$  for every PD image. Figure 4.10 shows values for the 12 acquisitions,  $\bar{s}_{ij} = \frac{1}{12} \sum_{k=1}^{12} s_{ijk}$ , for flow state  $i$  and clutter motion level  $j$ . We see that post-filter signal power (dB) increases linearly with flow rate. Unfortunately, the rate of increase depends on the clutter motion level.

The slope change with clutter level in Fig. 4.10 is consistent with our findings in the simulation results. Increasing the levels of clutter energy for fixed flow states increases the overlap of blood and clutter subspaces within the core tensor. The overlap is greatest for the slowest flow velocities. Because we employ a hard threshold, the increase in post-filter signal power with clutter level at the smallest blood speeds is expected. High-amplitude rigid-body clutter motion generates incomplete separation of tissue and blood signals with the effect of reducing PD image contrast as discussed below.

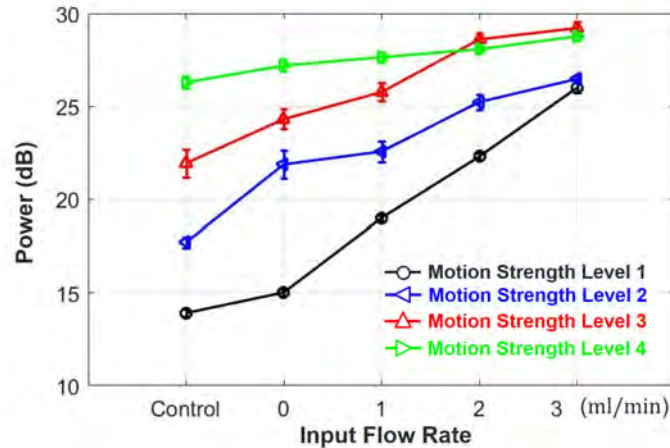


Figure 4.10: Post-filtered echo power versus input flow for four clutter levels. Error bar indicates standard errors from averaging results of 12 acquisitions.

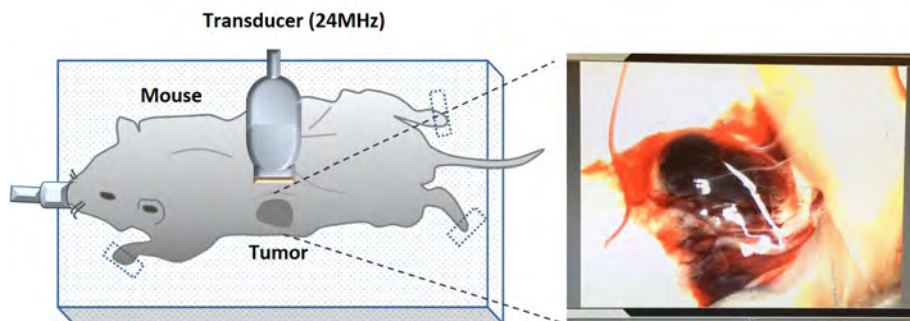


Figure 4.11: A murine model of melanoma is illustrated. A mouse implanted with tumor cells is scanned in a prone position. Data are acquired at 24 MHz with the Vevo 2100 over three weeks.

### 4.3.3 *In vivo* Tumor Study

To further test our imaging methods, we scanned implanted mouse melanomas, *in vivo*. Tumor cells injected subcutaneously into the flank of male black C57BL/6 mice (Charles River Laboratories, US) were investigated over time as tumors grew in size and vasculature. Figure 4.11 illustrates the scan positioning. Echo data were acquired 1, 2, and 3 weeks post-implantation using the Vevo 2100 system and the MS400 transducer at 24 MHz (see Table 4.2). Mice anesthetized with 1-3% isoflurane are scanned to acquire 3 s of echo data (30 sequential Doppler frames at 10 Hz frame rate). The 24 MHz pulses provide high B-mode spatial and contrast resolutions, allowing tumors to be readily located as hypoechoic regions. The clutter-filter classifier that was

trained using simulation data was applied to the tumor data to identify core elements belonging to the clutter subspace. We also applied the methods of Section 4.2.7 to set velocity windows for slow flow ( $<4$  mm/min) and fast flow ( $>4$  mm/min) regions. The PD map was determined from the blood signal measured using Eq. (4.25).

Figure 4.12 displays one example of low- and high-flow PD images acquired at weeks 1-3. One week post-implantation, the small nascent tumor appears as a hypoechoic region of enhanced perfusion. The tumor grows rapidly after one week, increasing its microvascular density. This tumor has only a few larger vessels with higher velocity flows. Note that the breathing rate of the anesthetized mouse was slowed, making it easy to acquire 3 s of echo data between breaths. In this example, clutter was primarily from stationary and vibrating tissue.

## 4.4 Discussion

From the simulation, phantom, and *in vivo* tumor results, we find a consistent picture regarding the performance of the clutter filter proposed for PD imaging from a 3-D echo array. The classifier-based filter works well when the amplitude of clutter motion is small and spatially uniform, e.g., rigid-body motion. In that case, the clutter subspace is relatively narrow band and confined to the first few eigenstates. Consequently, the clutter and blood subspaces in  $\mathcal{G}$  are largely disjoint, and thus the clutter subspace is readily suppressed with little effect on the blood subspace using a hard-threshold filter. In other words, feature vector  $\mathbf{z}$  from Eq. (4.18) in conjunction with the classifier of Eq. (4.19) is able to correctly label core elements of  $\mathcal{G}$ . Our clutter filter is well designed for these tumor imaging conditions because the clutter eigen-bandwidth is narrow.

In contrast, clutter-signal power in the phantom data was pulsatile, with a broad-band clutter subspace that overlapped the TM-blood subspace. We set the filter classifier to capture all of the blood power, and as a result the post-filter signal power contains more clutter power at slow flows than at fast flows. For this reason, power-Doppler image contrast was reduced in Fig. 4.10 as more clutter power was introduced. In addition, the resistance to flow through the dialysis fibers at the lowest flow states was highly variable;

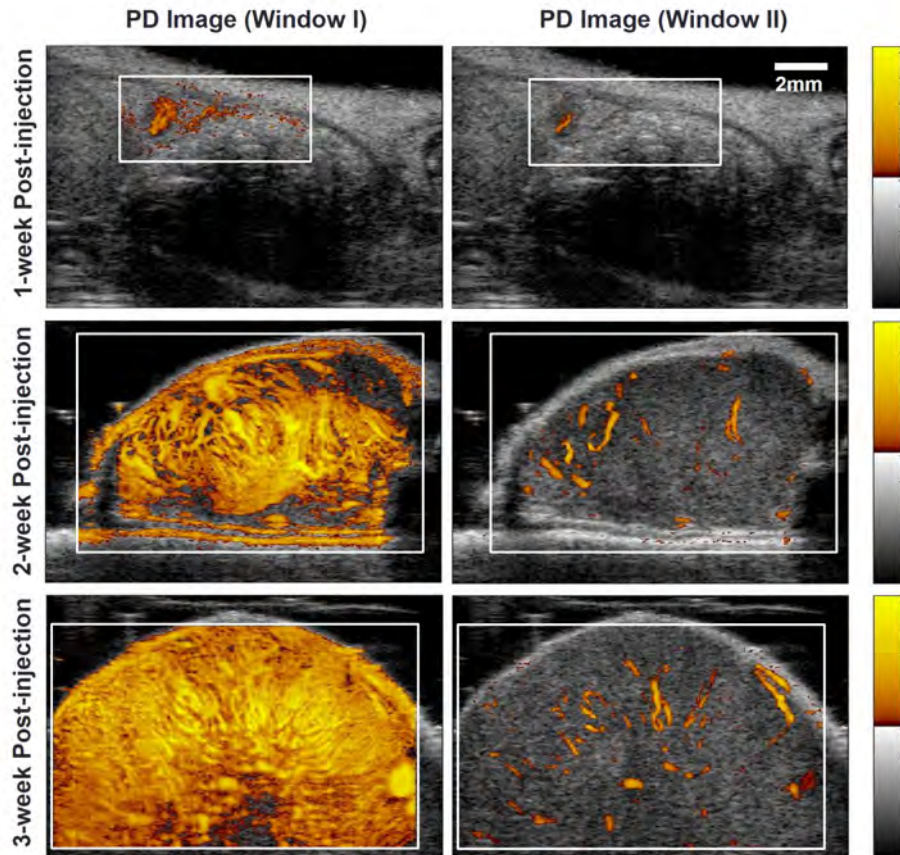


Figure 4.12: PD images of a murine melanoma 1 to 3 weeks after implantation. Tumor size and microvasculature clearly increase with time. The left column displays PD maps of microvascular flow and perfusion for blood speeds  $<4$  mm/s while those in the right column are flows  $>4$  mm/s. All imaging was implemented in MATLAB 2015b on an Intel processor i5-4300U CPU, 2.50 GHz. HOSVD computation was performed using a truncation technique supported by Tensorlab toolbox ([www.tensorlab.net](http://www.tensorlab.net)) to minimize running time. The time to compute all processing for one PD image ( $5.4\text{mm} \times 7\text{mm}$ , 1 week) is around 1 min.

we found that few fibers often carried most of the flow at higher speeds. As flow increased above 2 ml/min, flow among fibers became more uniform. In effect, the flow phantom posed more challenges to successful clutter filtering than *in vivo* tumor imaging.

To improve clutter filtering when tissues move with high amplitude and eigen-bandwidth, we are searching for additional  $\mathbf{z}$  components that can specifically identify those physical attributes. Such features might emerge from multimodal perfusion imaging investigations if another modality can provide appropriate independent information (Chapter 5). Alternatively, we are seeking soft-threshold decision functions that can recognize when more than one signal source is contributing to a core element. It is clear from the tumor images of Fig. 4.12 that peripheral microvascular imaging offers clutter conditions where our methods work very well.

Note that the simulation and phantom data in our report each provide small-vessel flow conditions but no capillary-perfusion-like signal, the latter being characterized by the slowest and most spatially disorganized red-blood-cell (RBC) movements. Both microvascular flow and perfusion are present in Fig. 4.12 as it was in a previous report involving ischemic mouse hindlimb images (Chapter 3). Perfusion is well represented in the power-Doppler spectrum that does not depend on the Doppler angle, but, unlike color-flow images, PD images offer no velocity information. We are able to obtain some speed ranging by partitioning eigenvector spectra (Section 4.2.7). We showed in Chapter 3 that eigenvector spectral images display distinct linear patterns when RBC movement is directed, as in vessel flows, and diffuse patterns when RBC movement is disorganized as in capillary perfusion. The 3-D eigenspace provided by HOSVD processing offers a wealth of specific information about scatterer movement that is encoded in pulse-echo signal arrays.

## 4.5 Summary and Conclusions

The sensitivity of PD images to tissue perfusion was increased by creating a frame-time axis in the acquired echo-data array in addition to the slow-time and spatial axes. The frame-time axis provides a high density of Doppler spectrum samples at frequencies corresponding to tissue perfusion signals. The perfusion signal was uncoupled from tissue clutter using a 3-D SVD

that generates a 3-D core tensor and three sets of eigenvectors describing the slow-time, spatial, and frame-time features of the echo signals. In this report, we describe a feature-vector classifier with elements computed from the 3-D eigenspace. Three of the features report eigenvalue energy and two are similarity measures. This statistical classifier examines each core-tensor element to decide if it is predominantly of clutter or non-clutter origin. Coupling the clutter filter with an acquisition noise filter and velocity discriminator, we image fast and slow blood-flow states *in vivo*. The method works well for narrow eigen-bandwidth clutter signals but generates progressively reduced-contrast PD images as the clutter eigen-bandwidth increases. This approach to microvascular/perfusion imaging performs well in peripheral vasculature imaging.

# CHAPTER 5

## CLINICAL APPLICATION

### 5.1 Introduction

Peripheral artery disease (PAD) is a prevalent disorder that becomes disabling when poorly managed. PAD reduces circulation in the extremities because of atherosclerosis, diabetes, and other microvascular maladies. Affected patients are vulnerable to debilitating systemic cardiovascular events like strokes and infarcts. PAD affects more than 8 million people in the USA today and is expected to affect 20 million by 2050 given a sedentary lifestyle in an aging population [59].

As PAD progresses, the narrowing vasculature results in a decreased perfusion and increased hypoxia. These changes can activate revascularization processes [60]. Angiogenesis, which is triggered under hypoxic conditions, leads to the formation of new capillary beds from preexisting vessels. Arteriogenesis, which is triggered by changes in the biomechanical properties of the vasculature as a result of decreased blood flow, leads to the enlargement of preexisting arteriolar connections.

The evaluation of interrelated functional parameters is required to understand the progression of PAD and the bodily response to the disease. The parameters include blood perfusion and oxygenation levels in different muscle tissues. The aim of the research is to employ an integrated multimodal approach to study PAD with ultrasound (US) imaging, photoacoustic imaging (PA), and laser speckle contrast imaging (LSCI). The research is also aimed to validate our US perfusion imaging proposed in previous chapters. The enhanced sensitivity enables differentiation of perfusion between healthy and ischemic states. The images also allow tracing perfusion changes in a deep region of interest while angiogenesis progresses.

## 5.2 Method

### 5.2.1 Murine Ischemic Model

The operation protocol to induce peripheral ischemia is described in the method section in Chapter 3. Briefly, male black (C57BL/6) mice (Charles River Laboratories, US) were subjected to the right femoral artery ligation and they were serially scanned with the imaging modalities before and immediately after closing the incision to confirm the ischemic status. The imaging proceeded at various time points up to two weeks post-surgery to monitor spatiotemporal changes. All experiments were performed according to the guiding principles of the American Physiological Society and approved by the Institutional Animal Care and Use Committee.

### 5.2.2 US Imaging

A subset of seven (n=7) animals were used for perfusion assessment employing US. Animals were imaged prior to ligation surgery and at a series of post-operative time points (10, 20, 30, 40, 50, and 60 minutes, and 1, 2, 7, and 14 days). Echo data were acquired using a Vevo 2100 system and an MS 400 linear-array transducer (FUJIFILM VisualSonics Inc. Toronto, Ontario, Canada). The acquisition and processing parameters are summarized in Table 5.1. The total imaging methods are described in Chapter 3.

### 5.2.3 Laser Speckle Contrast Imaging

Seven (n=7) animals imaged previously with ultrasonic power Doppler were also scanned using laser speckle contrast imaging prior to ligation surgery and at a series of post-operative time points (10, 20, 30, 40, 50, and 60 minutes, and 1, 2, 7, and 14 days). Images were obtained using a moorFLPI-2 laser perfusion imager (Moor Instrument, UK) operated from a Windows-based computer system installed with the moorFLPI software (moorFLPI Measurement V3.0, Moor Instruments, Devon, UK). High-resolution speckle images were acquired using a  $768 \times 576$  pixel grayscale charge-coupled device camera set to record each frame for a duration of 60 seconds. In addition, the

Table 5.1: Parameters

Parameter	Value
Axial (fast-time) samples ( $M$ )	200-272
Axial sampling rate	24.0 MHz
Axial size	6.4-8.7 mm
Slow-time samples ( $N$ )	17
Slow-time sampling rate	1.0 kHz
Frame-time samples ( $K$ )	100
Frame-time sampling rate	9 Hz
Scan-line numbers ( $L$ )	240-250
Scan-line density	16.67 lines/mm
Lateral size	14.4-15.0 mm
Spatial samples ( $S=LM$ )	48000-68000
Sub-block size ( $\dot{N} \times \dot{S} \times \dot{K}$ )	$17 \times 768 \times 30$
Slow-time division ( $J_1$ )	1
Spatial division ( $J_2$ )	1600
Frame-time division ( $J_3$ )	10
Sub-block numbers ( $J=J_1 J_2 J_3$ )	16000

feet of three (n=3) mice were imaged prior to surgery and at 1 hr, 1 day, 2 days and 7 days post-surgery. For collateral circulation assessment, the skin was removed from the right hindlimb of the animal. The mice were imaged prior to surgery, and subsequently at 2, 10, and 25 min post-ligation.

#### 5.2.4 Photoacoustic Imaging

Another subset of seven (n=7) mice was used for PA imaging. Each animal was imaged with Endra Nexus 128 PA tomographer (Endra, Inc., Ann Arbor, MI, USA) at (20, 30, 40, 50, and 60 minutes, and 1, 2, and 7 days) post-surgery. Images were acquired at 750 and 850 nm using continuous rotation mode with a 6 second rotation time. A 3D reconstruction was performed for each image, and signal intensity was accumulated over an 8 mm thick slab. The signal in each PA image was quantified by determining the mean PA signal in a 2 mm<sup>2</sup> region of interest (ROI). A ratiometric signal was determined by taking the ratio of signal at 750 nm to 850 nm. Data was processed using the freely available Horos software (Horos Project, <https://www.horosproject.org/>).

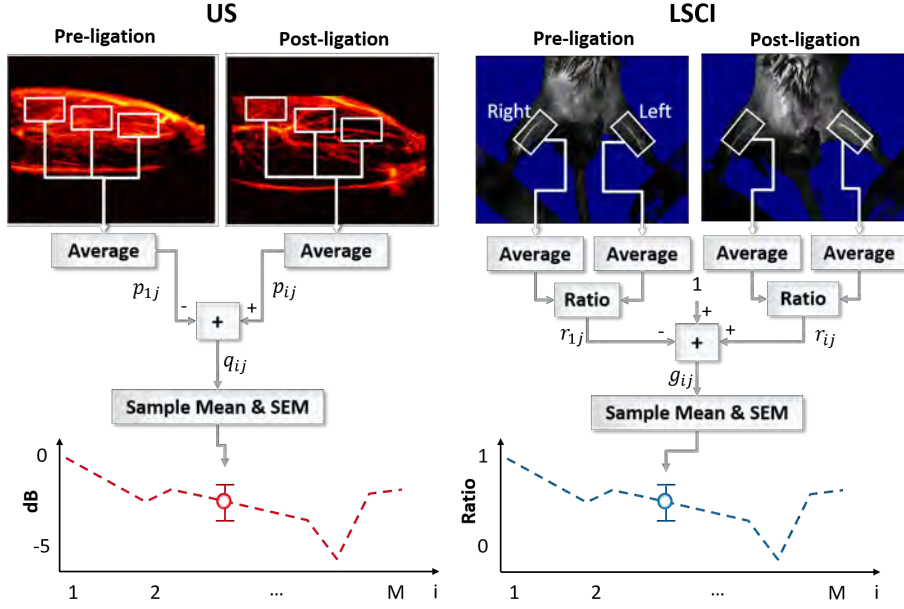


Figure 5.1: Perfusion quantification using US and LSCI. US and LSCI images were obtained at multiple time points before and after femoral artery ligation. The white rectangular windows in the images represent individual ROIs over which perfusion was averaged. In the US images, the difference between the pre- and post-operative state was computed for each mouse sample. Subsequently, the mean and SEM of this difference were plotted at each time point. The graph shows 0 dB pre-ligation ( $i = 1$ ) as a reference, and the relative changes for all post-ligation timepoints ( $i > 1$ ). In the LSCI images, the ratio between an ischemic right hindlimb region and its corresponding healthy left hindlimb region was computed, and their difference (plus unity, such that all values are relative to 1) was plotted.

### 5.2.5 Perfusion Trend Analysis for Ultrasound and Laser Speckle Contrast Imaging

Perfusion images obtained through power Doppler US were used to track tissue perfusion changes over the course of two weeks. Through imaging the animal hindlimbs at various time points (before and after ligation), we were able to track the average perfusion changes over the regions illustrated in Fig. 5.1. These regions intentionally exclude arteries in order to focus on tissue perfusion. The depth of each region was set to less than 6 mm to provide a consistently high echo signal-to-noise ratio. The average perfusion during the  $i$ th time point in the  $j$ th mouse is represented as

$$p_{ij}, i \in \{1, \dots, M\}, j \in \{1, \dots, N\}, \quad (5.1)$$

where  $M$  and  $N$  are the number of time points and mice included in this study, respectively. We compute the change in perfusion over time as  $q_{ij} = p_{ij} - p_{1j}$  where  $p_{1j}$  is the pre-ligation regional perfusion value. The temporal variation is analyzed by plotting sample mean  $\bar{q}_i = \frac{1}{N} \sum_{i=1}^N q_i$  and standard error of the mean (SEM)  $\tilde{q}_i = \sqrt{\frac{1}{N} \sqrt{\frac{1}{N-1} \sum_{i=1}^N (q_i - \bar{q}_i)^2}}$  for every time point  $i$ .

The trend for LSCI was obtained by a comparable procedure, but we report the ratio of signal from the right ischemic hindlimb to that of the left control hindlimb:

$$r_{ij} = \langle p_{ij}^{(R)} \rangle / \langle p_{ij}^{(L)} \rangle, \quad (5.2)$$

where  $\langle p_{ij}^{(R)} \rangle$  and  $\langle p_{ij}^{(L)} \rangle$  are perfusion averages over the boxes on right and left hindlimbs, respectively. Because the spatial absolute image values are highly sensitive to ambient light conditions, we normalize the perfusion change using  $g_{ij} = r_{ij} - r_{1j} + 1$  and plot the mean and SEM for  $g_{ij}$  at every time point.

### 5.2.6 Blood Oxygenation Analysis for Photoacoustic Imaging

Because the oxygenated ( $\text{HbO}_2$ ) and deoxygenated ( $\text{HbR}$ ) forms of hemoglobin have different near-infrared absorption properties, PA is able to detect the relative level of blood oxygenation. Briefly, the amplitude of the acquired PA image describes the local energy absorption at wavelength  $\lambda_i$ . This in turn can be expressed as  $\phi(\lambda_i, x, y, z)$ , with a spatial average  $\bar{\phi}(\lambda_i)$ . The contribution of the two forms of hemoglobin to the spatial mean absorption can be represented as

$$\bar{\phi}(\lambda_i) = \epsilon_{\text{HbR}}(\lambda_i)[\text{HbR}] + \epsilon_{\text{HbO}_2}(\lambda_i)[\text{HbO}_2], \quad (5.3)$$

where  $\epsilon_{\text{HbR}}$  and  $\epsilon_{\text{HbO}_2}$  are the molar extinction coefficients of HbR and HbO<sub>2</sub> at wavelength  $\lambda_i$ , respectively. The operator  $[\cdot]$  denotes the relative concentration of hemoglobin. In this study, we used three wavelengths,  $\lambda_1=750$  nm,  $\lambda_2=800$  nm, and  $\lambda_3=850$  nm. The two concentrations can thus be estimated

by a least squares solution as

$$\begin{bmatrix} [\text{HbR}] \\ [\text{HbO}_2] \end{bmatrix} = \left( \begin{bmatrix} \epsilon_{\text{HbR}}(\lambda_1) & \epsilon_{\text{HbO}_2}(\lambda_1) \\ \vdots & \vdots \\ \epsilon_{\text{HbR}}(\lambda_3) & \epsilon_{\text{HbO}_2}(\lambda_3) \end{bmatrix} \right)^\dagger \begin{bmatrix} \phi_{jk}(\lambda_1) \\ \vdots \\ \phi_{jk}(\lambda_3) \end{bmatrix}, \quad (5.4)$$

where  $(M)^\dagger = (M^T M)^{-1} M^T$  denotes pseudo-inverse of the matrix  $M$ . The relative change in oxygenation is consequently given as  $\eta = [\text{HbR}]/[\text{HbO}_2]$ . We employed the table in [61] for corresponding molar extinction coefficients. A total of seven (7) mice were scanned at several time points before and after ligation. We computed each ratio  $\eta_{jk}$  where  $j$  and  $k$  are indices of the time point and sample, respectively, and finally plotted the sample mean and SEM for every time point to trace the change.

### 5.3 Results

The primary goal of monitoring the circulatory system using multiple imaging techniques is to find an accurate, continuous, and non-invasive strategy that can help assess changes in tissue perfusion and the breakdown of homeostasis. Although several methods have been established for perfusion imaging in the clinical setting, none by itself can offer the fine resolution and variable ranges of depth necessary for detecting microvascular changes. To bridge this divide, we adopted three complementary imaging techniques (US, PA, and LSCI) with various penetration depth (see Table 5.2). These imaging modalities enable us to “connect the dots” between changes in blood flow through microvascular networks shortly after the onset of ischemia, all the way through to large-scale changes in blood supply seen days or weeks later (Fig. 5.2).

Table 5.2: Non-Invasive Imaging in Small Animal PAD Model

Imaging Modality	Depth	Pixel/Voxel representation
US (24 MHz)	4-6 mm	Echo power in dB scale
PA	3-4 mm	Optical absorption
LSCI	1 mm	Optical power in flux scale

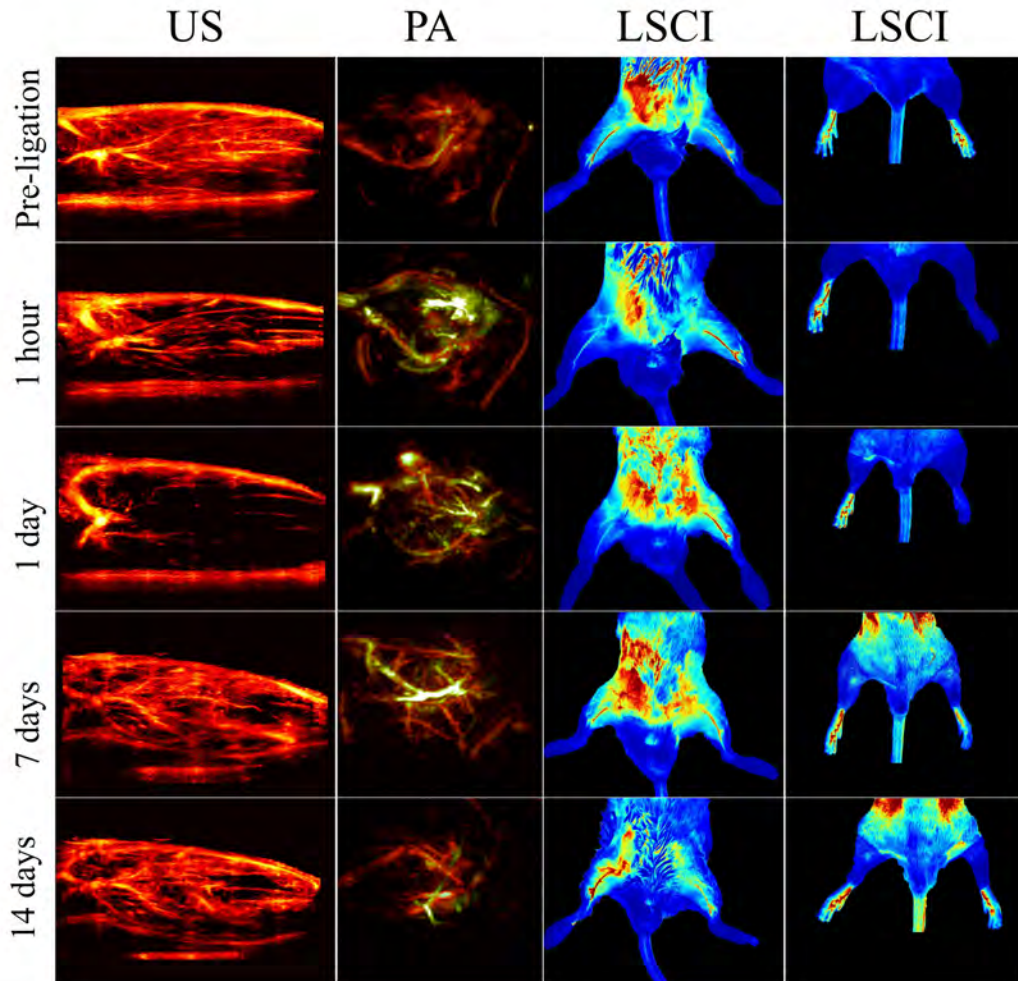


Figure 5.2: Representative multimodal imaging data presented at a series of time points (prior to and following ligation). Each column shows how a different circulatory parameter changes over time as the mice recover. The first column highlights perfusion as a series of  $10 \text{ mm} \times 15 \text{ mm}$  vertical cross sections of ischemic tissue imaged using US. Prior to ligation, perfusion generally appears strong, except for the distal regions of the limb where the signal appears to be diminished primarily due to acoustic attenuation. The second columns show PA images of the ischemic tissues excited at  $750 \text{ nm}$  (for HbR detection, green color) and  $850 \text{ nm}$  (for HbO<sub>2</sub> detection, red color). The third column represents LSCI images of the legs in a horizontal view. The right hindlimbs (appearing on the left side of the images) underwent femoral artery ligation, while the left hindlimbs were used as controls within each animal. The fourth column represents LSCI images of feet.

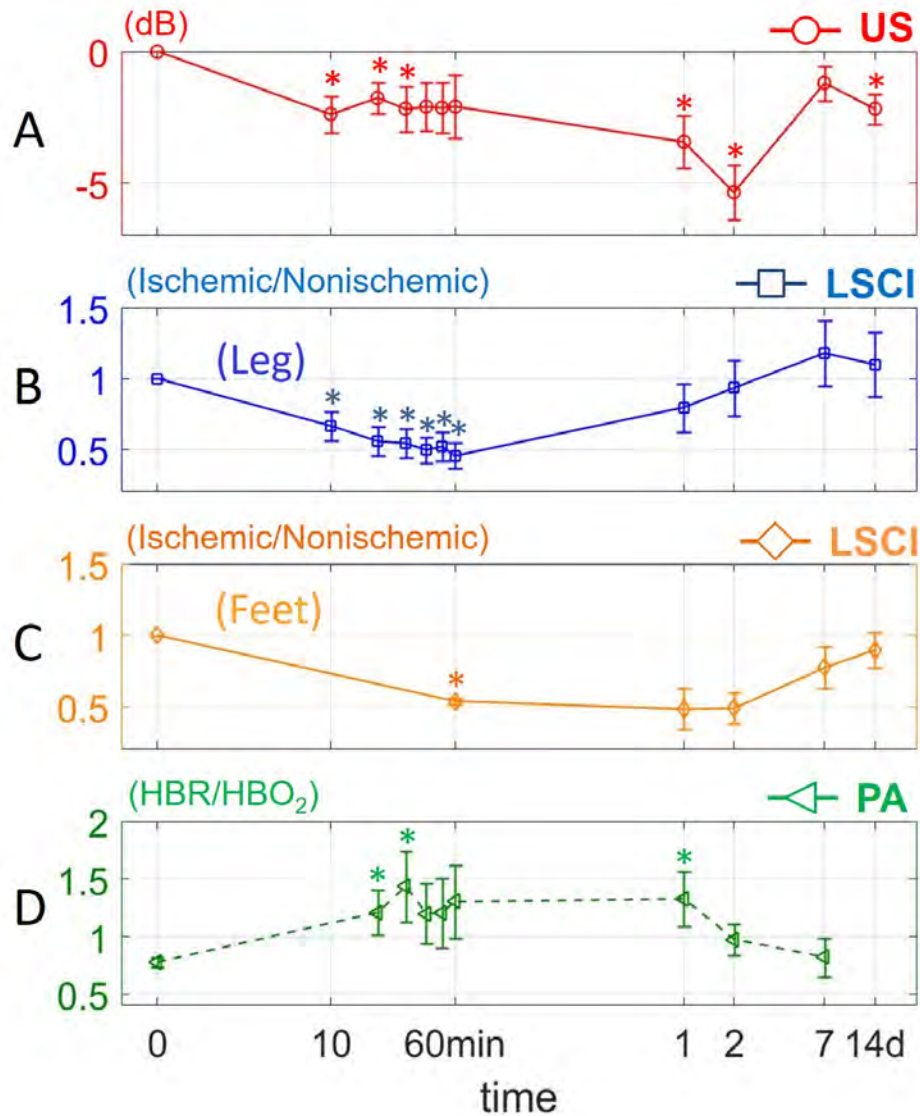


Figure 5.3: Changes in perfusion and hypoxia over a logarithmic timeline. Points marked (o) and (□) are for perfusion estimates using US and LSCI, respectively. Points marked (◁) indicate the ratio of deoxygenated to oxygenated hemoglobin (HbR/HbO<sub>2</sub>) as measured via PA. (A)–(D), are plots of each measure individually. The mark (\*) above each point indicates a statistically significant ( $p < 0.05$ ) difference from the pre-ligation state.

### **Ultrasound enables estimation of deep-tissue peripheral perfusion**

For each of seven experimental mice, US imaging sessions were performed before the surgical ligation, every 10 minutes after surgery (up to an hour), and at 1, 2, 7 and 14 days to monitor spatiotemporal changes in blood perfusion. We found that within the first 10 minutes, a significant drop in the perfusion signal was detected (see Fig. 5.3 (A)). The lowest perfusion levels, however, were not observed until the 1 or 2 days post-surgery. By day 7 perfusion was found to have recovered to near pre-ischemic level.

### **LSCI reveals the rapid dynamics of the subcutaneous tissue perfusion**

While the deep tissue (imaged with US) showed a relatively slow decrease in blood perfusion after surgery, the dynamics of the surface tissue (assessed via LSCI) were considerably faster. The LSCI signal was observed to continuously decrease over the entire first hour after ligation, and by day 1 had already started to recover (see Fig. 5.3 (B)). Indeed, while the deep tissue showed its lowest level of perfusion at the day 2 timepoint, the superficial tissue measurements indicated almost complete recovery. This is likely due to the fact that surface tissue contains a higher density of collateral blood vessels, which, during vascular occlusion, can help to rapidly recover blood perfusion [62].

### **LSCI demonstrates a slow perfusion recovery in lower extremities**

The traditional approach of assessing perfusion in a laboratory setting involves imaging the feet of animals using LSCI. As shown in Fig. 5.3 (C), we observed an immediate decrease in the ischemic-to-non-ischemic perfusion ratio followed by a slow but steady recovery that takes up to 14 days.

### **Photoacoustic imaging imparts functional microvascular parameters**

In contrast to ultrasonic and laser Doppler imaging, photoacoustic imaging is capable of quantifying several important physiological parameters, including levels of oxygenated ( $\text{HbO}_2$ , detected at 850 nm) and deoxygenated ( $\text{HbR}$ , detected at 750 nm) hemoglobin. Using light at wavelengths in the near-infrared region we found that the ratio of  $\text{HbR}$  to  $\text{HbO}_2$  increased approximately 1.2-fold after ligation (see Fig. 5.3 (D)), and maintained this high level throughout the first day. Some recovery was seen by day two, however by day seven, the ratio had reverted to its pre-ligation value.

## 5.4 Discussion

One of the primary drivers of this investigation was to explore applications of a new power Doppler US technology sensitive enough to not require exogenous contrast enhancement when detecting spatiotemporal changes in muscle perfusion. Although US imaging has been a mainstay in the healthcare industry for over 60 years, and it is widely used for the detection of blood circulation, its limited sensitivity in low-flow conditions has rendered it unsuitable for imaging the peripheral microvasculature until now. The power Doppler US methodology we employed in this study can detect relative perfusion changes within capillary beds using conventional instrumentation that samples and filters echo data in new ways. Using this method, we monitored the 14 day ischemia-reperfusion time course in healthy mice throughout the hindlimb (Fig. 5.3 (A)). We used 24 MHz (about 3 times the frequency of clinical imaging) because of the small size of the hindlimb. This method offers a safe and low cost approach to serially assess tissue perfusion.

We used this power Doppler method, along with several other imaging techniques, to construct a comprehensive timeline of the bodily response to peripheral vascular occlusion at the physiological levels. In the deep tissue, we found a slow decrease in the perfusion feature that manifested over the course of approximately 48 hours (although the shallower tissue showed a considerably faster drop-off). The ability to perform fast serial assessments also proved critical to the possible detection of a reactive hyperemia response shortly after ligation. Although modest in size, we note an increase in tissue perfusion at the 20 min time point relative to the 10 and 30 minute values (a similar uptick in oxygenation was noted at the 30 min time point (Fig. 5.3 (A&D))). One possible explanation may lie in a surge of endothelial nitric oxide (NO) production stimulated by the hypoxia conditions. Previous studies have shown that: (1) NO modulates the consumption of oxygen when blood flow is restricted by competitive inhibition of cytochrome oxidase [63], (2) hypoxic tissue expression increased levels of vascular endothelium growth factor (VEGF), which in turn gives rise to endogenous release of NO. Additional studies will be required to establish the role of NO in short-term perfusion and to investigate possible therapeutic effects of NO on the ischemic microenvironment.

With the utility of our new ultrasonic power Doppler technology estab-

lished, we next sought to use it as part of a broader multimodal imaging strategy to study the onset of and recovery from PAD. To that end, we employed LSCI and PA over the study time course to non-invasively inspect superficial blood perfusion and oxygenation, respectively.

Within the surface tissue, the LSCI data showed that hindlimb recovery from ischemia occurs considerably faster than in deeper tissue. While the US imaging revealed that it took approximately 7 days to show signs of vascular recovery within the muscle mass, the surface tissue was clearly recovering as early as 48 hours post-ligation. The simplest explanation for this observation lies in the differences in vascular physiology of the surface and deep tissues. In addition to angiogenesis, there exists a secondary type of vascular remodeling which involves the growth of preexisting collateral arterioles into functional collateral arteries. Dubbed arteriogenesis, this type of blood vessel growth is regulated not by hypoxia, but by the changes in shear stress that accompany the decrease in blood pressure associated with ligation [64, 65]. Because the vascular density in the surface tissue is generally quite high (presumably due to selection pressure favoring fast wound healing), arteriogenesis in these tissues might lead to the recovery of blood flow much faster than would be possible relying on angiogenesis alone.

For patients with PAD, amputation of the extremities may become necessary in situations where there is extensive tissue death due to prolonged ischemia. Indeed, the clinical presentation of severe ischemic ulcers or frank gangrene are recognized as the sixth stage of PAD manifestation according to Rutherford’s classification [66]. We therefore investigated perfusion within the feet of our animals using LSCI and found that blood flow recovered more slowly in the feet than in the distal muscle mass, taking approximately 14 days on average (in close agreement with reports by other authors) [67]. This slow recovery highlights the necessity of developing new screening methods capable of detecting PAD early on, before irreparable damage is done.

PA with a penetration depth of 5 mm enables label-free imaging of microvascular flow with high signal-to-noise ratio. This allows users to easily differentiate superficial capillaries and deep tissue vessels [68], but it can also be used to characterize functional microvascular parameters including HbO<sub>2</sub> and HbR concentrations [68, 69]. We found that 20 min after ligation, the ratio of HbR/HbO<sub>2</sub> increased (suggesting hypoxia), and this enhancement continued until approximately two days after ligation, when the blood

oxygenation began to rise (Fig. 5.3 (D)). Because the US measurements indicated that perfusion did not show signs of recovery until day 7, these results seem to indicate that blood oxygen levels can recover early in the angiogenic response.

# CHAPTER 6

## CONCLUSION

Ultrasound imaging combined with novel signal processing techniques has much potential to increase diagnostic accuracy, leading to better treatment options. The purpose of this research is to develop optimal blood perfusion imaging methods that remain safe and are available at a low cost for widespread clinical use. Forming a multidimensional array using a unique sampling method can increase sensitivity to disorganized perfusion without reducing sensitivity to directed arterial flow. The proposed HOSVD filtering technique effectively isolates blood components from tissue motion. This technique takes advantage of the full range of statistical information in the echo signal to decouple the independent scattering sources in adaptively determined vector spaces. The classifier, using extracted features, maximally nullifies clutter and retains blood components. The experimental results, attained using *in vivo* melanoma tumor imaging at 24 MHz, show significant clutter rejection without a loss of perfusion signal. Comparisons with other imaging modalities in well-known murine ischemic model enable us to establish the clinical potential of US imaging for the diagnosis of PAD.

Medical imaging is undergoing a transformation, becoming an essential contributor to medical data sciences. Data-driven techniques for image reconstruction and interpretation are revolutionizing how we attain patient information and images to make ideal medical decisions. Advanced computing power enables us to implement data processing based on complex statistical models. At the center of all diagnostic and therapeutic methods is the need to assess blood flow and perfusion. Our innovation in this regard is to modify echo acquisition and expand dimensionality to increase the sensitivity of non-enhanced US imaging to very slow and disorganized flows. Statistical filtering appropriately reduces data dimensionality to improve perfusion specificity. Methods can be implemented on an existing commercial scanner, which increases the utility of Doppler techniques without redesigning

the instrument.

Future work would consider methods for use at diagnostic frequencies (5-12 MHz) to (1) explore other organ systems in the animal models and (2) adapt the technique for human use. Low frequencies increase penetration depth at the expense of the signal power of RBCs. To compensate for this sensitivity, the role of acoustic beamforming is important. Standard processing delays and sums the echoes from multiple sensors in the transducer receive aperture merely to alleviate white noise. Access to the pre-beamformed data makes it possible to develop more flexible filtering techniques to extract weak blood components. The processing of a large amount of data requires high-performance computing. Developing fast decomposition algorithms and implementing them using a graphics processing unit (GPU) are needed to speed up image formation.

## REFERENCES

- [1] R. N. Pittman, “Regulation of tissue oxygenation,” in *Colloquium Series on Integrated Systems Physiology: From Molecule to Function*, vol. 3, no. 3. Morgan & Claypool Life Sciences, 2011, pp. 1–100.
- [2] V. Goh, S. Halligan, J. A. Hugill, and C. I. Bartram, “Quantitative assessment of tissue perfusion using MDCT: comparison of colorectal cancer and skeletal muscle measurement reproducibility,” *American Journal of Roentgenology*, vol. 187, no. 1, pp. 164–169, 2006.
- [3] C. A. Cuenod and D. Balvay, “Perfusion and vascular permeability: basic concepts and measurement in DCE-CT and DCE-MRI,” *Diagnostic and Interventional Imaging*, vol. 94, no. 12, pp. 1187–1204, 2013.
- [4] A. W. Pollak, P. T. Norton, and C. M. Kramer, “Multimodality imaging of lower extremity peripheral arterial disease,” *Circulation: Cardiovascular Imaging*, vol. 5, no. 6, pp. 797–807, 2012.
- [5] M. R. Stacy, M. W. Maxfield, I. M. Jaba, B. P. Jozwik, Z. W. Zhuang, B. A. Lin, C. L. Hawley, C. M. Caracciolo, P. Pal, D. Tirziu, and S. Sampath, “Multimodality imaging approach for serial assessment of regional changes in lower extremity arteriogenesis and tissue perfusion in a porcine model of peripheral arterial disease,” *Circulation: Cardiovascular Imaging*, vol. 7, no. 1, pp. 92–99, 2014.
- [6] V. E. Young, A. J. Degnan, and J. H. Gillard, “Advances in contrast media for vascular imaging of atherosclerosis,” *Imaging in Medicine*, vol. 3, no. 3, p. 353, 2011.
- [7] A. Humeau, W. Steenbergen, H. Nilsson, and T. Strömberg, “Laser Doppler perfusion monitoring and imaging: novel approaches,” *Medical & Biological Engineering & Computing*, vol. 45, no. 5, p. 421, 2007.
- [8] V. Cantisani, M. Bertolotto, H. Weskott, L. Romanini, H. Grazhdani, M. Passamonti, F. Drudi, F. Malpassini, A. Isidori, F. Meloni, F. Calliada, and F. D’Ambrosio, “Growing indications for CEUS: The kidney, testis, lymph nodes, thyroid, prostate, and small bowel,” *European Journal of Radiology*, vol. 84, no. 9, pp. 1675 – 1684, 2015.

- [9] N. Oebisu, M. Hoshi, M. Ieguchi, J. Takada, T. Iwai, M. Ohsawa, and H. Nakamura, "Contrast-enhanced color Doppler ultrasonography increases diagnostic accuracy for soft tissue tumors," *Oncol Rep*, vol. 32, no. 4, pp. 1654–1660, 2014.
- [10] E. Amarteifio, M. Krix, S. Wormsbecher, S. Demirel, S. Braun, S. Delorme, H. U. Kauczor, D. Böckler, and M. A. Weber, "Dynamic contrast-enhanced ultrasound for assessment of therapy effects on skeletal muscle microcirculation in peripheral arterial disease: pilot study," *European Journal of Radiology*, vol. 82, no. 4, pp. 640–646, 2013.
- [11] R. Kundi, S. J. Prior, O. Addison, M. Lu, A. S. Ryan, and B. K. Lal, "Contrast-enhanced ultrasound reveals exercise-induced perfusion deficits in claudicants," *Journal of Vascular and Endovascular Surgery*, vol. 2, no. 1, 2017.
- [12] A. F. Badea, A. T. Szora, S. Clichici, M. Socaciu, A. F. Tabaran, G. Baciut, C. Catoi, A. Muresan, M. Buruian, and R. Badea, "Contrast enhanced ultrasonography (CEUS) in the characterization of tumor microcirculation. validation of the procedure in the animal experimental model," *Medical Ultrasonography*, vol. 15, no. 2, p. 85, 2013.
- [13] M. Gao, J. Tang, K. Liu, M. Yang, and H. Liu, "Quantitative evaluation of vascular microcirculation using contrast-enhanced ultrasound imaging in rabbit models of choroidal melanoma," *Investigative Ophthalmology & Visual Science*, vol. 59, no. 3, pp. 1251–1262, 2018.
- [14] T. L. Szabo, *Diagnostic Ultrasound Imaging: Inside Out*. Academic Press, 2004.
- [15] J. Rubin, R. Bude, P. Carson, R. Bree, and R. Adler, "Power Doppler US: A potentially useful alternative to mean frequency-based color Doppler US," *Radiology*, vol. 190, no. 3, pp. 853–856, 1994.
- [16] T. Jansson, H. Persson, and K. Lindstrom, "Estimation of blood perfusion using ultrasound," *Proc Inst Mechan Eng, Part H: J Eng Med*, vol. 213, no. 2, pp. 91–106, 1999.
- [17] S. Bjærum, H. Torp, and K. Kristoffersen, "Clutter filters adapted to tissue motion in ultrasound color flow imaging," *IEEE Trans Ultrason Ferroelectr Freq Control*, vol. 49, no. 6, pp. 693–704, 2002.
- [18] A. Yu and L. Løvstakken, "Eigen-based clutter filter design for ultrasound color flow imaging: a review," *IEEE Trans Ultrason Ferroelectr Freq Control*, vol. 57, no. 5, pp. 1096–1111, 2010.

- [19] S. Bjærum, H. Torp, and K. Kristoffersen, “Clutter filter design for ultrasound color flow imaging,” *IEEE Trans Ultrason Ferroelectr Freq Control*, vol. 49, no. 2, pp. 204–216, 2002.
- [20] C. Gallippi and G. Trahey, “Adaptive clutter filtering via blind source separation for two-dimensional ultrasonic blood velocity measurement,” *Ultrasonic Imaging*, vol. 24, no. 4, pp. 193–214, 2002.
- [21] L. Løvstakken, S. Bjærum, K. Kristoffersen, R. Haaverstad, and H. Torp, “Real-time adaptive clutter rejection filtering in color flow imaging using power method iterations,” *IEEE Trans Ultrason Ferroelectr Freq Control*, vol. 53, no. 9, pp. 1597–1608, 2006.
- [22] I. Jolliffe, *Principal Component Analysis*. New York: Springer, 2002.
- [23] G. R. Naik, W. Wang, and eds., *Blind Source Separation: Advances in Theory, Algorithms and Applications*. Springer, 2014.
- [24] S. Zobly and Y. M. Kadah, “Clutter rejection for doppler ultrasound based on blind source separation,” *Journal of Medical Imaging and Health Informatics*, vol. 3, no. 2, pp. 187–194, 2013.
- [25] F. W. Mauldin, D. Lin, and J. A. Hossack, “The singular value filter: A general filter design strategy for PCA-based signal separation in medical ultrasound imaging,” *IEEE Transactions on Medical Imaging*, vol. 30, no. 11, pp. 1951 – 1964, 2011.
- [26] A. C. Yu, “Single-ensemble-based eigen-processing methods for color flow imaging-Part I. The Hankel-SVD filter,” *IEEE Transactions on Ultrasonics, Ferroelectrics, and Frequency Control*, 2008.
- [27] A. C. Yu and R. S. Cobbold, “Single-ensemble-based eigen-processing methods for color flow imaging-Part II. The matrix pencil estimator,” *IEEE Trans Ultrason Ferroelectr Freq Control*, vol. 55, no. 3, pp. 573–587, 2008.
- [28] C. Demené, T. Deffieux, M. Pernot, B. F. Osmanski, V. Biran, J. L. Gennisson, L.-A. Sieu, A. Bergel, S. Franqui, J. M. Correas, I. Cohen, O. Baud, and M. Tanter, “Spatiotemporal clutter filtering of ultrafast ultrasound data highly increases Doppler and fUltrasound sensitivity,” *IEEE Trans Med Imag*, vol. 34, no. 11, pp. 2271–2285, 2015.
- [29] S. V. Vaseghi, *Advanced Digital Signal Processing and Noise Reduction*. John Wiley & Sons, 2008.
- [30] J. Hanley and B. McNeil, “The meaning and use of the area under the receiver operating characteristic (ROC) curve,” *Radiology*, vol. 143, no. 1, pp. 29–36, 1982.

- [31] R. Zemp, C. Abbey, and M. Insana, "Ideal observer model for detection of blood perfusion and flow using ultrasound," *Inf Process Med Imaging*, vol. 18, pp. 318–329, 2003.
- [32] H. Barrett and K. Myers, *Foundations of Image Science*. Hoboken NJ: Wiley-Interscience, 2004.
- [33] C. Abbey, R. Zemp, J. Liu, K. Lindfors, and M. Insana, "Observer efficiency in discrimination tasks simulating malignant and benign breast lesions imaged with ultrasound," *IEEE Trans Med Imag*, vol. 25, no. 2, pp. 198–209, 2006.
- [34] A. Heimdal and H. Torp, "Detecting small blood vessels in color flow imaging: a statistical approach," *IEEE Proc Ultrason Symp*, pp. 1219 – 1222, 1997.
- [35] S. Hovda, H. Rue, and B. Olstad, "New Doppler-based imaging method in echocardiography with applications in blood/tissue segmentation," *Med Imag Informatics*, vol. LNCS-4987, pp. 207–215, 2008.
- [36] S. Cherry, P. Carnochan, J. Babich, F. Serafini, N. Rowell, and I. Watson, "Quantitative in vivo measurements of tumor perfusion using rubidium-81 and positron emission tomography," *J Nucl Med*, vol. 31, no. 8, pp. 1307–1315, 1990.
- [37] R. Jain and K. Ward-Hartley, "Tumor blood flow characterization, modifications, and role in hyperthermia," *IEEE Trans Son Ultrason*, vol. 31, no. 5, pp. 504–529, 1984.
- [38] H. van Trees, *Detection, Estimation, and Modulation Theory, Part I*. John Wiley and Sons, NY, 1968.
- [39] N. Nguyen, C. Abbey, and M. Insana, "Objective assessment of sonographic quality I: Task information," *IEEE Trans Med Imag*, vol. 32, no. 4, pp. 683–690, 2103.
- [40] L. A. F. Ledoux, P. J. Brands, and A. P. G. Hoeks, "Reduction of the clutter component in Doppler ultrasound signals based on singular value decomposition: A simulation study," *Ultrasonic Imaging*, vol. 19, no. 1, pp. 1 – 18, 1997.
- [41] W. Yang and P. Dempsey, "Diagnostic breast ultrasound: Current status and future directions," *Radiol Clin North Am*, vol. 45, no. 5, pp. 845–861, 2007.
- [42] L. D. Lathauwer, B. D. Moor, and J. Vandewalle, "A multilinear singular value decomposition," *SIAM Journal on Matrix Analysis and Applications*, vol. 21, no. 4, pp. 1253 – 1278, 2000.

- [43] G. Bergqvist and E. Larsson, “The higher-order singular value decomposition: Theory and an application [lecture notes],” *IEEE Signal Processing Magazine*, vol. 27, no. 3, pp. 151 – 154, 2010.
- [44] H. Niiyama, N. Huang, M. Rollins, and J. Cooke, “Murine model of hindlimb ischemia,” *Journal of Visualized Experiments*, vol. 23, no. e1035, 2009.
- [45] R. McDonough and A. Whalen, *Detection of Signals in Noise, 2nd Edition*. Academic Press, San Diego, 1995.
- [46] Z.-P. Liang, “Spatiotemporal imaging with partially separable functions,” in *Proc. IEEE Int Symp Biomed Imaging*. IEEE, 2007, pp. 988–991.
- [47] D. Muti and S. Bourennane, “Multidimensional filtering based on a tensor approach,” *Signal Processing*, vol. 85, no. 12, pp. 2238 – 2353, 2005.
- [48] L. D. Lathauwer, B. D. Moor, and J. Vandewalle, “On the best rank-1 and rank- $(r_1, r_2, \dots, r_n)$  approximation of higher-order tensors,” *SIAM Journal on Matrix Analysis and Applications*, vol. 21, no. 4, pp. 1324 – 1342, 2000.
- [49] N. Vannieuwenhoven, R. Vandebril, and K. Meerbergen, “A new truncation strategy for the higher-order singular value decomposition,” *SIAM Journal on Scientific Computing*, vol. 34, no. 2, pp. A1027 – A1052, 2012.
- [50] J. Hua, L. Dobrucki, M. Sadeghi, J. Zhang, B. Bourke, P. Cavaliere, and J. Song, et al., “Noninvasive imaging of angiogenesis with a  $^{99m}\text{Tc}$ -labeled peptide targeted at  $\alpha_v\beta_3$  integrin after murine hindlimb ischemia,” *Circulation*, vol. 111, no. 6, pp. 3255 – 3260, 2005.
- [51] D. Bertoldi, P. L. de Sousa, Y. Fromes, C. Wary, and P. Carlier, “Quantitative, dynamic and noninvasive determination of skeletal muscle perfusion in mouse leg by NMR arterial spin-labeled imaging,” *Magn Reson Imaging*, vol. 26, no. 9, pp. 1259 – 1265, 2008.
- [52] J. Baranger, B. Arnal, F. Perren, O. Baud, M. Tanter, and C. Demené, “Adaptive spatiotemporal SVD clutter filtering for ultrafast Doppler imaging using similarity of spatial singular vectors,” *IEEE Transactions on Medical Imaging*, 2018.
- [53] M. A. Lediju, M. J. Pihl, J. J. Dahl, and G. E. Trahey, “Quantitative assessment of the magnitude, impact and spatial extent of ultrasonic clutter,” *Ultrasonic Imaging*, vol. 30, no. 3, pp. 151–168, 2008.

- [54] W. Pereira and C. Maciel, “Performance of ultrasound echo decomposition using singular spectrum analysis,” *Ultrasound in Medicine and Biology*, vol. 27, no. 9, pp. 1231–1238, 2001.
- [55] T. G. Kolda and B. Bader, “Tensor decompositions and applications,” *SIAM Review*, vol. 51, no. 3, pp. 455–500, 2009.
- [56] M. Wax and T. Kailath, “Detection of signals by information theoretic criteria,” *IEEE Transactions on Acoustics, Speech, and Signal Processing*, vol. 33, no. 2, pp. 387–392, 1985.
- [57] Q. Wu and D. R. Fuhrmann, “A parametric method for determining the number of signals in narrow-band direction finding,” *IEEE Transactions on Signal Processing*, vol. 39, no. 8, pp. 1848–1857, 1991.
- [58] T. Yokota, N. Lee, and A. Cichocki, “Robust multilinear tensor rank estimation using higher order singular value decomposition and information criteria,” *IEEE Transactions on Signal Processing*, vol. 65, no. 5, pp. 1196–1206, 2017.
- [59] E. J. Benjamin, M. J. Blaha, S. E. Chiuve, M. Cushman, S. R. Das, R. Deo, J. Floyd, M. Fornage, C. Gillespie, and C. R. Isasi, et al., “Heart disease and stroke statistics-2017 update: A report from the American Heart Association,” *Circulation*, vol. 135, no. 10, pp. e146–e603, 2017.
- [60] M. Heil, I. Eitenmüller, T. Schmitz-Rixen, and W. Schaper, “Arteriogenesis versus angiogenesis: similarities and differences,” *Journal of Cellular and Molecular Medicine*, vol. 10, no. 1, pp. 45–55, 2006.
- [61] S. Prahl, “Tabulated molar extinction coefficient for hemoglobin in water,” [http://omlc.org/spectra/hemoglobin/summary, html](http://omlc.org/spectra/hemoglobin/summary.html), 1999.
- [62] Y. Yang, G. Tang, J. Yan, B. Park, A. Hoffman, G. Tie, R. Wang, and L. M. Messina, “Cellular and molecular mechanism regulating blood flow recovery in acute versus gradual femoral artery occlusion are distinct in the mouse,” *Journal of Vascular Surgery*, vol. 48, no. 6, pp. 1546–1558, 2008.
- [63] M. W. J. Cleeter, J. M. Cooper, V. M. Darley-Usmar, S. Moncada, and A. H. V. Schapira, “Reversible inhibition of cytochrome c oxidase, the terminal enzyme of the mitochondrial respiratory chain, by nitric oxide: Implications for neurodegenerative diseases,” *FEBS Letters*, vol. 345, no. 1, pp. 50–54, 1994.
- [64] M. Heil and W. Schaper, “Insights into pathways of arteriogenesis,” *Current Pharmaceutical Biotechnology*, vol. 8, no. 1, pp. 35–42, 2007.

- [65] N. V. Royen, J. J. Piek, I. Buschmann, I. Hofer, M. Voskuil, and W. Schaper, “Stimulation of arteriogenesis; a new concept for the treatment of arterial occlusive disease,” *Cardiovascular Research*, vol. 49, no. 3, pp. 543–553, 2001.
- [66] P. Abdulhannan, D. A. Russell, and S. Homer-Vanniasinkam, “Peripheral arterial disease: A literature review,” *British Medical Bulletin*, vol. 104, no. 1.
- [67] A. K. Jayanthi, N. Sujatha, M. R. Reddy, and V. B. Narayanamoorthy, “Non invasive blood flow assessment in diabetic foot ulcer using laser speckle contrast imaging technique,” in *Biomedical Applications of Light Scattering VIII*, vol. 8952, 2014, p. 89521D.
- [68] K. Maslov, H. F. Zhang, S. Hu, and L. V. Wang, “Optical-resolution photoacoustic microscopy for in vivo imaging of single capillaries,” *Optics Letters*, vol. 33, no. 9, pp. 929–931, 2008.
- [69] J. R. Wilson, D. M. Mancini, K. McCully, N. Ferraro, V. Lanoce, and B. Chance, “Noninvasive detection of skeletal muscle underperfusion with near-infrared spectroscopy in patients with heart failure,” *Circulation*, vol. 80, no. 6, pp. 1668–1674, 1989.